Charles University Prague

Faculty of Mathematics and Physics

Pressure effects on the magnetocaloric $R_5(Si_xGe_{1-x})_4$ compounds

Yuriy Skorokhod

Doctoral Thesis

Institute of Physics,

Academy of Sciences of the Czech Republic

Prague, 2008

Contents:

1 Introduction

Synthesis and structural characterization of the first R_5T_4 compounds (R-rare earth, T – Si,Ge) was performed in 1966. These compounds present very complex layered structures. Most of them crystallize in the orthorhombic structure (*Pnma* space group) but some of them presented monoclinic or orthorhombic distortions. Silicides were mostly ferromagnets and germanides ordered antiferromagnetically, but presenting large positive paramagnetic Curie temperature which pointed to the existence of complex magnetic interactions. Also surprising was the fact that Gd_5Si_4 ordered ferromagnetically at 336 K, more than 40 K higher than undiluted metallic Gd. Unfortunately sparse research work, mainly on crystal and structure determination was devoted to this system in the forthcoming 30 years.

In the late nineties V.K.Pecharsky and K.A.Gschneider were involved in the research of new rare earth intermetallic materials for application in room-temperature magnetic refrigeration systems. This promising technology is based on magnetocaloric effect as a cooling mechanism and is characterized by being environmental-friendly and energetically efficient, due to the absence of ozone depletion and greenhouse chemicals, and by a higher performance that the conventional vapor-compression refrigeration techniques.

The best candidate for room temperature magnetic refrigerant was metallic Gd which presented the record values of magnetocaloric effect around T_C = 291 K. In a study of Gd-based materials with long range magnetic order near room temperature they determined the magnetocaloric effect in $Gd_5(Si_{0.5}Ge_{0.5})_4$ and its maximum value at T_C = 276 K was found double the best known value in this range of temperature for a reversible process. This was labeled as “giant” magnetocaloric effect (GMCE). Further studies reveled that this novel property could be tuned from ~ 40 K to room temperature only by modifying the Si/Ge ration of the $Gd_5(Si_xGe_{1-x})_4$ where $0 \leq x \leq 0.5$. It opens a wide range of applications for these compounds.

An intrinsically layered crystallographic structure of $R_5(Si_xGe_{1-x})_4$ compounds is built by stacking two-dimensional sub-nanometric-thick layers (slabs) interconnected via partially covalent inter-slab (Si,Ge)–(Si,Ge) bonds. Three different crystallographic structures depend on the Si/Ge ratio, which are intimately related to the number of formed interslab covalent-like bonds: the *O*(I) orthorhombic (*Pnma*) structure where all

bonds are formed; the *O*(II) orthorhombic structure (*Pnma*) with no interslab bonds; and the monoclinic (*M*) $P112_1/a$ structure where one every other bond is broken. The formation or cleavage of these bonds by changing external parameters such as temperature, magnetic field, or hydrostatic pressure results in dramatic crystallographic, electronic, and magnetic changes.

The aim of these Theses was to perform a deep insight into evolution and stability of the crystal structures and magnetic behavior and their correlation to changes of magnetocaloric properties of R_5T_4 compounds (R-rare earth, T – Si,Ge). High hydrostatic pressure enables to change the volume without remarkable changes of electronic structure contrary to the case of substitution. As a consequence of the decrease of interatomic distances we may expect an enhancement of the interlayer interactions, favoring the ferromagnetic *O*(I) state, in a fashion similar to Si doping that leads to reducing of volume and consequent increasing of T_C in agreement with localized nature of magnetism. The aim was also to study the possibility to induce three-dimensional ferromagnetic correlations in Gd_5Ge_4 that is on the edge of stability of antiferromagnetic order. As the effect of chemical pressure may be quite different to that of a pure cell contraction caused by the applied hydrostatic pressure, the aim was to distinguish the pure volume effect and the role of Si – Ge substitution by the studies of the volume evolution of the several layered crystallographic structures with different magnetic structures. Moreover ambient pressure studies of magnetocaloric effects on different compounds of this series showed remarkable different results on compounds that have coupled and decoupled structural and magnetic phase transitions. Our aim is to utilize the different volume dependencies of structural and magnetic transitions to study also the role of coupling and/or decoupling of these two types of transitions on magnetic, elastic and magnetocaloric properties of properly chosen compounds and to contribute to determination of the detailed phase diagrams.

Outline

A complex study of the magnetic and magnetocaloric properties of $R_5(Si_xGe_{1-x})_4$ compounds with and special emphasis on the volume stability of both the crystal and magnetic structures is the main subject of this thesis.

Basic theoretical concepts and relations concerned magnetic properties, phase transitions and heat capacity are summarized in **Chapter 2**. The first part reveals model of localized magnetism of rare-earth elements. The next parts are related to the description of first and second order phase transitions, heat capacity, magnetocaloric effect, direct and indirect measurements of magnetocaloric effect and finally by the general trends of the pressure effect on magnetic systems.

Sample preparation and characterization together with the experimental techniques used to examine the magnetic properties of the studied systems are described in **Chapter 3.** The high pressure technique used for both the magnetic measurements and thermal expansion under pressure is described in detail.

In **Chapter 4** the magnetic properties of $R_5(Si_xGe_{1-x})_4$ compounds are reviewed. The main attention is devoted to the peculiarities of crystal structures and their correlations to magnetic properties such as magnetic structures and ordering temperatures.

Chapter 5 deals with the experimental results obtained on the studied compounds. Selected compounds of the $Gd_5(Si_xGe_{1-x})_4$ series (x=0, 0.1) were studied under hydrostatic pressure up to 9 kbar by means of ac magnetic susceptibility, compressibility, and linear thermal expansion measurements. In summary, we have found a positive increase of all transition temperatures in all studied $Gd_5(Si_xGe_{1-x})_4$. The calculated values of $d\ln T_C/d\ln V$ are significantly lower than those estimated from the concentration dependence of the lattice cell volume, demonstrating that the dependence of the transition temperatures upon changing the Si/Ge ratio along the series cannot be explained by a pure volume effect.

Gd_5Ge_4 is the only member of the $Gd_5(Si_xGe_{1-x})_4$ family where three-dimensional exchange interactions between two-dimensional correlated layers of the crystallographic structure are so weak that spontaneous ferromagnetism does not set in at any temperature. Gd_5Ge_4 orders antiferromagnetically at ~ 130 K, this system presenting a very complex magnetic field-temperature (H–T) phase diagram. Linear thermal expansion and magnetic measurements under pressure revealed that the reduction of the unit cell volume induces a spatially phase-segregated ground state below 10 kbar. We proved the possibility to induce three-dimensional ferromagnetic correlations in Gd_5Ge_4 upon application of an external hydrostatic pressure.

$Tb_5(Si_xGe_{1-x})_4$ alloys with intermediate compositions $0.4 \le x \le 0.6$ present a paramagnetic monoclinic structure at room temperature, the low-temperature ground state being ferromagnetic and *O*(I) structure. The structural and magnetic transitions are not fully coupled in this system. The study of the temperature-pressure (T–P) phase

diagram of $Tb_5Si_2Ge_2$ by means of thermal expansion, magnetization, and neutron powder diffraction experiments under hydrostatic pressure showed a coupling of the ferromagnetic transition with the structural change at a tricritical point in the vicinity of 8.6 kbar. Associated pressure induced changes of magnetocaloric effect were observed.

The studies of magnetic, magnetoelastic and magnetocaloric properties of $Nd_5Si_{1.45}Ge_{2.55}$ and $Pr_5Si_{1.5}Ge_{2.5}$ compounds show the qualitatively similar behavior of properties of these two compounds with monoclinic crystallographic structure. Application of high hydrostatic pressure leads to moderate increase of both the T_C and magnetocaloric effect that are consequence of second-order magnetic phase transition with no changes of crystal structure. Values of dT_C/dV and $d\left|-\Delta S_M\right|/dV$ obtained from experiments under high hydrostatic pressure are sufficiently lower than those estimated from the concentration dependence of the lattice cell volume, thus, similarly as in the case of $Gd_5(Si_xGe_{1-x})_4$ series changes of physical properties of the Nd and Pr compounds can not be explained only by pure volume effects.

The summary of main results and final conclusions are given in **Chapter 6**.

2 Theoretical aspects

2.1 Localized magnetism of the rare earth elements

Magnetic moment of the rare earth series originates in the *4f* electron shell. *4f* wave functions have negligible overlap due to shielding by eight $5s^2$-$5p^6$ electrons and by three 5d-6s valence electrons. This implies that the magnetism of the rare earth elements has strongly localized nature and can be successfully described by the atomic model. Unfilled electron shells create a non-zero spin $\boldsymbol{S}$ and orbital $\boldsymbol{L}$ angular momentum of the atom.

Values of $\boldsymbol{L}$, $\boldsymbol{S}$, and total angular momentum $\boldsymbol{J}$ can be predicted using the empirical Hund's rules from the number of electrons in incomplete electron shells:

- Quantum states are filled in order to maximize $S = \sum m_s$ ($m_s = \pm 1/2$) as far as allowed by the Pauli principle.
- The value of $L=\sum m_l$ ($m_l = -l, (-l + 1), ..., 0, ..., (l-1), l$) is also maximized accordingly to the Pauli principle and to the rule 1.
- The absolute value of the $\boldsymbol{J}$ is a result of subtraction $J=L-S$, when the electron shell is less than half filled. Otherwise, it is the result of addition $J=L+S$.

The rules describe the tendency of a system to minimize the Coulomb repulsion (of order 1 eV per atom) and spin-orbit interaction energy, $E_{SO} = \xi \boldsymbol{L}\cdot\boldsymbol{S}$, ($\sim 10^{-4}$ eV/atom) (O'Handley 2000):

The total magnetic moment, connected with J is given by

$$\mu_J = gJ\mu_B \tag{2.1}$$

where μ_B is the Bohr magneton

$$\mu_B = \frac{e\hbar}{m} \tag{2.2}$$

and g is the Landé factor determined by:

$$g = 1 + \frac{J(J+1) + S(S+1) - L(L+1)}{2J(J+1)} \tag{2.3}$$

Some atomic and related magnetic characteristics of the rare earth ions are presented in the Table 2.1

Table 2.1 Atomic characteristics of the rare earth R^{3+} ions.

Rare Earths	Z	Electronic State ($^{+}3$ Ion)						Magnetic Moment, μ_B	
		n_{4f}	S	L	J	$^{2S+1}L_J$	g	gJ	$g[J(J+1)]^{1/2}$
La	57	0	0	0	0	$^1S_0$	-	0	0
Ce	58	1	1/2	3	5/2	$^2F_{5/2}$	6/7	2.14	2.54
Pr	59	2	1	5	4	$^3H_4$	4/5	3.20	3.58
Nd	60	3	3/2	6	9/2	$^4I_{9/2}$	8/11	3.27	3.62
Pm	61	4	2	6	4	$^5I_4$	3/5	2.40	3.68
Sm	62	5	5/2	5	5/2	$^6H_{5/2}$	2/7	0.72	0.85
Eu	63	6	3	3	0	$^7F_0$	-	0	0
Gd	64	7	7/2	0	7/2	$^8S_{7/2}$	2	7.0	7.94
Tb	65	8	3	3	6	$^7F_6$	3/2	9.0	9.72
Dy	66	9	5/2	5	15/2	$^6H_{15/2}$	4/3	10.0	10.64
Ho	67	10	2	6	8	$^5I_8$	5/4	10.0	10.60
Er	68	11	3/2	6	15/2	$^4I_{15/2}$	6/5	9.0	9.58
Tm	69	12	1	5	6	$^3H_6$	7/6	7.0	7.56
Yb	70	13	1/2	3	7/2	$^2F_{7/2}$	8/7	4.0	4.53
Lu	71	14	0	0	0	$^1S_0$	-	0	0

2.1.1 Exchange interactions

The Hund's rules determine the magnitude of the magnetic moment for a lone atom. When atoms having the magnetic moment, form a solid, spontaneous magnetic ordering arises owing to exchange interaction between separate atoms. Magnitude of the interatomic exchange describes how strongly the atomic moments are coupled parallel or antiparallel. Thus, the measure of exchange interaction is the temperature of transition to magnetically ordered state. One can consider three types of the exchange interaction on the interatomic level – direct, indirect and superexchange. The superexchange occurs mostly in the insulating compounds in which two electrons from

a double negative ion (such as oxygen) in a solid go to different positive ions and couple with their spins, giving rise to a strong antiferromagnetic coupling between the positive ions, which are too far apart to have a direct exchange interaction.

Direct exchange is characterized by direct overlapping of electronic shells of the neighboring atoms. The second type is realized when the interaction can be mediated by various mechanisms, producing long range effects.

When spin magnetic moments of adjacent atoms *i* and *j* make an angle $\varphi_{i,j}$, the direct-exchange energy, ω_{EXij}, between two moments can be expressed as

$$\omega_{EXij} = -2J_{ij}S_iS_j\cos\varphi_{ij} \qquad (2.4)$$

where J_{ij} is the exchange integral between atoms numbered *i* and *j* and S_i S_j are their total spin quantum number. For positive values of *J* this gives a minimum when $\phi_{ij} = 0$ i.e. the spins are aligned parallel to each other. The negative *J* corresponds to antiparallel spin orientation. As the direct-exchange energy for neighboring atoms is dependent only on the angle between them it does not give rise to anisotropy.

Introduced by Heisenberg in 1928, the exchange Hamiltonian for solids is written as

$$H_{ex} = -2\sum J_{ij}\,\boldsymbol{S}_i\,\boldsymbol{S}_j \qquad (2.5)$$

The energy of direct exchange is typically of the order of 100 – 1000 K which implies quite high ordering temperatures of the compounds and occurs mainly for metals with partially filled 3d shell (for example Mn, Fe, Co, Ni). The Bethe-Slater curve represents the magnitude of direct exchange as a function of interatomic distance. Cobalt is situated near the peak of this curve, while chromium and manganese are on the side of negative exchange. Iron, with its sign depending on the crystal structures probably around the zero-crossing point of the curve,

2.1.2 Indirect exchange by polarization of the conduction electrons

Small overlap of the 4*f* shells makes direct exchange impossible. In this case interaction between separate magnetic moments becomes possible via polarization of conducting electrons propagating between localized magnetic moments. Such a mechanism was explained independently by Ruderman and Kittel (Ruderman and Kittel 1954) and Kasuya and Yosida (Kasuya 1956, Yosida 1957) and now it is known as RKKY interaction. The RKKY model was introduced for charge density perturbation

caused by impurity atom. According to Kittel, the spin density about an impurity (localized moment S_i) in a metal can be expressed as

$$\rho\uparrow\downarrow(x) = n\uparrow\downarrow [1 \pm 9n\uparrow\downarrow\pi JS^{\varepsilon}F(2k_F{}^{\uparrow\downarrow}r)/E_F] \quad (2.6)$$

where

$$F(x) = x^{-4}(\sin x - x \cos x) \quad (2.7)$$

i.e. the spin polarization is described by damped periodical function of distance from the charge. In that way, the spin information from the localized magnetic moment reaches another one. When a remote atom bearing a local magnetic moment is situated at an arbitrary distance from the first one, it interacts ferro- or antiferromagnetically depending on the part (positive or negative) of the polarization wave in a point where the atom is. The exchange Hamiltonian for coupling of mentioned spins is

$$H_{RKKY}(x) = S_i S_j (2\pi)^{-3} 4J^2 m^* k_F{}^r F(2k_F r) \quad (2.8)$$

that is shown in Fig. 2.1. The RKKY interaction is very well suited for describing of the magnetic properties of rare-earth metals and alloys, multilayered structures, diluted alloys and any other magnetic systems in which the direct exchange is impossible or extremely embarrassed.

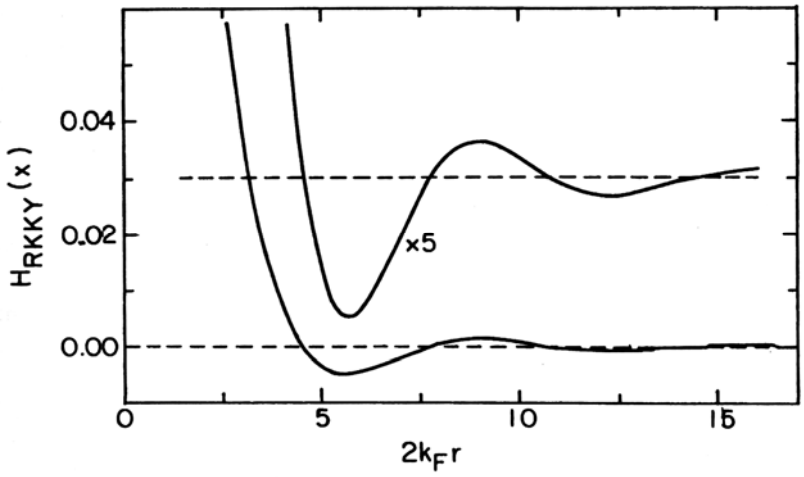

Figure 2.1. Variation of the RKKY oscillatory function F(x) showing how the sign of the indirect exchange interaction can change for atoms at different distances from a given site in a material.

It is clear, that the magnetic interaction in RKKY systems is strongly dependent on interatomic distances. So any changes of volume and symmetry can lead to significant changes of strength of the magnetic interaction and even to changes of sign of the exchange integral.

2.2 First-order and second-order phase transitions

The ideal second-order phase transition are the continuous phase transitions where one phase phase transforms itself into the second phase in a continuous manner so two phases never coexist. These transitions have no associated latent heat. Following Landau, the free energy can be expanded in series of even powers of the ordering parameter in vicinity of the critical point. For ferromagnetic phase transitions, the spontaneous magnetization can be chosen as an appropriate ordering parameter and the free energy can be expressed as:

$$F(M,T) = F_0 + \frac{1}{2}a_1(T,H,P)M^2 + \frac{1}{4}a_3(T,H,P)M^4 + ... - MH \tag{2.9}$$

where coefficients a_1, a_2 are assumed to be functions of temperature, magnetic field and pressure and M is spontaneous magnetization at temperature T normalized to its value at $T=0$ K. The Landau sufficient condition for a second-order transition is associated to the minimum of free energy: the system must be stable. In this case the fourth-order coefficient a_3 in (2.9) must be positive and the third-order one does not appear. In the case that a_3 becomes negative, there are two minima of $F=f(M)$ and a first-order transition occurs.

The main difference of the first-order transition from the second-order one is that the first-order phase transitions involve a latent heat. As the energy cannot be instantaneously transferred between the system and its environment, first-order transitions are associated with the coexistence of two phases (mixed-phase regimes) in vicinity of critical point. In this case the theoretical description of behavior of mixed-phase systems that exist during the phase transition becomes complicated.

On the basis of the Landau-Devonshire theory (Devonshire 1949, 1951, 1954), which is the improved Landau theory for first-order phase transitions, the free energy of the system can be written as:

$$F(M,T,H) = F_0(T) + \alpha(T - T_0)M^2 - \beta M^4 + \gamma M^6 - \delta MH \tag{2.10}$$

where M is the magnetization, $\alpha, \beta, \gamma, \delta, T_0$ - are the parameters for the particular material. Introducing the dimensionless quantities:

$$f = \frac{\gamma^2}{\beta^3}F, \quad t = \frac{\alpha\gamma}{\beta^2}(T - T_0), \quad \eta = \sqrt{\frac{\gamma}{\beta}}M, \quad h = \frac{\delta}{\beta}\left(\frac{\gamma}{\beta}\right)^{3/2}H, \tag{2.11}$$

the free energy can be rewritten:

$$f(\eta,h,t) = f_0 + t\eta^2 - \eta^4 + \eta^6 - h\eta. \tag{2.12}$$

From the equilibrium condition

$$\left(\frac{\partial f(\eta,h,t)}{\partial \eta}\right)_{h,t} = 0 \tag{2.13}$$

the ordering parameter η can be expressed as a function of h and t:

$$h = 2t\eta - 4\eta^3 + 6\eta^5 \tag{2.14}$$

Then, the $h-t$ magnetic phase diagram can be obtained from (2.14)

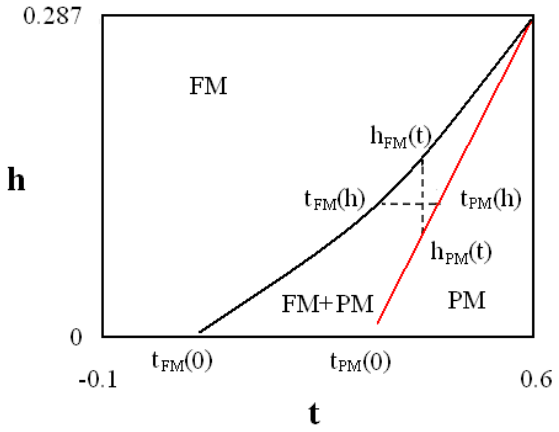

Figure 2.2 The magnetic phase diagram, based on Landau-Devonshire theory for the first-order phase transition. "FM+PM" mark a region where two FM and PM phases coexist.

In Fig. 2.2, the h_{PM}(t) and h_{FM}(t) show the critical field limit at temperature t for two phases coexistence. Similarly, the upper and lower critical temperature at magnetic field h is marked as h_{PM}(h) and h_{FM}(h), respectively. The field dependence of the order parameter at a certain temperature and the temperature dependences in a certain magnetic field on the base of the magnetic phase diagram are depicted in Fig. 2.3a,b.

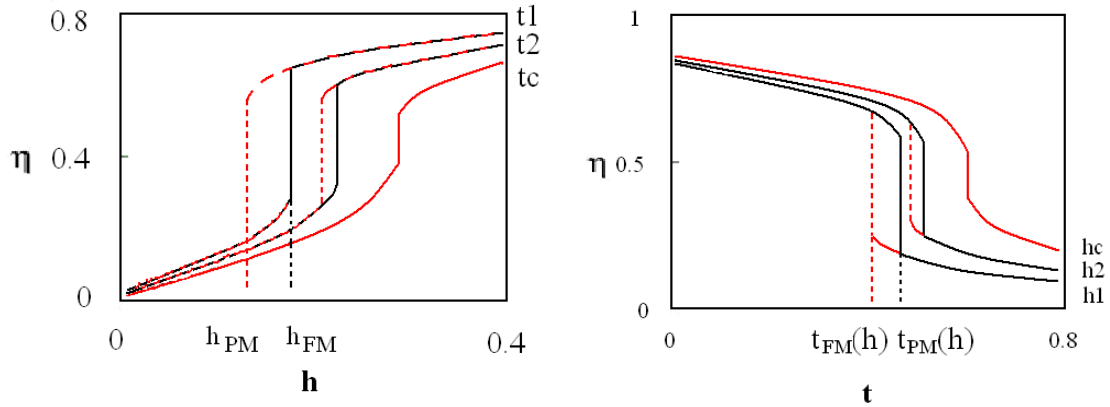

Figure 2.3 Behavior of the order parameter, according to the Landau-Devonshire theory: a) field dependence at t1=0.45 and t2=0.52; b) temperature dependence in field h1=0.15 and h2=0.2. Here dashed lines mark cooling (field decrease) and solid lines mark heating (field increase).

When the temperature is lower than $t_{FM}(0)$, the material in zero field has orthorhombic ferromagnetic structure and its magnetic behavior in increasing field is usual for a soft-magnetic material and a hysteresis is not present. When the temperature is above $t_{PM}(0)$, the alloy in zero field lies in a monoclinic PM state. When the temperature is higher than $t_{PM}(0)$ and magnetic field is lower than h_{PM}, the material has monoclinic paramagnetic state. With field increasing to h_{PM}, the field-induced first-order magnetostructural transition begins and the material enters the FM+PM phase state (Fig. 2.2). With further field increasing, the FM part in the intermediate state growth, and after the value h_{FM} has been reached, the material is fully transformed to the FM orthorhombic state. For the field decreasing, the situation is inverse and the magnetic hysteresis is present.

The calculated temperature dependence of the order parameter is depicted in Fig. 2.3, *b*. When the temperature is below t_{FM}, the material is in a ferromagnetic state with orthorhombic structure. When the temperature reaches $t_{FM,}$ the material begins to undergo the first-order transition from the orthorhombic ferromagnetic to the monoclinic paramagnetic phase (intermediate FM+PM state). With temperature increasing to t_{PM}, the material has become transformed totally to a paramagnetic monoclinic state. For cooling, the situation can be described similarly but the thermal hysteresis is present. Usually, the temperature and field hysteresis are determined by the differences t_{PM}- t_{FM} and h_{FM}-h_{PM}, respectively.

A phenomenological description of the first-order transition in $Gd_5(Si_xGe_{1-x})_4$ in composition range $0.24<x<0.5$ was performed by B.Teng *et al.* (Teng 2002). These materials undergo a first-order magnetostructural transition from ferromagnetic orthorhombic to paramagnetic monoclinic phase in temperature range from 130K for x=0.24 to 276K for x=0.5. The transition, accompanied with the GMCE, behaves on the one hand as field induced PM-FM transition with a magnetic field hysteresis and on the other hand as a temperature induced FM-PM transition with temperature hysteresis and field-driven T_C.

2.3 Heat Capacity and Magnetocaloric effect

2.3.1 Heat Capacity

The heat capacity C_x at a constant parameter x is defined as

$$C_x = \left(\frac{dQ}{dT}\right)_x \tag{2.15}$$

where dQ is the heat amount which changes the system temperature on dT. For nonmagnetic substance only two definitions of the C are practically interesting: at constant volume C_V and at constant pressure C_P. The first definition is more fundamental than C_P because C_V can be obtained directly from the energy of the system:

$$C_V = \frac{dU}{dT} \tag{2.16}$$

but C_P is easier to be measured experimentally. The difference between C_V and C_P is:

$$C_P - C_V = \frac{\alpha_T^2 TV}{k_T} \tag{2.17}$$

where α_T is the volume thermal expansion coefficient and k_T is the isothermal compressibility of the substance. At low temperatures the difference is negligible for solids and reaches about 5% at room temperature. But at higher temperatures it must be taken into account.

In nonmagnetic solids, there are two contributions into the heat capacity. First one is connected with electron gas and defined as

$$C_{el} = \frac{2}{3}\pi^2 k_B^2 V_m N(\varepsilon_F) = \gamma T \tag{2.18}$$

where $N(\varepsilon_F)$ is the density of electronic states at the Fermi level and V_m is the molar volume. Plotting the low-temperature specific heat data in the form C_V / T vs. T^2, the γ coefficient can be obtained as a crossing point of the plot with the C_V / T axis.

The second contribution to the specific heat C_{ph} corresponds to the phonon excitations in the crystal lattice. At the lowest temperatures, it conforms the T^3-dependence and saturates to the value $C_{ph} = 3N_{f.u.}R$ for molar heat capacity at the highest temperatures (here, $N_{f.u.}$ is number of atoms per formula unit, $R = N_A k_B$ =8.314 is the gas constant) which is the Dulong-Petit law.

First, the C_{ph} temperature dependence in a wide temperature range was described by Einstein. The lattice vibrations were supposed as a combination of N oscillators with identical resonant frequency. Einstein's expression for the molar specific heat is:

$$C_{phE} = R\sum_{i=1}^{N_E} x_{Ei}^2 \frac{\exp(x_{Ei})}{[\exp(x_{Ei})-1]^2} \tag{2.19}$$

where N_E is number of optical branches in the phonon spectra ($N_E = 3N_{f.u.}$).

Later, Debye proposed the model which describes the phonon part as contribution of harmonic oscillators with different frequencies ω_D. Debye's formula for the C_{ph} is:

$$C_{phD} = 9Nk_B\left(\frac{T}{\theta_D}\right)^3 \int_0^{x_D} \frac{x^4 \exp(x)}{[\exp(x)-1]^2} dx \tag{2.20}$$

where $x_D = \frac{\theta_D}{T}$ and $\theta_D = \frac{\hbar\omega_D}{k_B}$ is Debye characteristic temperature of saturation of the oscillating modes (at which the maximum possible frequency is presented in the phonon spectra).

For the best C_{ph} approximation, C.Martin (C.Martin 1991) combined both models taking into account small but not negligible deviation from harmonicity. The resulting phonon specific heat can be written as:

$$C_{ph} = R\left(\sum_{i=1}^{3N_{f.u.}-3} \frac{1}{1-\alpha_{Ei}T} \frac{x_{Ei}^2 \exp(x_{Ei})}{[\exp(x_{Ei})-1]^2} + \frac{9}{1-\alpha_D T}\left(\frac{1}{x_D}\right)^3 \int_0^{x_D} \frac{x^4 \exp(x)}{[\exp(x)-1]^2} dx\right) \tag{2.21}$$

where α_D and α_{Ei} are the anharmonic correction coefficients. Here, the Debye integral

$$I_D = \int_0^{x_D} \frac{x^4 \exp(x)}{[\exp(x)-1]^2} dx$$

for x_D>0.5 (temperature range $T<2\theta_D$) can be substituted with satisfactory accuracy by modified Gaussian:

$$I_D \approx 25.88 - 26.31\exp(-0.0249x_D^{2.224}) \tag{2.22}$$

for the simplification of the calculations (Svoboda 2001).

In magnetic materials the additional contribution to the specific heat is present. The ideal magnetic order can exist only in absence of thermal fluctuations. At a finite temperature magnetic moments move aside from their initial directions, that leads to excitation of spin waves. For ferri- and ferromagnets at low temperatures, the specific heat related to the spin waves can be expressed as:

$$C_M = c_l N k_B \left(\frac{k_B T}{2 I_{ex} S} \right)^{3/2} \tag{2.23}$$

where c_l is the constant defined by a crystal structure type, N is the number of magnetic atoms, I_{ex} is the exchange integral and S is the spin of the magnetic atom. In the case of antiferromagnetic ordering, the power index is 3 (Kittel 1986, Gopal 1966). Above T_C, C_M drops to zero value. However, experimentally observed C_M values were much higher then it was predicted theoretically.

2.3.2 Magnetocaloric Effect

Some magnetic materials heat up when they are placed in a magnetic field and cool down when removed. This effect was discovered by E.Warburg in 1881 in pure iron (Warburg 1881) and is known as the Magnetocaloric effect (MCE). The strength of the effect has been around 0.5 to 2 K per 10 kOe change in magnetic field. The larger MCE was observed in gadolinium and reached 3 to 4 K per 10 kOe.

Physical origin of the MCE is the transference of entropy between a system of magnetic moments and a crystal lattice, which was independently explained by Debye (Debye 1926) and Giauque (Giauque 1927). The value of the entropy of a ferromagnet (FM) depends on both field H and temperature T. Total entropy can be considered as sum of the magnetic, lattice and electron entropies:

$$S_{total}(H,T) = S_M(H,T) + S_{lat}(H,T) + S_{el}(H,T) \quad (2.24)$$

Fig. 2.4 shows a diagram of the entropy of a FM near T_C as a function of T. The total entropy is displayed for an applied external field H_1 and for zero field H_0. The magnetic part of the entropy is also shown for each H_1 and H_0.

Two processes are shown in the diagram in order to understand the thermodynamics of the MCE:

1. Magnetic field is applied adiabatically (the total entropy value remains unchanged) in a reversible process, the magnetic entropy decreases. Then the temperature decreases because of the total entropy conservation

$$S(T_0, H_0) = S(T_1, H_1) \quad (2.25)$$

$$\Delta T_{ad} = T_1 - T_0 \quad (2.26)$$

This adiabatic temperature rise can be visualized as the difference between the corresponding *S(T,H)* functions and, essentially, represents the MCE measure.

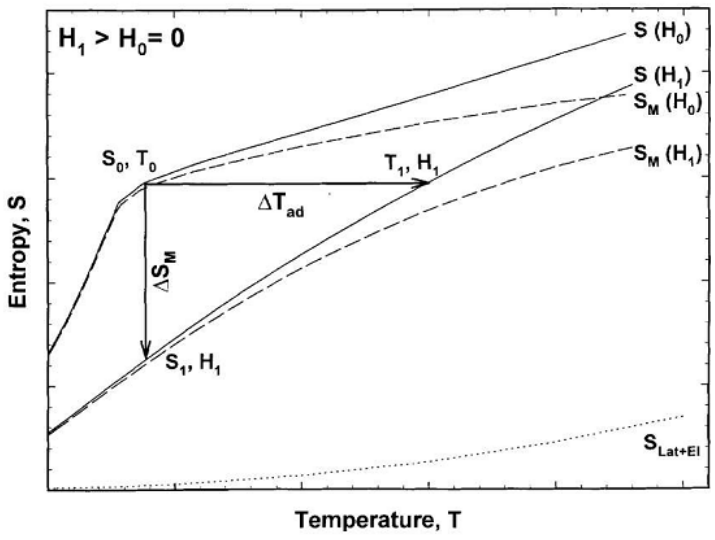

Figure 2.4 *S-T* diagram describing the MCE. Solid lines represent the total entropy in two different magnetic fields. Dotted line shows together the electronic and lattice contributions to the entropy. Dashed lines show the magnetic entropy in two fields. The horizontal and the vertical arrows show ΔT_{ad} and ΔS_M, respectively.

2. Magnetic field is applied isothermally, the total entropy decreases due to the decreasing of the magnetic contribution:

$$\Delta S_M = S(T_0, H_0) - S(T_0, H_1) \quad (2.27)$$

Both the adiabatic temperature change, ΔT_{ad}, and the isothermal magnetic entropy change, ΔS_M, characterize intensity of the MCE. Both quantities are functions of the initial temperature, T_0, and the magnetic field alteration $\Delta H = H_1 - H_0$. Obviously, if the field is switched on, the magnetic order is increasing and ΔS_M has negative value - solid is warming up (ΔT_{ad} >0). For the reverse process, ΔS_M and ΔT_{ad} change their signs and the solid is cooled.

The dependence of MCE parameters ΔS_M and ΔT_{ad} on H, T and magnetization of the material, M is given by one of thermodynamic Maxwell relations:

$$\left(\frac{\partial S(T,H)}{\partial H}\right)_T = \left(\frac{\partial M(T,H)}{\partial T}\right)_H \tag{2.28}$$

After integration for an isothermal process we have the expression for the magnetic entropy change, ΔS_M:

$$\Delta S_M(T,\Delta H) = \int_{H_1}^{H_2}\left(\frac{\partial M(T,H)}{\partial T}\right)_H dH \tag{2.29}$$

Using following thermodynamic relation:

$$\left(\frac{\partial T}{\partial H}\right)_S = -\left(\frac{\partial S}{\partial H}\right)_T\left(\frac{\partial T}{\partial S}\right)_H \tag{2.30}$$

and expression for the heat capacity at constant magnetic field:

$$C_H = T\left(\frac{\partial S}{\partial T}\right)_H \tag{2.31}$$

we obtain the infinitesimal adiabatic temperature change

$$dT_{ad} = -\left(\frac{T}{C(T,H)}\right)_H\left(\frac{\partial M(T,H)}{\partial T}\right)_H dH \tag{2.32}$$

After integration, we can write down the expression for MCE when field change is $\Delta H = H_1 - H_0$:

$$\Delta T_{ad}(T,\Delta H) = -\int_{H_1}^{H_2}\left(\frac{T}{C(T,H)}\right)_H\left(\frac{\partial M(T,H)}{\partial T}\right)_H dH \tag{2.33}$$

Some information about behavior of the MCE in magnetic solids can be obtained by analyzing of afore cited equations:

1. The ΔT_{ad} is positive and ΔS_M is negative for positive field change (ΔH >0) in case of paramagnets and simple ferromagnets (magnetization at constant field decreases with increasing temperature);

2. The absolute value of ΔS_M has peak at $T = T_C$, when $\left|(\partial M / \partial T)_H\right|$ is maximized;

3. Since the heat capacity C_H has an anomalous temperature dependence in vicinity of phase transition, ΔT_{ad} in FM shows a peak at $T = T_C$ even if ΔH tends to zero.

When spontaneous magnetic ordering occurs, the magnetization strongly varies in a very narrow temperature range in the vicinity of the transition temperature, T_N or T_C. In this case, the large value of $\left|(\partial M / \partial T)_H\right|$ allows magnetic materials to have a significant MCE without application of large magnetic field. Thus, the external magnetic field can be used only for temperature shift of the transition temperature.

2.3.3 Measurements of Magnetocaloric Effect

Methods of MCE measurements can be separated into direct and indirect techniques. Direct techniques imply the MCE material to be placed to the magnetic field and the resulting change of temperature ΔT_{ad} is directly measured in some way. In the indirect methods, the MCE is determined from magnetization or heat capacity data. The indirect methods allow calculation of both ΔT_{ad} and ΔS_M unlike the direct methods which usually give only ΔT_{ad} value.

Direct techniques to measure MCE always involve the measurement of the initial (T_0) and final (T_1) temperatures of the sample, when the external magnetic field is changed from an initial (H_0) to a final value (H_1). Then the adiabatic temperature change ΔT_{ad} is simply given by

$$\Delta T_{ad}(T_0, H_1 - H_0) = T_1 - T_0 \qquad (2.34)$$

For the realization of the direct measurement of MCE, a rapid change of the magnetic field is needed. The accuracy of the direct methods depends on the precision of thermometry, field setting, the quality of thermal isolation of the sample, etc.

The magnetic entropy change ΔS_M can be obtained indirectly from magnetization isotherms $M(H)$ at different temperatures by numerical integration of Eq. (2.28) in the desired range of temperatures and magnetic fields (McMichael 1993ab):

$$\left|\Delta S_M\right| = \sum_i \frac{M_i - M_{i+1}}{T_{i+1} - T_1} \cdot \Delta H_i \tag{2.35}$$

Strictly speaking, the last formula can be applicable only in systems with a second-order phase transition because in point of the first-order transition the derivative $\partial M / \partial T$ tends to infinity. However, it happens only in case of ideal first-order transitions and in real materials the Eq. (2.35) can be usually used for MCE calculation even when the first-order transition takes place within the interesting range. Possibility of using (2.35) for the first-order transitions is discussed in (Liu 2007).

The complete set of MCE parameters (ΔT_{ad}, ΔS_M, C) can be obtained from the heat capacity temperature dependences measured in different magnetic fields. The total entropy of a material at temperature T in magnetic field $S(T,H)$ can be calculated from the heat capacity data:

$$S(T,H) = \int_0^T \frac{C(T,H)}{T} dT + S_0 \tag{2.36}$$

where S_0 is the entropy at T=0. Pecharsky and Gschneider (Pecharsky and Gschneidner, Jr. 1999) proposed the equation for the entropy calculation from heat capacity data:

$$S(T,H) = 0.5\left\{C(T_1,H) + \sum_{i=1}^{n-1}\left[\left(\frac{C(T_i,H)}{T_i} + \frac{C(T_{i+1},H)}{T_{i+1}}\right)(T_{i-1} - T_i)\right]\right\} \tag{2.37}$$

where T_1 is starting temperature of measurement and n is the number of measured heat capacity data points between T_1 and T. The isothermal entropy change ΔS_M can be determined as:

$$\Delta S_M(H,T) = S(H,T) - S(0,T) \tag{2.38}$$

and adiabatic temperature change is:

$$\Delta T_{ad} = T(S,H) - T(S,0) \tag{2.39}$$

where $T(S,0)$ and $T(S,H)$ are temperatures at constant total entropy.

2.3.4 Magnetocaloric Effect at first-order magnetic phase transitions

At second-order magnetic phase transitions, the existence of short-range order and spin fluctuations above the T_C causes a reduction in the maximum possible value of $\left|(\partial M / \partial T)_H\right|$ and thus maximum MCE is reduced. In contrast, a first-order phase transition ideally occurs stepwise at constant temperature and the $\left|(\partial M / \partial T)_H\right|$ in this case becomes infinitely large. The discontinuity in the entropy also takes place and is related to the enthalpy of transformation, which is also called latent heat. Thus, in an ideal first-order phase transition, the discontinuity in both magnetization and entropy causes that the derivatives in the mostly used Maxwell relation (Eq. (2.35)) must be replaced by the finite increments of the Clausius-Clapeyron equation for phase transformations:

$$\Delta S = -\Delta M \frac{dH_t}{dT_t} \tag{2.40}$$

where ΔM is the difference in magnetization at transition field H_t between the linear extrapolations of $M(H)$ well above and below the transition.

The existence of entropy change caused by the first-order transition brings an additional contribution to MCE known as giant magnetocaloric effect (GMCE). Intensive search for materials with a field-induced first-order magnetic phase transition for applications has widely been shown in literature (Tegus 2002).

2.4 Relation between volume and magnetism

A number of physical properties of solids depend on interatomic distances. Therefore, experiments under high hydrostatic pressure represent a powerful method for solid state research. The hydrostatic pressure enables to vary the interatomic distances in a compressed matter in a similar extent as the widely used chemical substitution, but, it saves composition, purity and shape of the sample. The pressure induced volume and energy changes are dependent on the compressibility of a particular sample and hence,

the high pressures comparable in magnitude with bulk modulus should be applied to obtain a sufficient effect.

The use of high pressure as a parameter for the investigation of solid state phenomena has become increasingly important during recent years. Physical properties of some special materials under high pressure are an indispensable part of their characterization. Application of the external pressure on materials with magnetic order will result in the changes of magnetic ordering temperatures, magnetic moment values, magnetic structures, magnetocrystalline anisotropy etc.

Approximately 75% of all elements have a magnetic moment in monatomic state but only 32% of them retain their magnetism after condensation to the solid. The question whether an element is magnetic or not depends largely on the number of unpaired electrons that atoms or ions of the element contain. This leads to the "islands of stability" in the magnetic periodic table where the magnetic solid state can be find in the solid state. The first island lies in the transition metals and includes *3d* elements. The *3d* electron shell of these elements can accommodate up to 10 electrons and is progressively filled or moving across the series of elements from scandium (atomic number 21) to zinc (atomic number 30). The other main region of stability is based on the *4f* series: the *4f* electron shell can accommodate 14 electrons and is progressively filled as we move from Lanthanum (atomic number 57) to lutetium (atomic number 71). A third island of stability for magnetic order exists in the region of Oxygen, where the magnetism is a result of the diatomic nature of these elements. The last island of stability of magnetism is represented by the trans-uranium compounds.

The simple expectation that compressing an arbitrary magnetic solid connected with the increase of the atomic density will lead to a suppression of all forms of solid state magnetism as a consequence of the increase of overlap of orbitals and creation of bonds is not correct for all materials. There exists a good counterexample of arising magnetism when the pressure is applied: the Yb can acquire the magnetic moment only at pressure enough for removing of an electron from the completely filled 4*f* shell (Schilling 1984).

The criterion for existence/destruction of the magnetism under pressure was proposed by Schilling (Schilling 1984, 1986). He suggested to use the degree of overlap of neighbouring wave functions α as a parameter which characterizes the magnetic or nonmagnetic state:

$$\alpha = \overline{R}_{SS} / R_{MO} \qquad (2.41)$$

where $\overline{R}_{SS} = V_a^{1/3}/2$ (V_a is the available volume per atom) and R_{MO} is the radius for the maximum in the charge density of the magnetic orbital. Charge densities of two atomic wave functions of neighbouring atoms for the selected 3d-, 4d-, 4f- and 5f-elements are shown in Fig. 2.5 a. The α values for different elements are collected in Fig. 2.5 b. It is seen that the critical value α_C=3.2 separates magnetic elements (top part) from nonmagnetic (bottom part) in a condensed state (except of Cr). The biggest value of α for the rare earth elements implies that their atomic magnetic moment is almost pressure independent whereas a significant pressure effects on the *3d* transition metals and actinides is expected.

Since the magnetic state in solids is strongly correlated with interatomic distances, variation of exchange energy in magnetic materials causes changes of volume and vice versa. The first effect is known as magnetostriction and the second one corresponds to the external pressure applied to the material. The magnetostriction and the pressure changes of magnetization are connected by thermodynamical relation, following from a differentiation of the Gibbs function *G*:

$$\mathrm{d}M/\mathrm{d}P = -\,\mathrm{d}V/\mathrm{d}H \qquad (2.42)$$

where *M* is the saturation magnetization of the sample with volume *V*. The last relation makes it possible to interpret the pressure effect as an inverse one to the magnetostriction.

The saturation magnetization of ferromagnets is also susceptible to the external pressure. Relation between them at temperature *T* is given by the expression:

$$\frac{d\ln M}{dP} = \frac{\left[d\ln M_0/dP - T(d\ln M/dT)(d\ln T_C/dP)\right]}{\left[1+3(\beta/\kappa)(d\ln T_C/dP)\right]} \qquad (2.43)$$

where β is the linear thermal expansion coefficient, κ is the compressibility and T_C is the Curie temperature (Kouvel and Wilson 1961).

The $4f$-wave functions of neighboring rare earth atoms in the solid have negligible overlap, so, the $4f$-electrons thus could not contribute to crystalline binding (Fig. 2.5 a). Hence, they remain localized and the earth atoms conserve the magnetic moment after condensation into solid. Except of Eu and Yb, originally divalent rare earths became trivalent after their condensation into a solid.

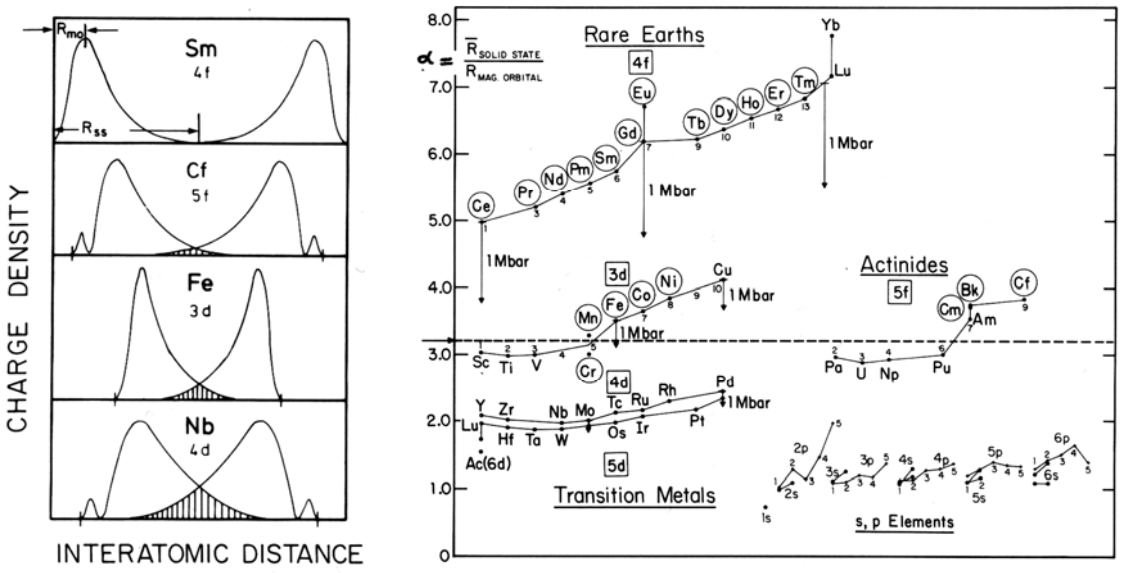

a) **b)**

Figure 2.5 a) Charge density versus distance from nucleus for two atoms at their nearest neighbour separation in the solid. b) Overlap parameter α between neighbouring wave functions in solids. The value of α is shown for all elements in the periodic table with Z ≤ 98 (Schilling 1984).

The *4f*-series of rare earth elements are also the most successful in retaining their magnetism in a solid. The *4f* shell is relatively closely bound to the nucleus of the atom and so, the electrons are shielded by the either $5s^2$-$5p^6$ electrons and, to some extend, by the three 5*d*-6*s* valence electrons. This leads to the negligible orbital overlap and the well-localized and stable nature of the magnetic state. However, pressure induced decrease of interatomic distances bring the *4f*-ions so close together that their *4f* wave functions begin to overlap, leading to *4f* band formation and a contribution to crystalline binding. As long as the Stoner criterion (that the product of density of states *N(Ef)* and exchange interaction I is greater than 1) is fulfilled, *4f* band magnetism is still possible. On the other hand, the band broadening at higher pressures leads to decrease in the density of states and loss of magnetism. For the $4f$-electrons, the transition from a localized to a delocalized state can take place at pressure of several Mbars, thus, the magnetic properties of the rare earth elements can be considered exceptionally in frame of the model for localized magnetism (see Sec. 2.1).

In the framework of the Heisenberg model, the magnetic ordering temperatures $T_{C,N}$ is connected with the magnetic moment, μ, and exchange integral, $J_{i,j}$:

$$J_{i,j} = 3k_B T_{C,N} / 2zS(S+1) \qquad (2.44)$$

where k_B is the Boltzmann constant, *z* is a number of nearest neighbours. Taking into account negligible pressure dependence of the μ, the ordering temperatures is mainly

caused by the pressure influence on the exchange integral $J_{i,j}$. A logarithmical relation between changes of ordering temperature and volume can be written:

$$\mathrm{d}\ln J / \mathrm{d}\ln V = \mathrm{d}\ln T_{C,N} / \mathrm{d}\ln V = \Gamma \qquad (2.45)$$

where Γ is the dimensionless magnetic Grüneisen coefficient (Kamarád 2001).

3 Experimental details

3.1 Sample preparation and characterization

All samples were obtained from University of Zaragoza (Zaragoza, Spain). The polycrystalline samples were synthesized by arc melting of 99.9 wt % pure rare-earth and 99.9999 wt % pure Si and Ge under a high-purity argon atmosphere. The quality of all samples was checked by means of room-temperature X-Ray diffraction and scanning electron microscopy.

In the alloys with nominal composition $Gd_5(Si_xGe_{1-x})_4$ (x=0, 0.1), the X-ray pattern confirms the presence of an orthorhombic main phase (*Pnma*) with unit-cell parameters: a = 7.6946(5) Å, b = 14.826(1) Å, c = 7.7814(4) Å (x=0) and a = 7.6887(1) Å, b = 14.827(2) Å and c = 7.7785(1) Å (x = 0.1). In both samples, the presence of a small amount of impurity phase (~6-7%) were detected. The impurity phases were identified as hexagonal $Gd_5(Si,Ge)_3$ and Gd_5Ge_3 for x=0.1 and x=0, respectively. More details on these samples preparation and characterization can be found in (Magen 2003a, Morellon 1998a).

The $Tb_5Si_2Ge_2$ alloy crystallizes in the monoclinic $P112_1/a$ structure with unit cell parameters: a=7.5088(6)Å, b=14.653(1)Å, c=7.7147(7) and γ=93.00(1)°. The X-ray diffraction measurements confirmed existence of minor amounts of secondary 5:3 (~5%) and 1:1 (~10%) phases within the main phase. For details, see Ref. (Ritter 2002).

The $Nd_5Si_{1.45}Ge_{2.55}$ and $Pr_5Si_{1.5}Ge_{2.5}$ samples were remelted several times after alloying to ensure homogeneity. According to the X-ray diffraction, both samples were essentially single-phase with a room-temperature monoclinic $P112_1/a$ crystallographic structure, in agreement with the crystallographic phase diagrams reported by Yang *et al* (Yang 2002c). Magnetic characterization performed in SQUID magnetometer registered a small anomaly on the magnetization curves at T=115 K and T=32K in cases of $Nd_5Si_{1.45}Ge_{2.55}$ and $Pr_5Si_{1.5}Ge_{2.5}$ alloys, respectively. The anomaly can be corresponded to an impurity phase with higher T_C unrecognizable by X-ray diffraction (Magen 2004).

3.2 High Pressure Techniques

All measurements under hydrostatic pressure (pressure is directed everywhere normal to the sample surface) were performed in piston-cylinder clamped cells of different types. All of them consist of a cylindrical body closed by piston and plug. Most of the cell's parts are made of Cu-Be bronze. High elastic strength of this material is almost temperature independent and mechanical properties remain appropriate down to very low temperatures. Additionally, the CuBe bronze is a non-magnetic material that allows minimizing the influence of the cell on the obtained results of magnetic measurements.

A low viscosity mixture of mineral oils is been used as a pressure-transmitting medium. At room temperature it solidifies under pressure of about 13 kbar which limits the range of applicable pressures. The pressure in the cell can be changed at room temperature only.

The difference between thermal expansions of the cell and the pressure-transmitting medium causes the pressure changes during temperature scan cycle. Such a variation has to be taken into account in order to obtain real pressure values at given temperatures. With temperature change of ΔT, the pressure variation ΔP is given by:

$$\Delta P_T = (1/k_{oil}) \times (\beta_{oil} - \beta_{CuBe}) \times \Delta T \qquad 3.1$$

where $\beta_{oil} = 72\times10^{-5}$ K^{-1} and $\beta_{CuBe} = 4.9\times10^{-5}$ K^{-1} are the thermal expansion coefficients of the oil and CuBe bronze, respectively, and $k_{oil} = 60\times10^{-3}$ kb^{-1} is a compressibility of the oil. The change of pressure ΔP_T does not depend on the cell space and for our cells the following relation was derived:

$$\Delta P_T\,(\text{bar}) = 11.2 \times \Delta T\,(\text{K}) \qquad 3.2$$

Temperature dependencies of the pressure changes ΔP for the mixture of oil (OL 3) and for the Fluorinert FC-77 are presented in Fig. 3.1.

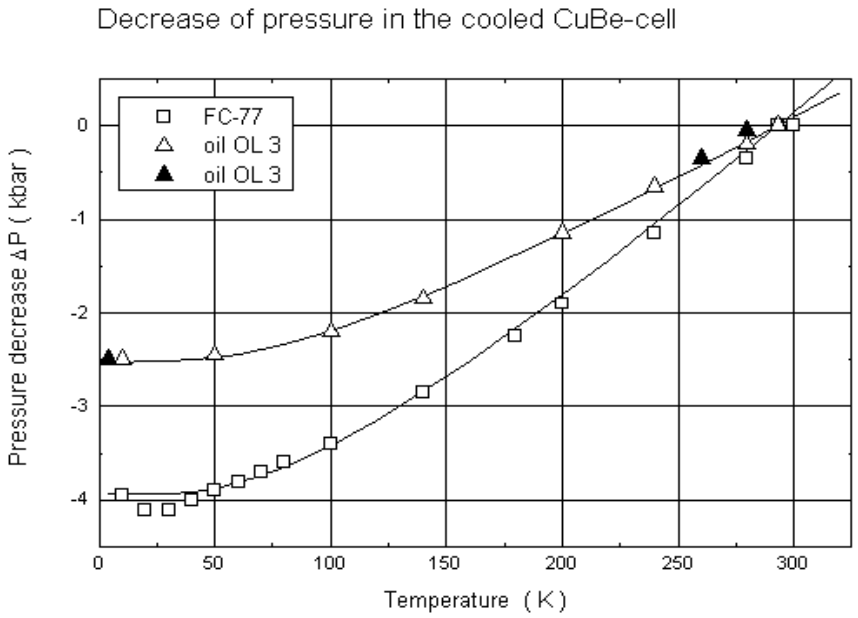

Figure 3.1 Decrease of pressure in the cell cooled from the room temperature.

3.2.1 Miniature pressure cell for the Magnetic Measurements.

Magnetization measurements under hydrostatic pressure were performed in commercial SQUID magnetometer (Quantum Design) in miniature pressure cell. The outer and inner diameters of the cell make 8.5 and 2.5 mm, respectively. The outer size is given by a probe area of the magnetometer. The inner one should ensure only elastic deformation of the cell at maximum pressure inside which is 9.5 kbar at temperature 4 K. The construction of the miniature pressure cell is schematically presented in Fig. 3.2.

The sample (4) is glued to the sample holder which is screwed into plug (2). The plug (2) is sealed by two rubber and one copper rings (3) and clamped by the upper bolt (1). The piston (6) is sealed by the Bridgeman mushroom-type sealing. The pressure is produced by screwing the bolt (8) and pushing the piston (6) into the cell. Pressure magnitude inside the cell is determined using a small amount of lead. Lead has a transition to superconducting state at about 7K. The critical temperature of transition T_C can be shifted to lower value by external pressure. T_C is been determined by sharp decrease of magnetic susceptibility to negative value at cooling down (Fig. 3.3),

corresponding to the diamagnetic superconducting state of lead (Garfinkel and Marother 1961, Smith 1969, Reich and Godin 1996). The superconducting temperature T_C decreases with applied pressure as $dT_C / dP = -4.05 \times 10^{-2}$ K/kbar and the pressure value is calculated as $P(kbar) = \{T_C(0) - T_C(P)\} / 0.0405$.

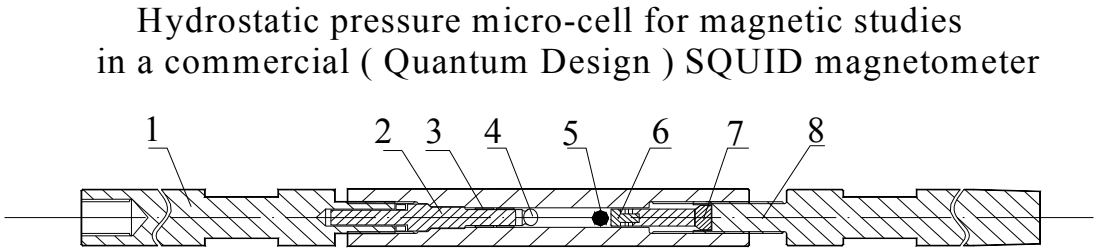

Figure 3.2 Hydrostatic piston-cylinder pressure micro-cell produced by High Pressure Laboratory, IP ASCR for magnetic studies in the commercial SQUID magnetometer (Quantum Design Co.).

(1), (8) upper and lower pressure clamping bolts; (2) wireless plug; (3) seals; (4) sample; (5) Lead pressure sensor; (6) piston; (7) piston backup.

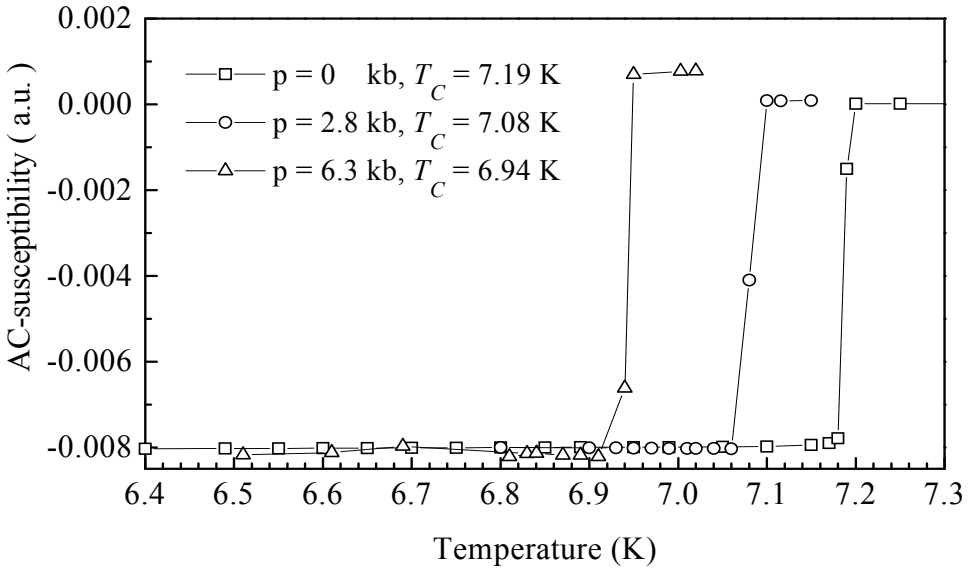

Figure 3.3 Temperature dependence of the ac-susceptibility of the Pb pressure sensor for several applied pressures.

The influence of the CuBe cell on the magnetization results in the SQUID magnetometer was tested by Kamarád (Kamarád 1997) on a sample of Y_2Fe_{17} intermetallic compound. The difference between data obtained with and without cell at ambient pressure was less then 0.2% in temperature range from 5 K up to 200 K. Precision of dc-susceptibility measurements was estimated by experiment with Pd in magnetic field up to 50 kOe. The difference at ambient pressure was up to 1.5%.

3.2.2 Standard piston-cylinder cell

The compressibility and thermal expansion measurements under pressure were realized in a close-cycle refrigerator. Hydrostatic pressure up to 12 kbar was produced using the standard piston-cylinder CuBe pressure cell. The outer diameter of the cell is 36 mm, the inner one is 8 mm and the length is 155 mm. Internal arrangement of the standard pressure cell is schematically represented in Fig. 3.4.

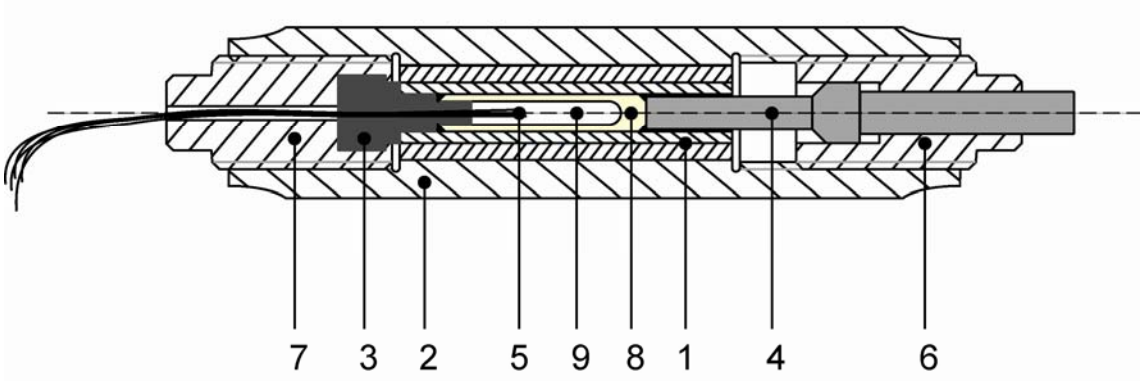

Figure 3.4 Standard piston-cylinder pressure cell

(1) inner cell body; (2) outer cell body; (3) plug with a conical lead-through; (4) piston; (5) wiring to the sample and pressure sensor; (6),(7) upper and lower clamping bolts; (8) Teflon container; (9) transmitting medium.

The plug (3) with a conical lead-through gives possibility to measure electrical signals inside the cell. The copper wires (5) connect the sample and Manganin pressure sensor located inside the cell with measuring equipment. The sample is located inside the Teflon container (8) sealed by copper rings. The clamping force is applied to the piston (4) by hydraulic press. When the desirable pressure is created, a position of the piston in the cell body is been fixed by bolt (6). By its opposite side, the bolt (7) is connected with a cooling head of the close-cycle refrigerator. A small amount of apiezon is placed between the head and the bolt for a better thermal contact.

For the standard cell, a coil of Manganin wire can be used as a pressure sensor due to the almost linear pressure dependence of resistance of Manganin. (Bridgman 1952):

$$R(T,P) = R(T,O)\{1+\alpha(T)P\} \qquad 3.3$$

and the expression for pressure is:

$$P = \frac{R(T,P)-R(T,0)}{R(T,0)}\frac{1}{\alpha(T)} \qquad 3.4$$

where $R(T,P)$ and $R(T,0)$ are the values of the electrical resistance of the Manganin coil corresponding to the pressure P and ambient pressure at temperature T. $\alpha(T)$ is the pressure coefficient of resistance of the Manganin. This coefficient depends on the diameter and composition of the Manganin wires. Its values for wires that are being used are collected in Table 3.1.

Table 3.1 Characteristics of the Manganin sensors (Arnold 1994).

∅ wire, mm	Composition, wt. % Cu - Mn - Ni	α (273 K), 10^{-3}kbar^{-1}	$1/\alpha\, d\alpha/dT$, 10^{-4} K^{-1}
0.04	84.41 - 12.56 - 3.03	2.447	1.8
0.05	85.64 - 12.28 - 2.08	2.569	3.4
0.10	85.56 - 12.38 - 2.06	2.517	a2.3

Additionally to the pressure dependence, the Manganin resistance largely depends on temperature. Temperature dependencies of 120 Ω coil at initial 9 kbar and ambient pressure are depicted in Fig. 3.5. For the correct pressure definition below room temperature, the difference between two curves at temperature T should be used in formula 3.4.

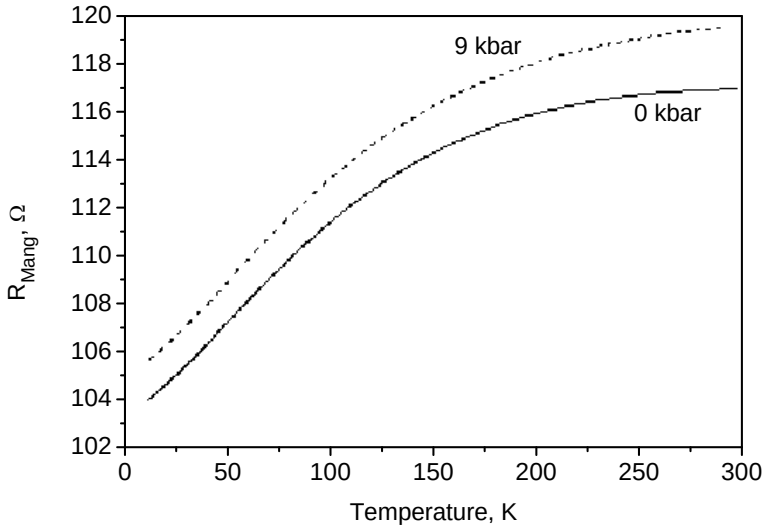

Figure 3.5 The temperature dependencies of the electrical resistance of Manganin pressure sensor at normal and 9 kb pressures.

We used the Manganin wire with silk winding for the pressure sensors. Its usual resistance is about 100 Ω. After the wire has been reeled up to a coil, it should be annealed at 120°C for 60-80 hours to minimize the residual winding strains in the wire.

3.3 Experimental Methods

3.3.1 Thermal expansion and compressibility measurements under pressure

Measurements of the compressibility and thermal expansion under pressure were made using the calibrated micro-strain gauges (Micro-Measurements Division, Measurements Group, Inc.) in the standard cell. The thermal expansion was measured in the Close Cycle Refrigerator System. The Refrigerator allows measurements in temperature range 3.5 - 320 K. Assuming the polycrystalline samples to be homogeneous with negligible texture of crystal grains, a simple relation for the volume changes can be written down:

$$\Delta V / V = 3\Delta L / L_0 = 3\frac{\Delta R / R_0 + f(T,P)}{G(T,P)} \qquad 3.5$$

where R_0 and ΔR are electrical resistance of the micro-strain gauge and its pressure and temperature change, respectively. A gauge factor $G(T, p)$ and a correction function $f(T,P)$ of the strain gauges were calibrated by the thermal expansion and compressibility measurements on pure Cu, Fe and SiO_2 (Kamarad 1995).

For better accuracy, the compressibility measurement of pure Cu was performed simultaneously with the sample measurement. In this case, comparison of measured value of Cu compressibility with its well-known value of 0.73 $Mbar^{-1}$ allows to make appropriate corrections to the compressibility results.

3.3.2 Magnetic measurements

All the magnetization measurements were performed in the SQUID magnetometer (Quantum Design Co.) installed at the Institute of Physics AS CR. The SQUID is a flux-to-voltage converter. The changes of magnetic flux are detected in a pair of superconducting coils when the sample moves through these coupled coils. An

obtained voltage response curve is fitted to a SQUID calibration curve (a voltage response curve for a defined point magnetic moment) and the magnetic moment of the sample is derived. The SQUID magnetometer operates over temperature range 2-400 K with applied DC fields up to H_{ext} = ± 50 kOe. To eliminate an effect of the samples shape the demagnetization field is taken into account in the data processing, using the relation:

$$H_{int} = H_{ext} - 4\pi N M \qquad 3.6$$

where N is demagnetizing factor and M is magnetization of the sample.

For the ac-susceptibility measurements, an ac magnetic field with amplitude of up to 20 Oe and frequency of up to 100 Hz was used.

Details of the magnetization measurements and data processing are as follows:

- the isothermal magnetization curves of samples were measured at magnetic fields from 0 Oe to 50 kOe (in the hysteresis mode - without any field oscillations) at stabilized temperatures which were changed step-by-step;
- the saturation magnetization, M_S, has been determined as an linear extrapolation of high-field part of the magnetization curve back to the field $H = 0$, (intersection with the vertical axis);
- the detailed temperature dependencies of M were measured in static magnetic field (in the persistent mode) at stabilized temperatures which were changed step-by-step (from 1 K to 10 K each) in desirable temperature range;
- due to the changes of internal pressure with temperature, data of the mentioned temperature dependencies were obtained at varying magnitudes of pressure; consequently, they were recalculated on uniform pressure.

3.3.3 Specific heat measurements

The Specific Heat measurements were realized using the commercial PPMS (Quatum Design) experimental setup installed in Joint Laboratory for Magnetic studies (Charles University, Prague). Its cryostat system allows operating in temperature range 0.3-400K. Temperature is measured using a calibrated Cernox thin film resistance sensor. The sample is attached to an insulating platform inside the brass container by thin Apiezon layer for better thermal contact (Fig. 3.6). The resistive heater and the

thermometer are attached to the bottom of the sample platform. The platform is suspended on thin wires which also provide electrical connection to the heater and thermometer and thermal connection to the sample. The container with the sample is placed into vacuum chamber pumped by turbo-molecular pump.

All the specific heat measurements were performed by relaxation heat-pulse method (Bachmann 1972). The Figure 3.7 shows a measuring cycle for one heat-capacity value. At the beginning the sample and the frame are at the same temperature T_1 (time period before t_1). Then electrical current is supplied to the heater of the sample holder. The heating power P causes the temperature increasing until a stationary temperature T_2 is reached (time period t_1 - t_2).

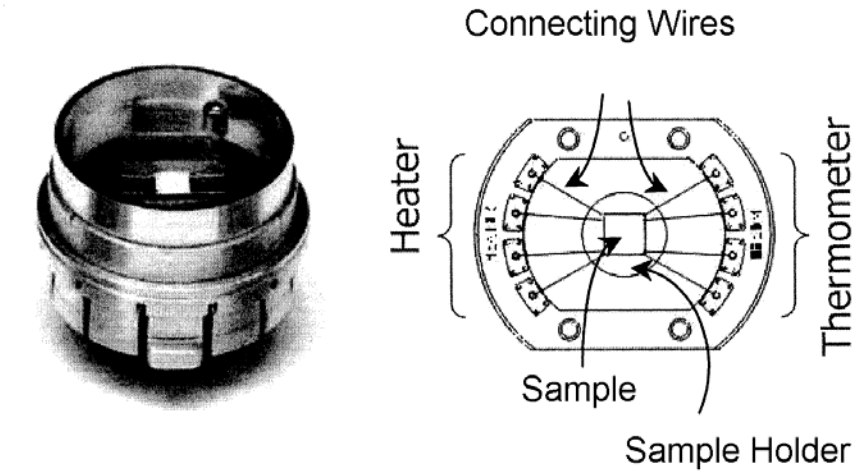

Figure 3.6 Schematic drawing of the sample mounting for the heat capacity measurement

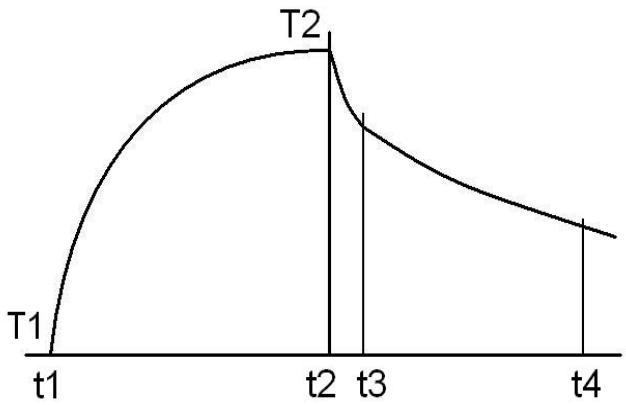

Figure 3.7 A plot of temperature versus time in a relaxation measurement

The power P is now equal to the heat dissipation per time unit through the electrical wires and by radiation (minor importance). After the power has been turned off, the

temperature decays to the original temperature T_1 by the exponential law. In this case, the one dimensional heat-flow equation can be written:

$$k(T - T_1) + C(T)\frac{dT}{dt} = P \qquad 3.7$$

where k is value of the heat links, can be determined from equation:

$$k = \frac{P}{T_2 - T_1} \qquad 3.8$$

The solution of (3.7) for the cooling curve ($P = 0$, time interval t_2-t_4 Fig. 3.7) is:

$$T(t) = T_1 + (T_2 - T_1)\exp\left(-\frac{t}{\tau}\right) \qquad 3.9$$

where the time constant of the thermal relaxation τ is determined using the fitting procedure and the heat capacity can be determined as

$$C = k\tau \qquad 3.10$$

In these expressions, the heat diffusion from the center of the sample through the wires is considered to be much faster than the heat diffusion in the wires. Such situation is realized in case if the thermal conductance of the sample is much higher compared to that of the wires and sample has a good thermal contact with sample holder (the internal relaxation time τ_2 is small compared with τ_1 related to the heat link). Otherwise, *T*(t) must be represented by a more complicated sum of exponential curves with two time constants τ_1 and τ_2 (the t_2-t_4 period is separated on t_2-t_3 and t_3-t_4). In this case, the set of equations for the sample and the sample holder should be written:

$$\begin{cases} C_{sh}\dfrac{dT_{sh}}{dt} = P(t) - k_w(T_{sh}(t) - T_1) + k_{s-sh}(T_s(t) - T_{sh}(t)) \\ C_s\dfrac{dT_s}{dt} = -k_{s-sh}(T_s(t) - T_{sh}(t)) \end{cases} \qquad 3.11$$

where k_{s-sh} and k_w are thermal conductance between the sample and sample holder via Apiezon and conductance of wires, respectively. C_s and C_{sh} are heat capacities of the sample and sample holder ($C = C_s + C_{sh}$) and T_s is temperature of the sample. Solution of the equation set (3.11) for time period t_2-t_4 is:

$$T(t) = T_1 + \left(T_2(t) - T_1\right)\exp\left(-\frac{t}{\tau_1}\right) - \left(T_2(t) - T_s\right)\exp\left(-\frac{t}{\tau_2}\right) \qquad 3.12$$

The τ_2-effect was discussed in details by Bachmann *et. al.* (Bachmann *et. al.* 1972).

4 $R_5(Si_xGe_{1-x})_4$ compounds

Synthesis and structural characterization of the first R_5T_4 compounds (R-rare earth, T – Si,Ge) was performed in 1966 (Smith, Tharp, Johnson 1966). All of these compounds have a multilayered crystallographic structure created by layers of the rare-earth atoms interleaved by Si-Ge layers accordingly to a certain sequence (Pecharsky and Gschneidner, Jr. 2001). The inter-layer (3D) and intra-layer (2D) exchange interactions play a definitive role in formation of magnetic structure and magnetic transitions. Silicides were mostly ferromagnets and germanides ordered antiferromagnetically. Gd_5Si_4 ordered ferromagnetically at 336 K, more than 40 K higher than undiluted metallic Gd. Unfortunately sparse research work, mainly on crystal and structure determination was devoted to this system in the forthcoming 30 years.

In 1997, Pecharsky and Gschneidner discovered a giant magnetocaloric effect (GMCE) in $Gd_5(Si_xGe_{1-x})_4$ alloys (Pecharsky and Gschneidner, Jr. 1997abcd, 1998). For $Gd_5Si_2Ge_2$ (Pecharsky and Gschneidner, Jr. 1997a), the magnetic entropy change, ΔS_M, derived from magnetization measurements using the Maxwell relation (Eq.(2.28)) yielded a value twice larger than that of Gd which has the best MCE near the room temperature known before. With the measurements of the heat capacity as a function of T and H, the giant value of ΔS_M was confirmed and the adiabatic temperature change, ΔT_a, as a function of T was evaluated, giving rise to a narrower and 30% higher peak in comparison with pure Gd. In order to understand such unusual magnetocaloric properties of this system, Pecharsky and Gschneidner studied compounds $Gd_5(Si_xGe_{1-x})_4$ in the whole composition range $0 \le x \le 1$. A comparison of ΔS_M for $Gd_5(Si_xGe_{1-x})_4$ compounds with other magnetocaloric materials is given in Fig. 4.1.

$R_5(Si_xGe_{1-x})_4$ compounds with rare-earth elements, other than Gd, also attracted a great deal of interest in recent time. Presence of the reversible first-order magnetostructural transition in certain members of the $R_5(Si_xGe_{1-x})_4$ series results in an impressive number of unusual physical properties: colossal magnetostriction (Morellon 2000, 1998a, Nazih 2003), giant magnetoresistance (Morellon 1998b, 2001a, Levin 1999, 2000a), unusual Hall effect (Stankiewicz 2000), spontaneous generation of voltage (Levin 2001a, Sousa 2002) and giant magnetocaloric effect.

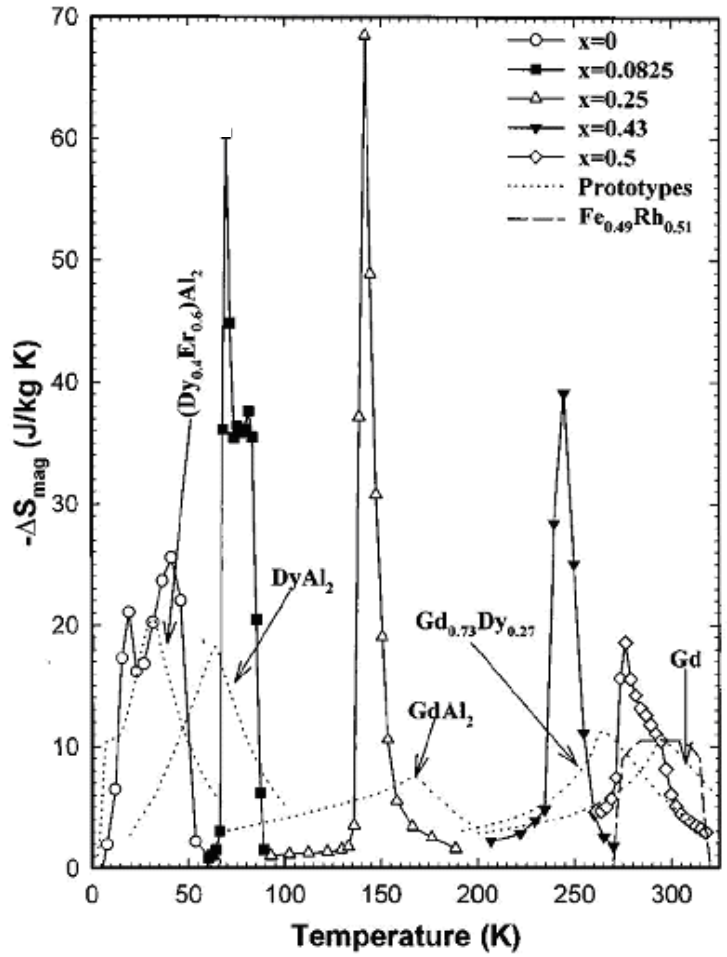

Figure 4.1 comparison of the ΔSM value for $Gd_5(Si_xGe_{x-1})$ compounds and the best other magnetic refrigerants (Pecharsky and Gschneidner 1997b).

4.1 Gd-based $R_5(Si_xGe_{1-x})_4$ compounds

4.1.1 Crystal Structure of $Gd_5(Si_xGe_{1-x})_4$

The crystal structure of $Gd_5(Si_xGe_{x-1})_4$ compounds can be considered as succession of two-dimensional layers (slabs) consistent of distorted cubes and trigonal prisms with common faces (Fig. 4.2) (Choe *et. al.* 2000). The Gd atom (blue circle) at the center of each cube is surrounded by six Si/Ge atoms. Four of them (green circles) occupy the trigonal prisms and create intraslab bonds. Two others (red circles) are located outside the slab and bonding two different slabs. The crystallographic structure and physical properties of the alloy are controlled by covalent-like bonds and thus by

the distances between namely the "red" Si/Ge atoms. Since the Si and Ge atoms have different atomic radii, the distances between atoms (and thus, the crystallographic structure) can be modified by changing the Si/Ge ratio in the alloy.

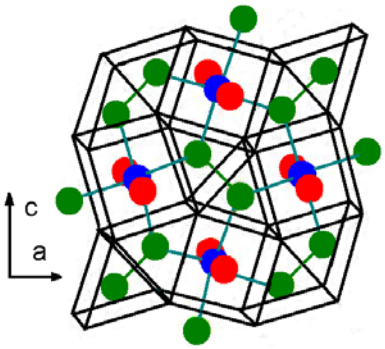

Figure 4.2 Projection of the crystallographic structure of Gd alloys on the a-c plain. Blue circles depict the Gd atoms. Green and red circles depict the Si/Ge atoms inside and outside the basic building slabs, respectively (Choe *et. al.* 2000).

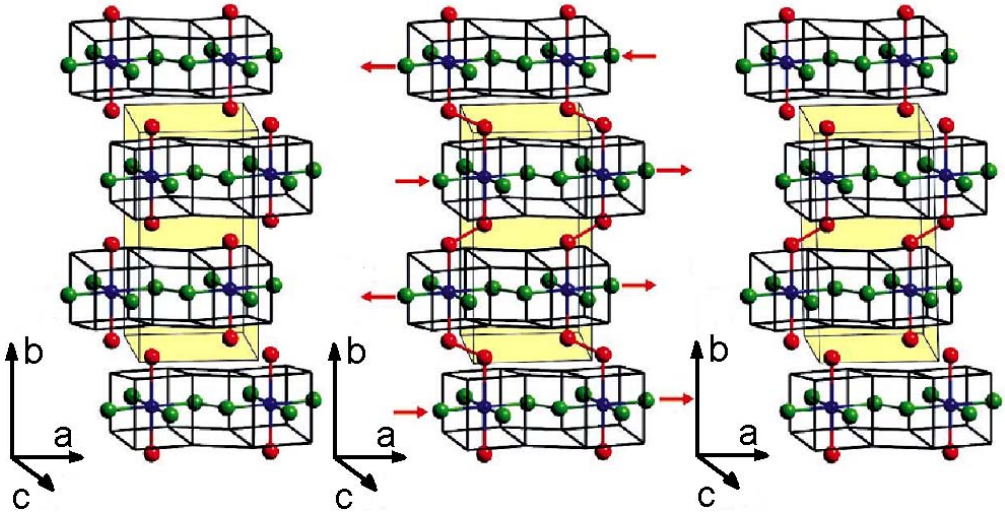

a)
Orthorhombic *O(II)*
Pnma
0≤x≤0.3

b)
Orthorhombic *O(I)*
Pnma
0.575≤x≤1

c)
Monoclinic *M*
$P112_1/a$
0.4≤x≤0.503

Figure 4.3 Crystallographic structure of $Gd_5(Si,Ge)_4$ alloys: a) Sm_5Ge_4-type orthorhombic structure *O*(II); b) Gd_5Si_4-type orthorhombic structure *O*(I); c) monoclinic structure M. Red line segments depict the covalent-like interslab bonds. Red arrows indicate the slab displacement in the *O*(I) structure when the transition to other possible phases occurs.

The three structures *O*(I), *M* and *O*(II) are present at room temperature by tuning the Si/Ge ratio from Gd_5Si_4 to Gd_5Ge_4. When all possible bonds are present, the Gd_5Si_4-type orthorhombic structure *O*(I) is stabilized (Fig. 4.3 b) (Choe 2000). Half breaking of the bonds leads to formation of the monoclinic *M* type of structure (Fig. 4.3 c). Finally, totally broken bonds correspond to a Sm_5Ge_4-type orthorhombic structure *O*(II) (Fig. 4.3 a) (Morellon 2000, Choe 2000).

The main difference between the structures is the shift of the atomic positions along the ***a*** axis affecting the distance between bonding Si/Ge atoms (Fig. 4.4) (Pecharsky and Gschneidner 1997c).

Since the Si and Ge atoms have different atomic radii, the distances between atoms (and thus, the crystallographic structure) can be modified by changing the Si/Ge ratio in the alloy. The crystallographic structures and the lattice parameters vs. Si content in the $Gd_5(Si_xGe_{x-1})_4$ are presented in Fig. 4.5 (Pecharsky and Gschneidner 1997c)

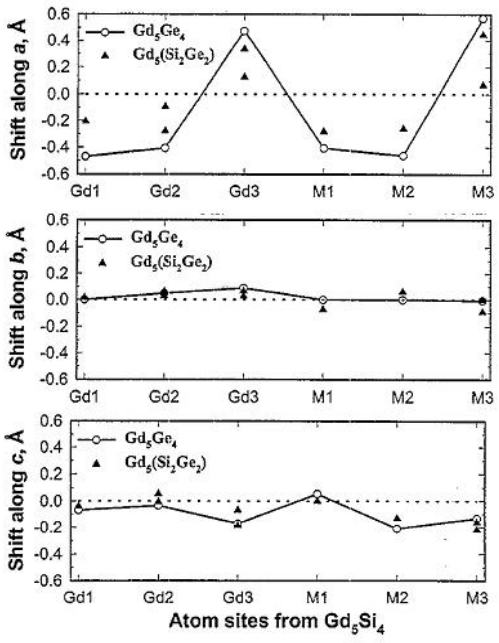

Figure 4.4 The relative atomic shifts along a, b, and c axes in the crystal structures of Gd_5Ge_4 [*O*(II)] and $Gd_5Si_2Ge_2$ (*M*), with respect the positions in Gd_5Si_4 [*O*(I)] structure. M3 are the interslab bonding Si/Ge atoms, M1 and M2 are the other Si/Ge atoms. (Pecharsky and Gschneidner 1997c)

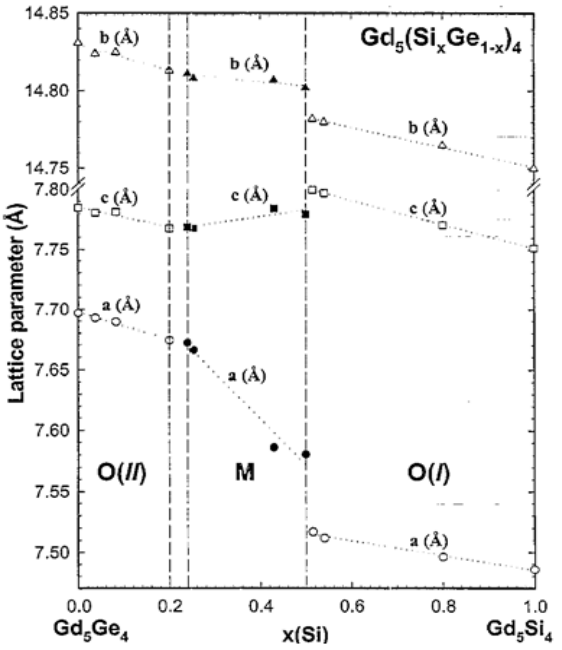

Figure 4.5 Lattice parameters for the $Gd_5(Si_xGe_{1-x})_4$ system at room temperature. The dotted lines are guides to the eye. The dashed lines delineate structural phase regions. (Pecharsky and Gschneidner 1997c)

4.1.2 Magnetism of $Gd_5(Si_xGe_{1-x})_4$ compounds

Magnetism and crystallography in $Gd_5(Si_xGe_{x-1})_4$ are closely related. Choe *et al*. (Choe 2000) investigated this relationship by calculating the exchange parameter *J(R)* between Gd atoms for different phases in $Gd_5Si_2Ge_2$, where *R* is the Gd-Gd distance (Fig. 4.6). They used a nearly free electron model for the conduction band and the RKKY model. It was found that in the *M* phase, *J(R)*>0 for short Gd-Gd distances and *J(R)*<0 for long distances while in the *O*(I) phase *J(R)*>0 for the entire range of Gd-Gd distances. A hypothetical *O*(II) phase (which was not observed in $Gd_5Si_2Ge_2$, see Fig. 4.8) would give *J(R)*<0 for the whole range of *R*.

The ferromagnetic ordering exists only if all slabs are connected by covalent-like bonds, i.e. in the *O*(I) structure (Pecharsky and Gschneidner 2001). As was mentioned in Sec. 2.1, the indirect RKKY *4f-4f* exchange through the *6-s* conducting electrons is responsible for most of the magnetic properties in lanthanide systems. But in the $R_5(Si_xGe_{x-1})_4$ systems, the magnetic FM-PM transition at the crystallographic transition can not be explained only within the RKKY model. Actually, even though a relevant change of the RKKY interaction along the ***a*** axis present due to the "shear" displacement of the layers (distance between bounding Si/Ge atoms changes from 0.8 to 1.1Å (Morellon 1998a, Pecharsky and Gschneidner 2001, Choe 2000), the changes along the ***b*** and ***c*** axes are fairly smaller. Therefore, the overall RKKY interaction is expected to have a minimal variation and can not cause the drastic change of magnetism.

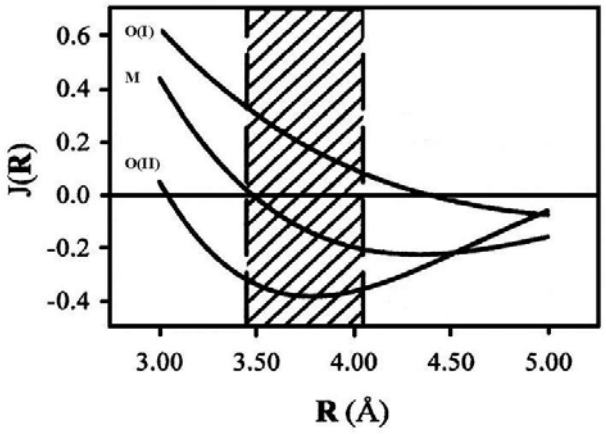

Figure 4.6 Variations of the exchange interaction, *J(R)*, between Gd atoms in $Gd_5Si_2Ge_2$. R is the Gd-Gd distance. Estimated from the RKKY model using a nearly free electron model for the conduction electrons (Choe 2000).

In order to explain the fact of ferromagnetism breaking at the structural transition, Levin *et al*. (Levin 2000b) proposed that ferromagnetism in the *O(I)* ground state exists not only due to the indirect RKKY *4f-4f* interaction, but also due to the Gd-(Ge/Si)-Gd superexchange coupling through the interslab covalent-like bonds. Thus, the breaking of all (or part) of bonds at the structural transformation would explain the destruction of the ferromagnetic coupling in the $Gd_5(Si_xGe_{1-x})_4$ system, since the superexchange interaction should disappear.

Rao (Rao 2000) established an almost linear dependence between T_C and the distance between bonding Si/Ge atoms for the whole composition range ($0<x<1$). The length of the bonds is thus a crucial structural parameter governing the magnetic interactions in these compounds. Therefore, the volume changes can cause significant changes of magnetism. For example, in Gd_5Ge_4 compound three-dimensional exchange interactions between two-dimensional layers are so weak that spontaneous ferromagnetism does not set in zero magnetic field at any temperature. Application of hydrostatic pressure shortens the distances between Si/Ge bounding atoms and the ferromagnetic order is been reached (Fig. 4.7).

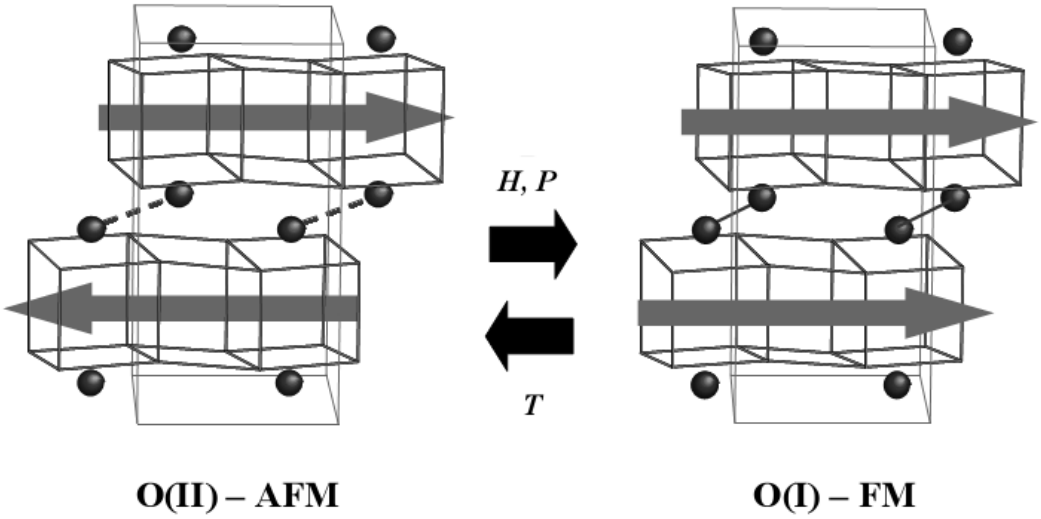

Figure 4.7 Crystallographic and magnetic structures of Gd_5Ge_4 in the a-b plane at low temperature. Only the Ge atoms participating in interlayer covalent-like bonds are depicted as solid spheres. Solid lines stand for formed bonds while dashed lines represent broken bonds. Gray arrows are used to illustrate the change in the magnetic coupling induced by field, hydrostatic pressure or temperature (Magen 2003b).

4.1.3 Magnetostructural phase diagram of $Gd_5(Si_xGe_{1-x})_4$ compounds

The magnetostructural phase diagram of the $Gd_5(Si_xGe_{1-x})_4$ compound at zero field and ambient pressure is presented in Fig. 4.8. It shows three ranges. The Si-rich compounds ($0.5<x\leq1$) have the Gd_5Si_4- type orthorhombic structure with space group *Pnma* (*O*(I)). A second-order transition between PM and FM magnetic states occurs in this case at T_C which changes from 280K for x=0.5 to 340K for x=1 (Pecharsky and Gschneidner 1997bc, 1998). The crystallographic structure remains unchanged during this transition. In the intermediate composition range ($0.24\leq x\leq0.5$), a first-order magneto-structural phase transition occurs from a high-temperature PM monoclinic *M* (space group $P112_1/a$) to a low-temperature FM phase with the same *O*(I) structure as the Si-rich compounds. In this composition region the temperature of transition linearly increase from 130K for x=0.24 to 276K for x=0.5 (Pecharsky and Gschneidner 1997b, Morellon 1998a, Nazih 2003). For the Ge-rich compounds ($x\leq0.2$), a second-order PM-AFM transition occurs at T_N, changing from 125K for x=0 to 135K for x=0.2. Since the neutron scattering cannot be performed easily on Gd-based compounds, the nature of the AFM phase in is currently under discussion (Morellon 2000). A phenomenological description of the first-order magnetostructural transition on the basis of Landau-Devonshire theory is given in (Teng 2002) (see also Sec.2.2 of the thesis).

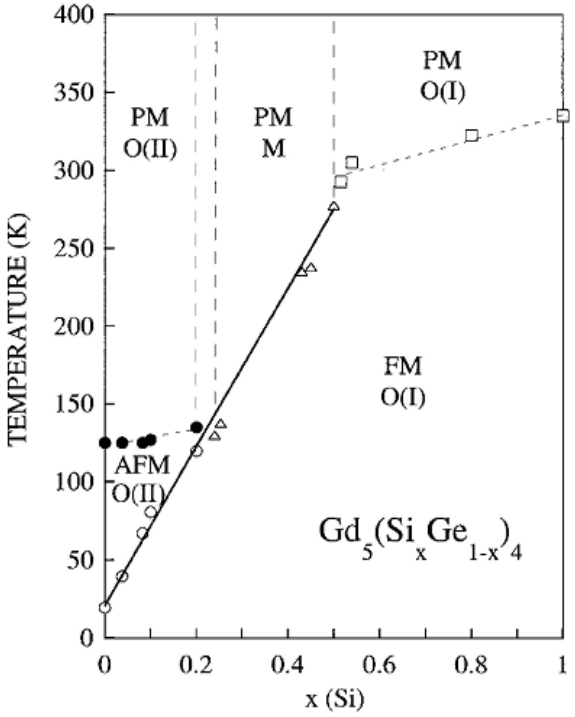

Figure 4.8
Magnetic and crystallographic phase diagram at zero field, for $Gd_5(Si_xGe_{1-x})_4$ alloys (Morellon 2000). PM stands for paramagnetic phase, FM for ferromagnetic phase and AFM for antiferromagnetic phase. M stands for monoclinic structure, *O*(I) for Gd_5Si_4–type orthorhombic structure and *O*(II) for Gd5Ge4-type orthorhombic structure. A solid line signifies the first-order phase transition.

With further cooling, a first-order transition to the FM phase arises. T_C in this case linearly changes from approximately 20 K for x=0 to 120 K for x=0.2. The AFM-FM transition occurs simultaneously with a first-order structural transformation from a high-temperature Sm_5Ge_4-type orthorhombic (space group *Pnma*) phase structure, *O*(II), to the low-temperature *O*(I) (Morellon 2000). In this case the symmetry remains unchanged but the transformation is accompanied by significant changes of the lattice parameters and atomic positions. In the composition range $0.2<x<0.24$, where the second-order PM-AFM transition disappears, the *O*(II) and *M* structures coexist (Pecharsky and Gschneidner 1997c). In both the Ge-rich and intermediate composition regions, the first-order transition may be induced reversibly by application of external magnetic field (Pecharsky and Gschneidner 1997b, Morellon 2000, Morellon 1998a) or hydrostatic pressure (Morellon 1998a, Magen 2003b) which both linearly increase the temperature of transition.

The neutron diffraction experiments are the most relevant for determination of magnetostructural relationships. However, the huge neutron absorption cross-section of the most of Gd isotopes makes impossible neutron measurements of the Gd-based compounds. In recent time, $R_5(Si_x,Ge_{1-x})_4$ compounds with other rare-earths are also a subject of intensive research. All the diversity of crystal structures found in the Gd-based compounds is reproduced in most systems with other rare-earth. Additionally, a high-symmetry Zr_5Si_4-type tetragonal structure with the space group $P4_12_12$ has been found in the Si-rich composition range in alloys with light rare-earth (La, Ce, Pr, Nd).

4.2 Other $R_5(Si_xGe_{1-x})_4$ compounds

4.2.1 $Tb_5(Si_xGe_{1-x})_4$ compounds

$Tb_5(Si_xGe_{1-x})_4$ is the second best studied series where a comprehensive neutron diffraction characterization has been possible due to the absence of Gd. The crystal structure and basic characteristics of magnetic phase transitions in binary T_5Si_4 and Tb_5Ge_4 compounds were reported by Holtzberg *et al*. (Holtzberg 1967). Information about magnetic and magnetocaloric properties of Tb_5Si_4 can be found in

(Spichkin 2001, Serdyuk 1982). Electrical resistance study was performed by Y.D.Yao *et al*. (Yao 2003). Results of the neutron diffraction experiments on $Tb_5(Si_xGe_{1-x})_4$ were published in (Ritter 2002, Garlea 2005). The magnetic and crystallographic temperature-composition phase diagram of $Tb_5(Si_xGe_{1-x})_4$ compounds is depicted in Fig. 4.9 (Ritter 2002).

As in the Gd-based $R_5(Si_xGe_{1-x})_4$, three different crystallographic structures are been observed at room temperature. The orthorhombic *Pnma* Gd_5Si_4-type (*O*(I)) and Gd_5Ge_4-type (*O*(II)) structures stabilize in Si-reach and Ge-reach compounds, respectively (Morellon 2000). The intermediate concentration range ($0.35<x<0.65$) has monoclinic $P112_1/a$ type of structure.

On cooling down, the system goes through a second order phase transition (upper doted lines in Fig. 4.9) from paramagnetic PM to either a complex ferromagnetic structure (Si-rich region, FM1 in Fig. 4.9) or to an antiferromagnetic phase (Ge-rich region, AFM). In both cases, the crystallographic structure remains unchanged. The solid line depicts a first-order magnetostructural transition in monoclinic alloys from PM-*M* to the FM1-*O*(I) phase. At lower temperatures, a second magnetic phase transition occurs in whole composition range (bottom doted line in Fig. 4.9). In Ge-rich alloys AFM1 phase turns to AFM2 via spin reorientation, and in other cases, the magnetic mode mixing leads to the FM2 phase formation (Ritter 2002).

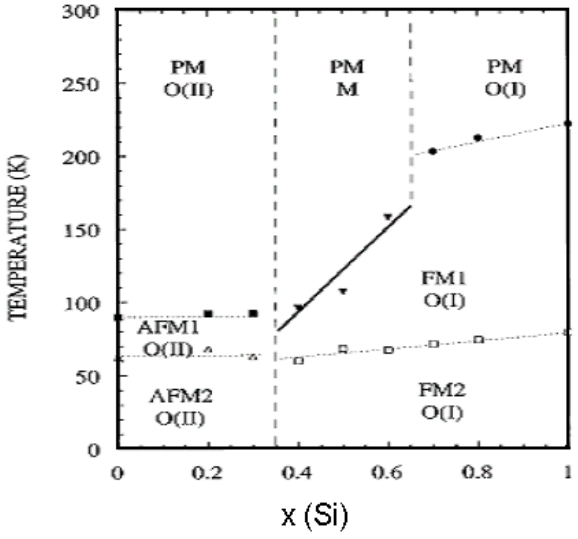

Figure 4.9. Magnetic and crystallographic phase diagram of the $Tb_5(Si_xGe_{1-x})_4$ systems. The transition temperatures have been taken from magnetic susceptibility measurements (Ritter *et al*. 2002).

A large magnetic entropy change in intermediate composition range of $Tb_5(Si_xGe_{1-x})_4$ makes these systems important candidates for magnetic refrigeration applications (Morellon 2001b). Here, the MCE is connected with first-order

magnetostructural transition from paramagnetic monoclinic to orthorhombic ferromagnetic phase (Fig. 4.9). In compound with x=0.5 (i.e. $Tb_5Si_2Ge_2$), the magnetic entropy change reaches value 36.4 $J*Kg^{-1}K^{-1}$ in magnetic field 120 kOe near T_C which is comparable with giant MCE in Gd-based alloys.

4.2.2 Nd- and Pr-based compounds

The relationship between crystallographic structure and Si/Ge concentration in Nd-based $R_5(Si_xGe_{1-x})_4$ was studied by Yang *et al.* by means of X-ray powder diffraction (Yang 2002b). The tetragonal Zr_5Si_4 and the orthorhombic Sm_5Ge_4 structures were reported for the Nd_5Si_4 and Nd_5Ge_4 compounds, respectively. Substitution of 25% of Si by Ge with respect to the Nd_5Si_4 compound (i.e. Nd_5Si_3Ge) also leads to the orthorhombic Sm_5Ge_4 type of structure. Further addition of Ge up to $Nd_5Si_2Ge_2$ stabilizes the monoclinic $Gd_5Si_2Ge_2$ type structure. At the Nd_5SiGe_3 composition both monoclinic and orthorhombic phases coexist.

The magnetic and magnetocaloric properties of selected (x = 0, 0.25, 0.5, 0.75, 1) Nd-based $R_5(Si_xGe_{1-x})_4$ systems was reviewed by Gschneidner *et al*. in (Gschneidner 2000). T_C of the $Nd_5(Si_xGe_{1-x})_4$ alloys changes with concentration gradually from 52 K for Nd_5Ge_4 to 73 K for Nd_5Si_4 except the orthorhombic Nd_5Si_3Ge which has the T_C above 120K. Significantly higher T_C is associated with structures that have all (four per unit cell) bond (Si/Ge)-(Si/Ge) pairs. Phases with reduced number of bonding pairs order magnetically at significantly lower temperatures. The MCE is relatively small which is typical for a second-order phase transition. Basic magnetic parameters of selected $Nd_5(Si_xGe_{1-x})_4$ alloys are collected in Table 4.1.

The information about Pr-based compounds was reported by Yang *et al.* in (Yang 2002c). There are three structurally distinct phase regions exist in these systems. The Si-rich compounds ($0.6625 \leq x \leq 1$) crystallize in the Zr_5Si_4-type tetragonal structure with space group $P4_12_12$. For the Ge-rich compounds ($0 \leq x \leq 0.275$) the Sm5Ge4-type orthorhombic structure with space group *Pnma* was reported. The $Gd_5Si_2Ge_2$-type monoclinic structure with space group $P112/a$ corresponds to the intermediate region of concentrations extending from $x \approx 0.35$ to $x \approx 0.5875$. The lattice parameters and the unit cell volume in dependence on x are presented in Fig. 4.11 a and b, respectively.

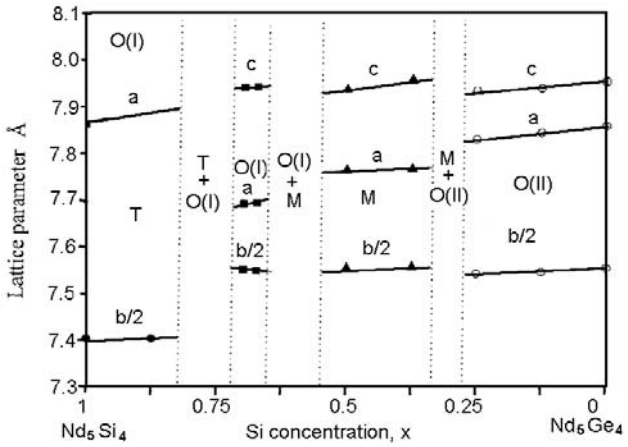

a)

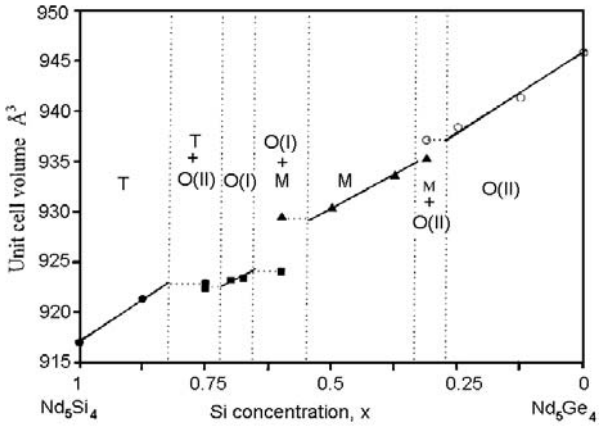

b)

Figure 4.10. Dependence of the lattice parameters **a)** and the unit cell volume **b)** on Si content in the $Nd_5(Si_xGe_{1-x})_4$ alloys. The lines are guides for the eye. The dashed lines delineate phase regions, where *T* and *O* are the tetragonal-based and orthorhombic-based solid solutions, respectively, and *M* is the ternary monoclinic intermediate phase.

Table 4.1 Magnetic properties of some $Nd_5(Si_xGe_{1-x})_4$.

Composition	Cryst. structure	T_C, K	θ_P, K	P_{eff}/Nd, μ_B	-ΔSM, (J/kg*K)
Nd_5Si_4	Tetragonal	71	74	3.39	8.3
Nd_5Si_3Ge	Orthorhombic	124	122.6	3.15	6.4
$Nd_5Si_2Ge_2$	Monoclinic	65	61.6	4.27	5.6
Nd_5SiGe_3	Two phases	52, 61	58.1	3.41	4.1
Nd_5Ge_4	Orthorhombic	55	52.1	3.55	6.4

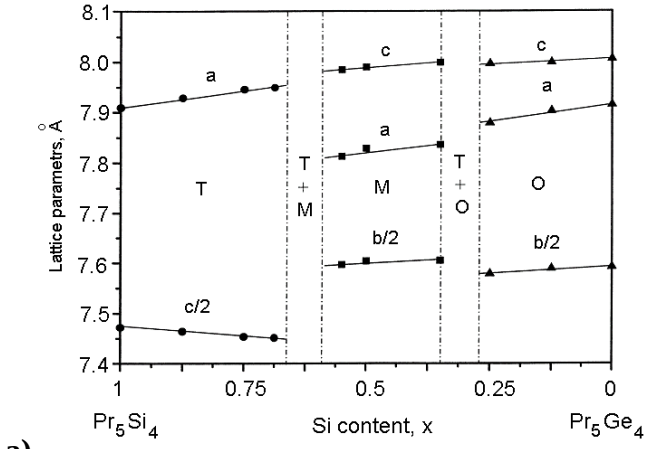

a)

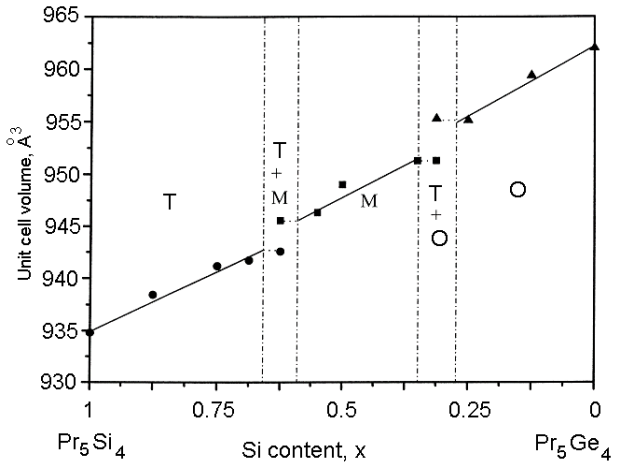

b)

Figure 4.11. Dependence of the lattice parameters (a) and the unit cell volume (b) on Si content in the $Pr_5(Si_xGe_{1-x})_4$ systems. The lines are guides for the eye. The dashed lines delineate phase regions, where *T* and *O* are the tetragonal-based and orthorhombic-based solid solutions, respectively, and *M* is the ternary monoclinic intermediate phase.

5 Results and discussions

5.1 Gd_5Ge_4 compound

The Gd_5Ge_4 has complex Sm_5Ge_4-type orthorhombic structure at room temperature (Morellon 2000). On cooling down, this compound orders antiferromagnetically at ~ 128 K (Magen 2003a). In contrast with magnetic behavior of other Gd-based Ge-rich compounds ($0 < x \leq 0.3$), the FM order was not observed in Gd_5Ge_4 in zero magnetic field down to the lowest measured temperatures (Levin 2001b, 2002). Magnetization, magnetostriction and electrical resistivity studies point to a field induced structural transition coupled with a transformation to a collinear ferromagnet below 30 K, but only when the magnetic field exceeds 10 kOe. This field-induced transition from AFM *O*(II) to FM *O*(I) is irreversible below 10 K and becomes fully reversible at ~20 K. The complex magnetic field-temperature phase diagram of Gd_5Ge_4 is presented in (Magen 2003a).

The effect of high hydrostatic pressure is expected to be similar to the Si doping (increasing *x*, decreasing of the unit cell volume), therefore we may expect an enhancement of the interlayer interaction leading to formation of FM *O*(I) phase. However, effects of chemical and hydrostatic pressure can be quite different (Morellon 2004). The aim of our study was to test the possibility to induce the structural transition coupled with creation of FM correlation in Gd_5Ge_4 only by applying high hydrostatic pressure and to explore changes of its magnetic and magnetocaloric properties upon applying of hydrostatic pressure.

5.1.1 Magnetoelastic properties under high pressure

The structural behavior of Gd_5Ge_4 was studied by the LTE and compressibility measurements under selected hydrostatic pressures up to 11 kbar. The LTE was measured in temperature range 5-160 K on heating using method described in Sec.3.3.1,

results are present in Fig. 5.1. The zero-pressure and 1 kbar curves are almost identical and have a weak anomaly below 40 K. At higher pressure, a clear jump arises and becomes larger upon further increasing of pressure. Accordingly to the magnetostriction measurements reported in (Magen 2003a), the jump reflects the existence of the pressure-induced *O*(I)-FM phase with smaller unit cell volume. The amount of this phase is proportional to the jump magnitude. The critical temperature T_C determined from the maximum of the LTE coefficient vs. *T* dependences (Fig. 5.2) increases at a rate dTc/dP = +4.6(8) K/kbar.

The relative volume changes under pressure were measured at room temperature (Fig. 5.3). The volume of the sample changes nonlinearly with pressure in range 0–12 kbar. The calculated compressibility value at low pressures (up to 4 kbar) $k = -(1/V)dV/dP = 1.84$ Mbar^{-1} is well compared with other $Gd_5(Si_xGe_{1-x})$ alloys (Morellon 2004). Compressibility at lower temperatures was determined using the LTE data. Its value at 100 K is reduced to 1.47 Mbar^{-1}.

Taking into account the difference in volume between spontaneous *O*(II) and field-induced *O*(I) phases in Gd_5Ge_4 (Pecharsky 2003) and the volume compressibility value, we can expect that at pressure over 6 kbar the *O*(I)-FM ground state should be stabilized in the majority of the sample.

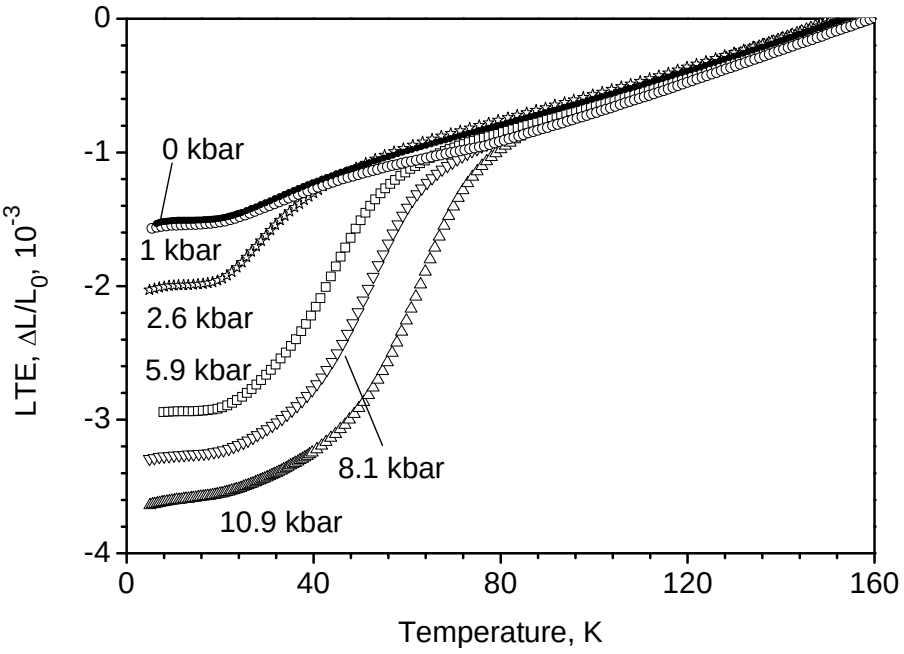

Figure 5.1 Linear thermal expansion of Gd_5Ge_4 as a function of temperature under selected values of applied hydrostatic pressures. The pressure values are the actual ones near transition temperature.

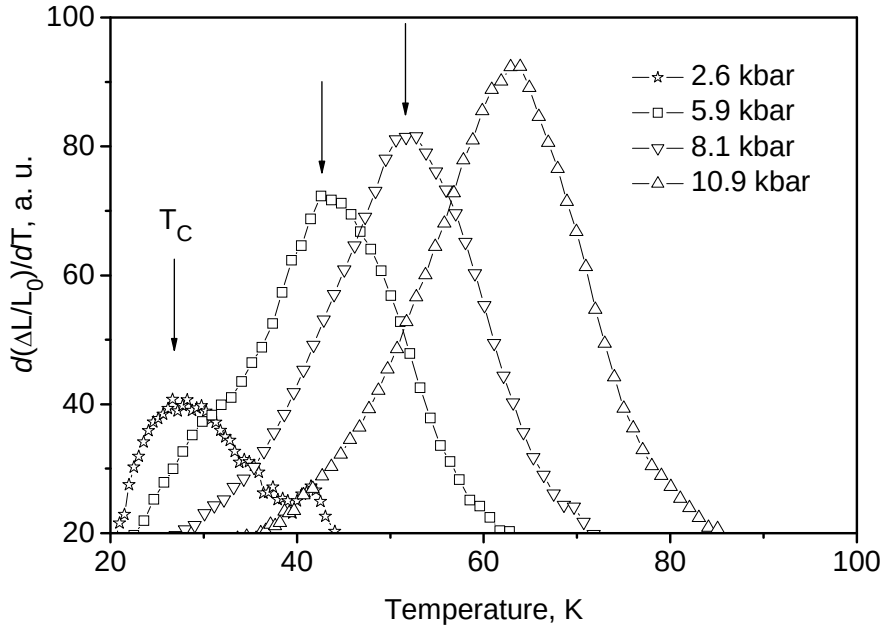

Figure 5.2 Evolution of T_C in Gd_5Ge_4 upon increasing pressure from 2.6 to 10.9 kbar.

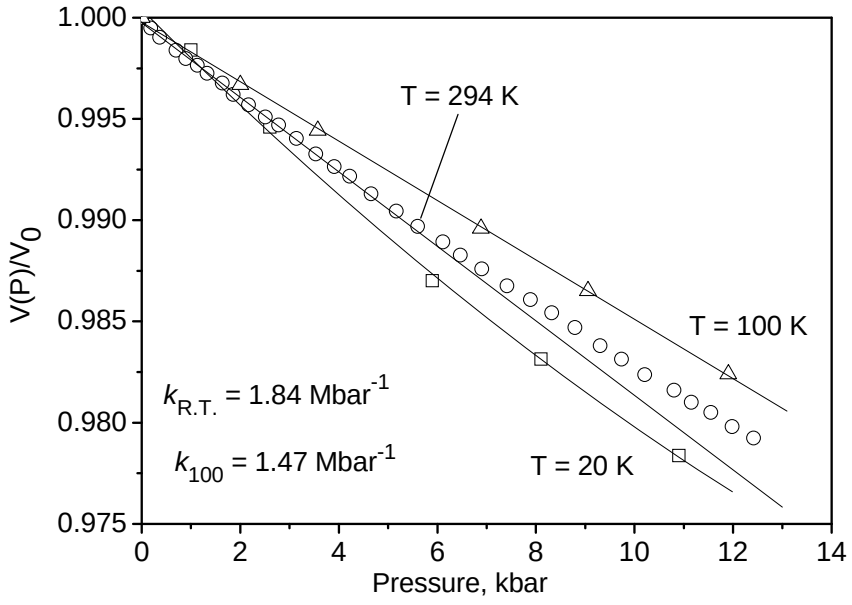

Figure 5.3 The relative change in volume of the sample at selected temperatures. The room temperature dependence is obtained directly by gradual loading of the pressure cell in the hydraulic press. The low-temperature dependencies were obtained indirectly from the LTE measurements under pressure.

5.1.2 Magnetic properties under high pressure

To correlate the structural behavior with magnetism, we have performed measurements of magnetic properties of Gd_5Ge_4 as function of temperature, applied magnetic field and hydrostatic pressure. The magnetic susceptibility was measured in ac field H_{ac} = 1 Oe and frequency f_{ac} =50 Hz under different hydrostatic pressures (Fig. 5.4). The transition temperature of the impurity 5:3 phase (~46 K at P=0) does not change significantly under pressure.

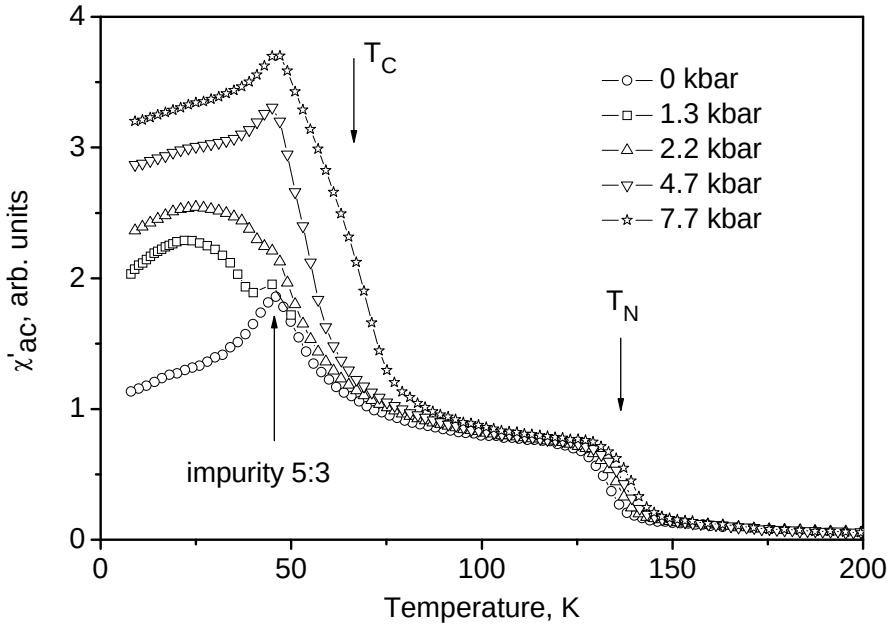

Figure 5.4 Temperature dependencies of the ac susceptibility obtained on heating after zero-field cooling at different values of hydrostatic pressure. H_{ac}= 1 Oe, f_{ac} = 50 Hz

The values of dT_C/dP and dT_N/dP obtained from the susceptibility data are 5.3(3) and 0.6(9) K/kbar, respectively (Fig. 5.5). Values of both T_C and T_N increase with pressure. Significantly different slopes, significant increase of Curie temperature with pressure and only moderate pressure changes of Neel temperature are in qualitative agreement with concentration dependencies of this two transitions as is presented in Fig. 4.8.

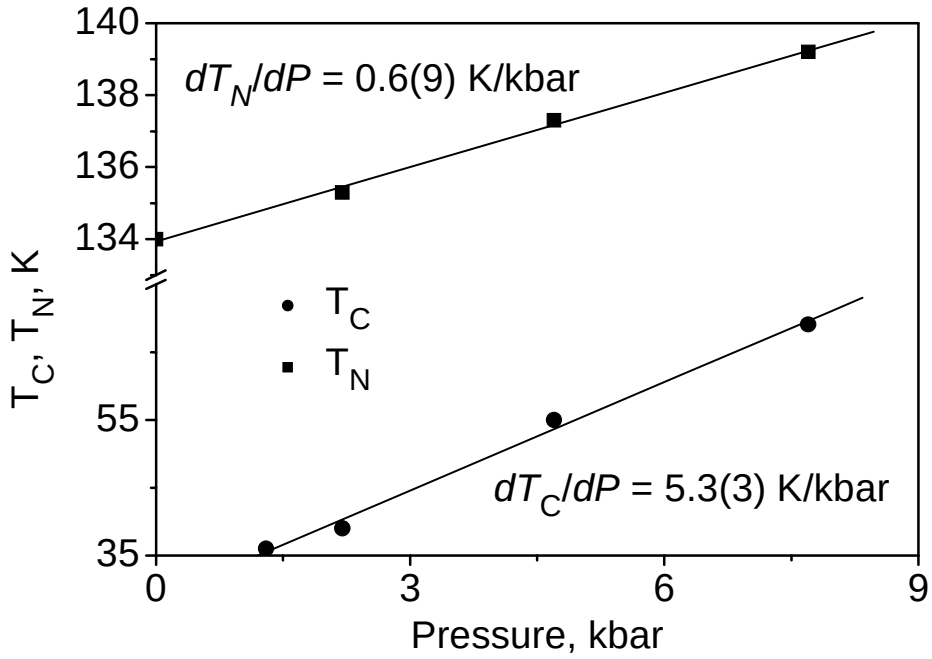

Figure 5.5 Pressure induced changes of transition temperatures T_C and T_N in Gd_5Ge_4.

Temperature dependence of the low-field magnetization at pressures 0, 1.3 and 8 kbar are displayed in Fig. 5.6. The temperature scan was performed in *dc* magnetic field of 500 Oe which is much lower than the lowest critical field (~ 11 kOe) needed to induce the FM phase at any temperatures and in selected values of pressure. At ambient pressure, no FM state was detected down to 5 K in agreement with (Levin 2001b, 2002). The isothermal application and removal of 50 kOe field at 5 K induces a FM state which is reflected in increase of magnetization up to 18.5 emu/g. The FM signal remains pronounced on following heating up to 15 K. An applied hydrostatic pressure of 1.3 kbar is sufficient to induce the AFM-FM transition at ~37 K on heating (~30 K on cooling) in the absence of significant magnetic field. In this case, the induced FM signal is much lower than that obtained after application of 50 kOe at ambient pressure. If the magnetic field has been applied and removed at 1.3 kbar, a full FM signal is recovered. Therefore, taking into account results in Fig. 5.1 we can suppose that the sample volume at 1.3 kbar is spatially segregated into *O*(II)-AFM and *O*(I)-FM phases. At 8 kbar, the low-temperature FM signal is close to maximum and T_C is shifted to 69 K on heating and 63 K on cooling.

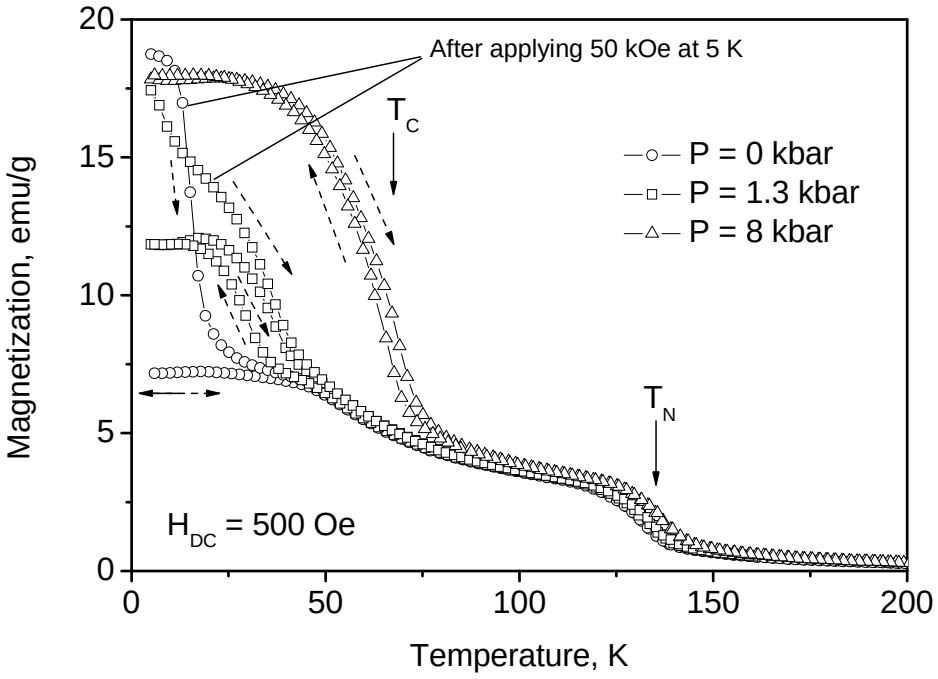

Figure 5.6 Magnetization of Gd_5Ge_4 in field 500 Oe as a function of temperature under selected values of the applied hydrostatic pressure. The values of pressure at ~7 K are shown. Dashed arrows indicate the direction of temperature change.

In order to confirm the enhancement of interlayer FM correlation under pressure and justify presence of the *O*(I)-FM phase within the *O*(II)-AFM ground state, we have measured magnetization isotherms at selected temperatures and applied pressures. The results at 5 K and selected pressures 0, 1.3, 2.2, 4.7 and 7.7 kbar are presented in Fig. 5.7 and Fig. 5.8. The sharp metamagnetic AFM-FM transition was observed at ambient pressure (weak low-field FM signal is related to the impurity 5:3 phase). Upon increasing pressure, magnetization isotherms get smoother and low-field FM signal becomes more pronounced confirming an existence of mixed *O*(I)-FM/*O*(II)-AFM state. At higher fields, the AFM regions transform irreversibly into FM ones that are reflected in a wide hysteresis. The temperature dependencies of critical field of the field-induced metamagnetic transition at 0 and 1.3 kbar are displayed in (Fig. 5.5).

The relative amount of pressure-induced *O*(I)-FM phase (Fig. 5.9) can be estimated from the saturation of FM components as indicated in Fig. 5.7 and Fig. 5.8 for different pressures. The percentage has been corrected by ~ -10% to take into account the FM signal from the saturation of the 5:3 impurity and the increase in the magnetization in the AFM phase upon field increasing.

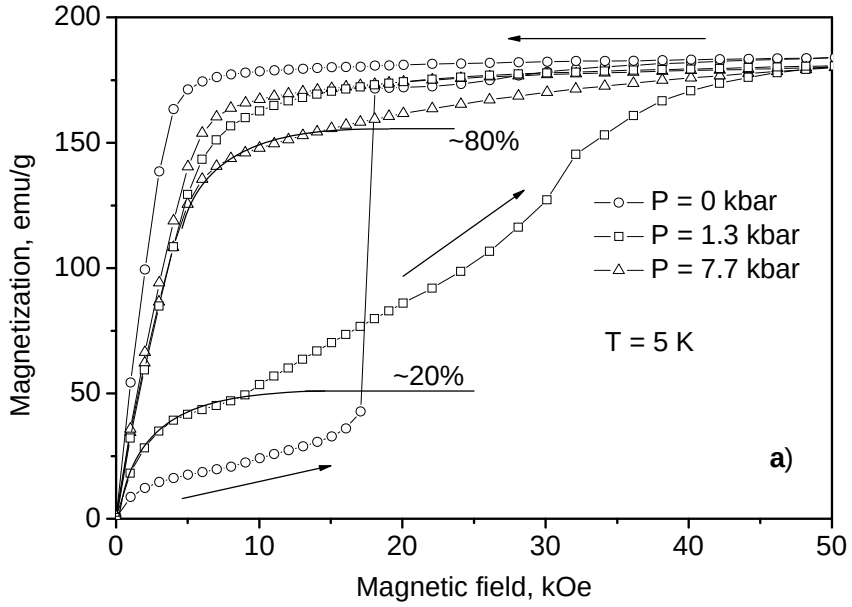

Figure 5.7 Magnetization isotherms at 5 K in Gd_5Ge_4 under selected values of the applied hydrostatic pressure of 0, 1.3, 7.7 kbar. The ambient-pressure curve was obtained without pressure cell. The pressure values are taken in vicinity of transition of the Pb pressure sensor to superconducting state, i.e. ~7 K.

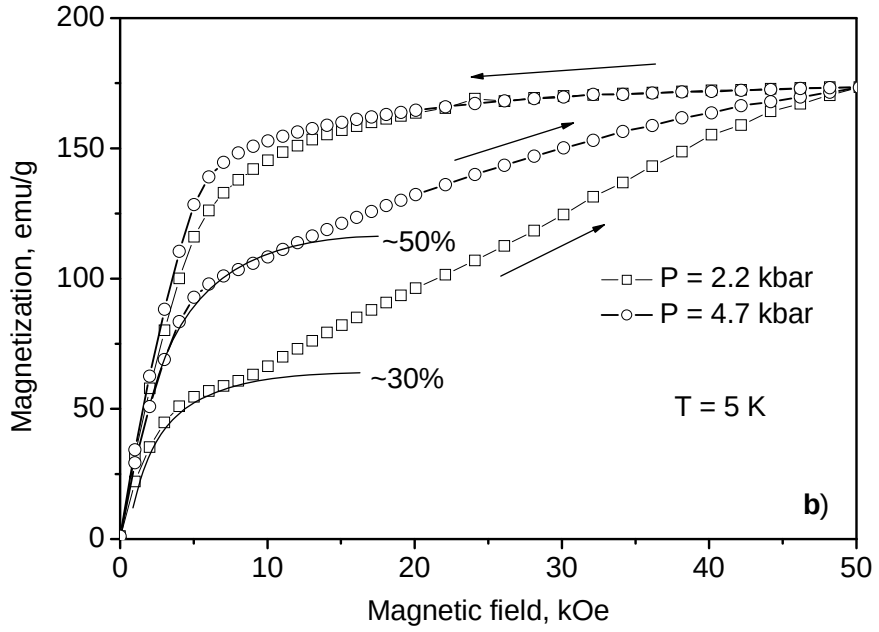

Figure 5.8 Magnetization isotherms at 5 K in Gd_5Ge_4 under selected values of the applied hydrostatic pressure of 2.2 and 4.7 kbar. The pressure values are taken in vicinity of transition of the Pb pressure sensor to superconducting state, i.e. ~7 K.

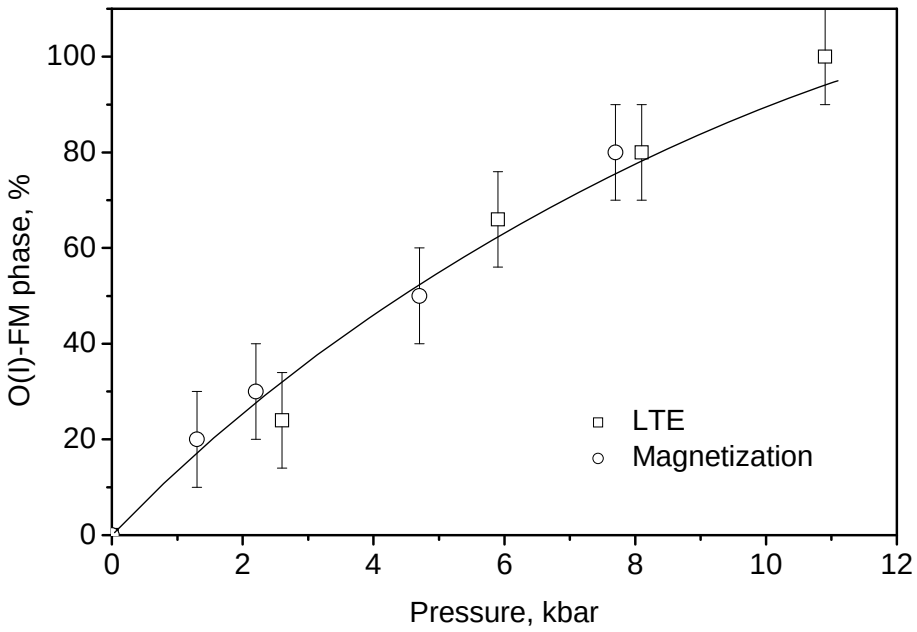

Figure 5.9 Percentage of pressure induced *O*(I)-FM phase as estimated from LTE and magnetization measurements. The line is a guide for the eye.

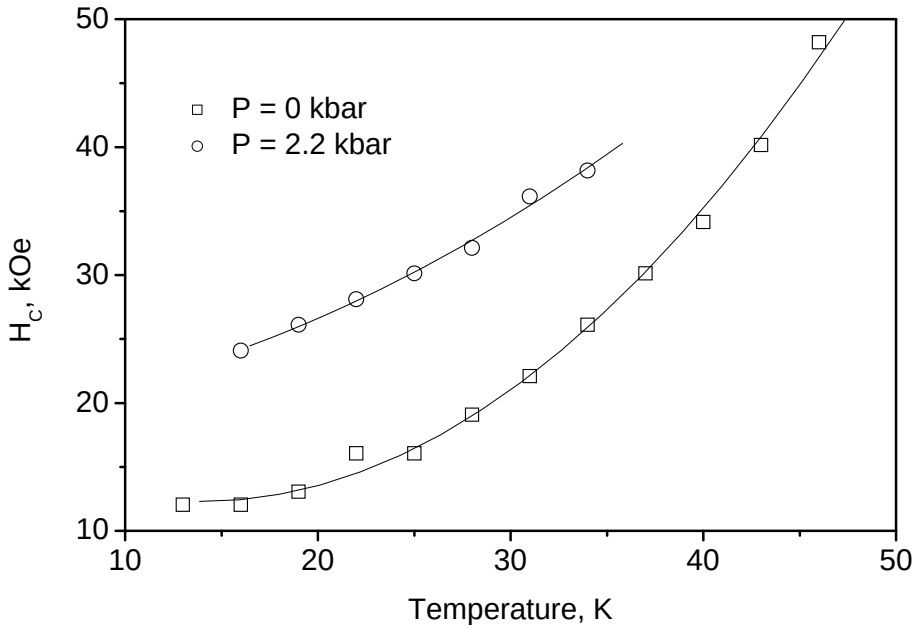

Figure 5.10 Temperature dependence of transition field H_C of the first-order field-induced magnetostructural transition in Gd_5Ge_4 at pressures 0 and 2.2 kbar. The lines are guides for the eye.

5.1.3 Magnetocaloric effect under high pressure

To examine if the formation of pressure-induced *O*(I)-FM phase has influenced the magnetocaloric properties of Gd_5Ge_4 we performed the study of magnetocaloric effect under high hydrostatic pressure. To calculate magnetic entropy changes ΔS_M under different pressures, magnetization isotherms on increasing field up to 50 kOe were measured from 16 to 100 K with a temperature step 3 K. Measurements were performed under selected values of hydrostatic pressure 0, 2.2, 3.7 and 8.7 kbar (Fig. 5.11). Taking into account the irreversibility of the AFM-FM transition, the sample was warmed up to the PM state (~150 K) after each magnetization-demagnetization cycle.

At zero pressure (Fig. 5.11,a), curves from 16 to 49 K exhibit a jump in magnetization corresponding to the first-order field-induced magnetostructural transition. The transition field H_C is defined as inflection point of magnetization curves within the transition region. The ambient pressure results are comparable with those obtained before by means of magnetostriction and heat capacity measurements (Levin 2001b, Magen 2003a). On increasing pressure, the shape of the magnetization isotherms is significantly changed. At 2.2 kbar (Fig. 5.11 b), presence of the pressure induced *O*(I)-FM phase is reflected in increasing of the low-field (up to 10 kOe) magnetization in temperature range 16-55 K. The sharp magnetization jump is now replaced by sinuosity of the magnetization curves from 16 to 40 K indicating the field-induced transition in the rest of the AFM phase. At pressure 3.7 kbar (Fig. 5.11,c), the anomaly connected with AFM-FM transition disappears, but the slope of the magnetization curves significantly differs from the FM behavior. At maximal pressure of 8.7 kbar , (Fig. 5.11 d) the magnetization curves have typical FM shape that is attributed to formation of the FM phase in majority of the sample.

The temperature dependencies of ΔS_M are calculated indirectly from the magnetization data, results are presented in Fig. 5.12. At zero pressure, the ΔS_M can be calculated using both Clausius-Clapeyron (Eq.(2.40) and Maxwell (Eq.(2.35) formulas. The first one evaluates real values entropy change ΔS_{MCC} associated with a first-order transition (solid circles in Fig. 5.12 a). Since the transition takes place in a narrow field range, the maximum value of ΔS_{MCC} is almost independent on the maximum field H_{max}, when $H_{max} > H_C$ (Fig. 5.10). The ΔS_{MCC} reaches value -17.8 $J \cdot kg^{-1} \cdot K^{-1}$ at 40 K.

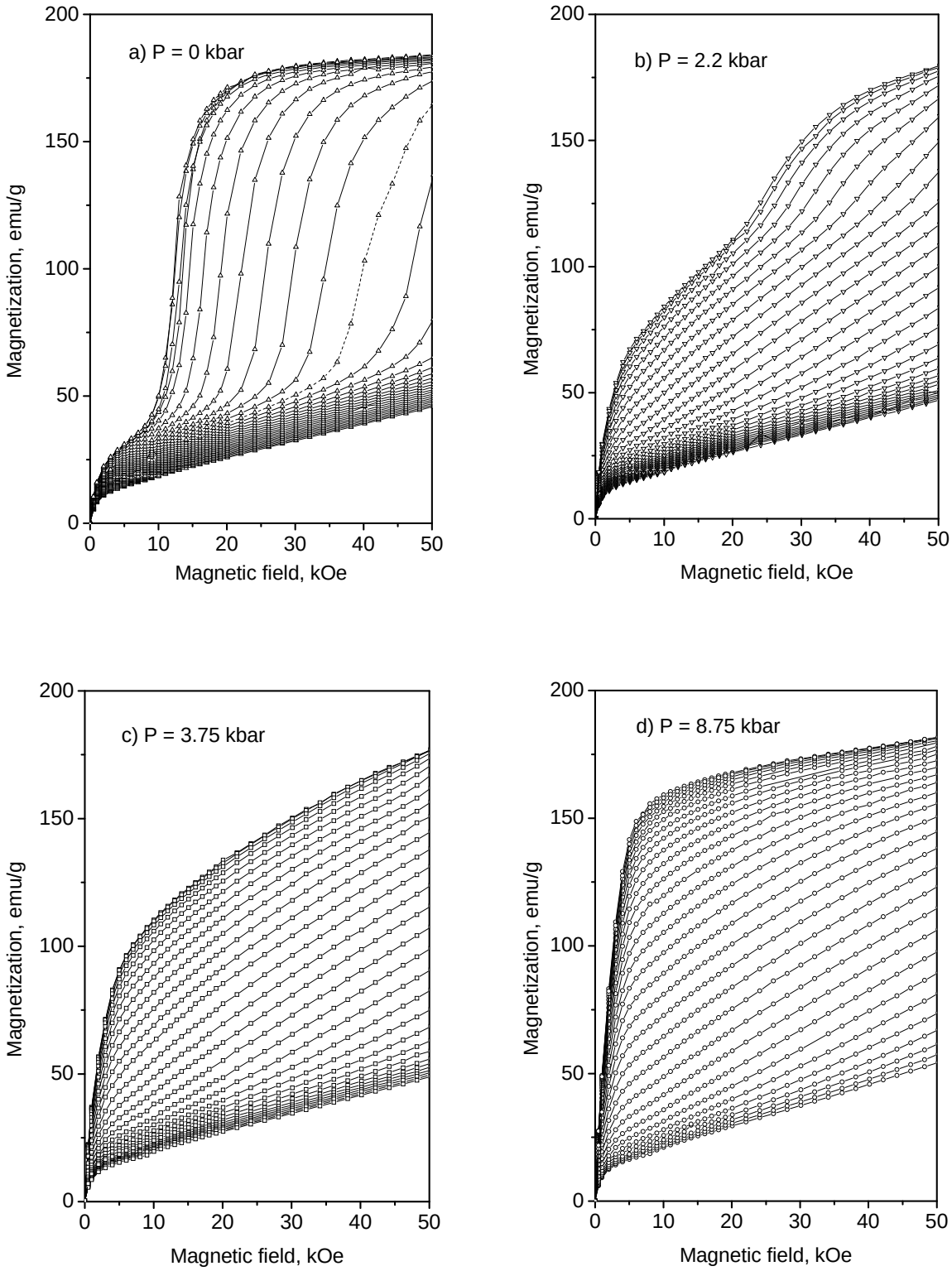

Figure 5.11 Magnetization isotherms of Gd_5Ge_4 under increasing field. Temperature step is 3 K in range 16-100K. Corresponding pressure values are displayed on each plot. The pressure values are taken in vicinity of transition of the Pb pressure sensor to superconducting state, i.e. ~7 K. The high-temperature FM signal corresponds to the minority 5:3 phase.

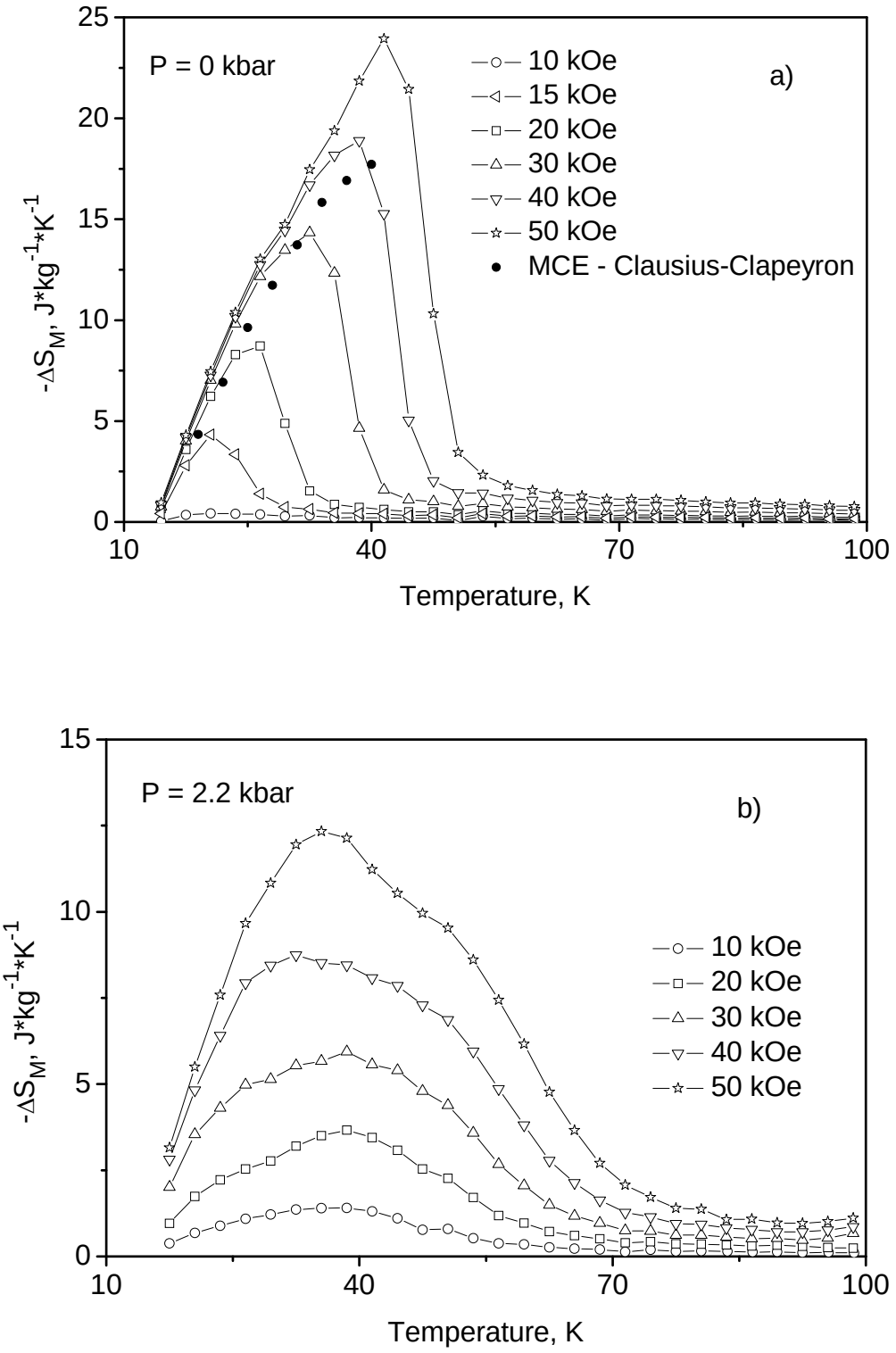

Figure 5.12 a,b. Magnetic entropy change in Gd_5Ge_4 as function of temperature at selected pressures 0 kbar (a) and 2.2 kbar (b) and up to different magnetic fields. The solid circles in a) display the $-\Delta S_M$ obtained using the Clausius-Clapeyron equation (Eq. (2.40)).

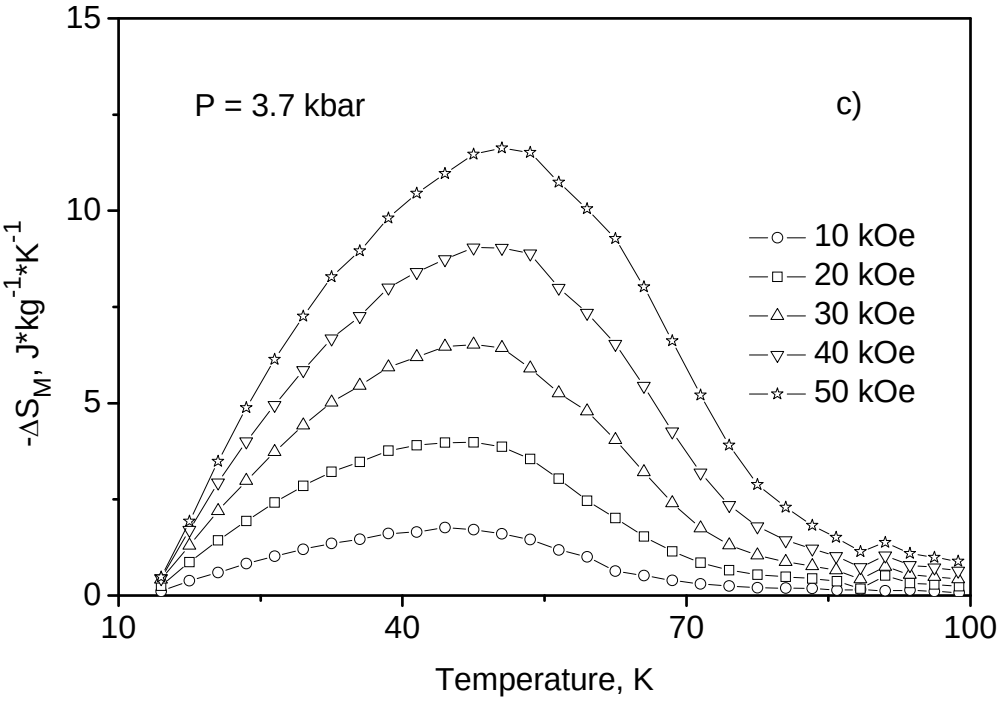

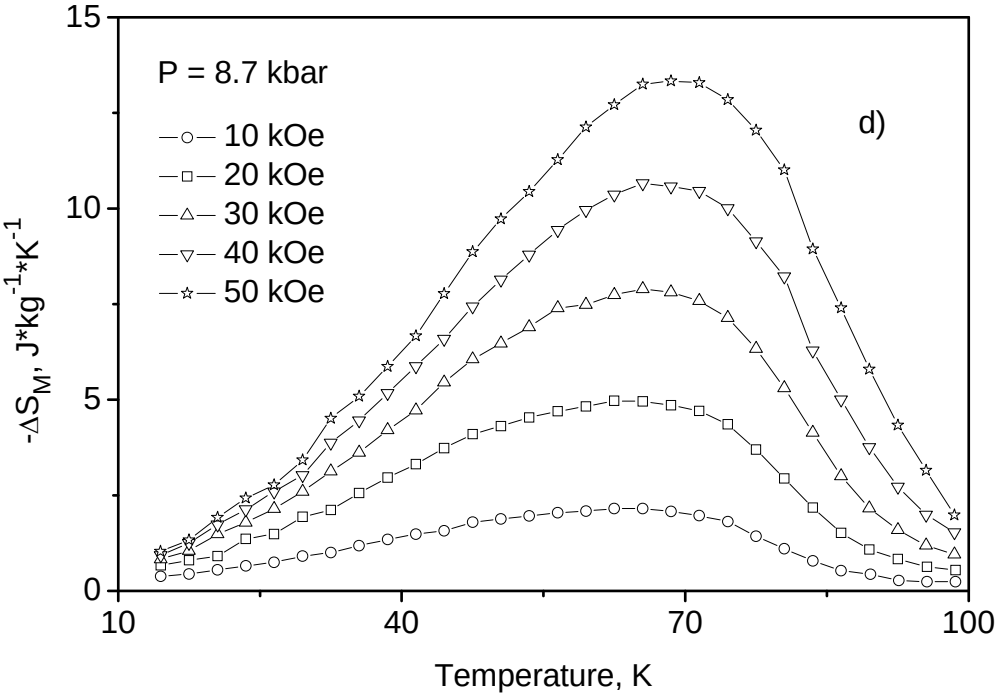

Figure 5.12 c,d. Magnetic entropy change in Gd_5Ge_4 as function of temperature at selected pressures 3.7 kbar (a) and 8.7 kbar (b) and up to different magnetic fields.

Temperature of 40 K is maximum for calculations using Eq.(2.40) because at higher temperatures the magnetization curves do not approach saturation in field up to 50 kOe (dashed line in Fig. 5.11 a). The maximum value of ΔS_M obtained using the Maxwell relation can be larger or smaller than ΔS_{MCC} depending on H_{max}. It reaches value of -24 $J \cdot kg^{-1} \cdot K^{-1}$ at 41.5 K which is maximum in fields up to 50 kOe. At higher pressures, the temperature behavior of ΔS_M fundamentally differs from that obtained at zero pressure. At 2.2 kbar (Fig. 5.12 b) its maximum value drops to -12.3 $J \cdot kg^{-1} \cdot K^{-1}$. The shape of the $-\Delta S_M$ vs. T dependence at 50 kOe allows to conclude that the total MCE consist of two distinguishable contributions: first one is connected with first-order AFM-FM transition and second one is caused by second-order FM-PM transition in the incipient FM phase, accordingly to Fig. 5.9. On further increasing of pressure, the first contribution becomes suppressed (Fig. 5.12 c) and totally disappears at 8.7 kbar (Fig. 5.12 d).

Calculating the $-\Delta S_M$ value in fields below H_C and taking into account dependence in Fig. 5.9 one can estimate the increasing of the maximum MCE value with respect to the growing amount of the pressure-induced *O*(I)-FM phase. Resulting $-\Delta S_{Mmax}$ vs. percentage of the *O*(I)-FM phase is shown in Fig. 5.13.

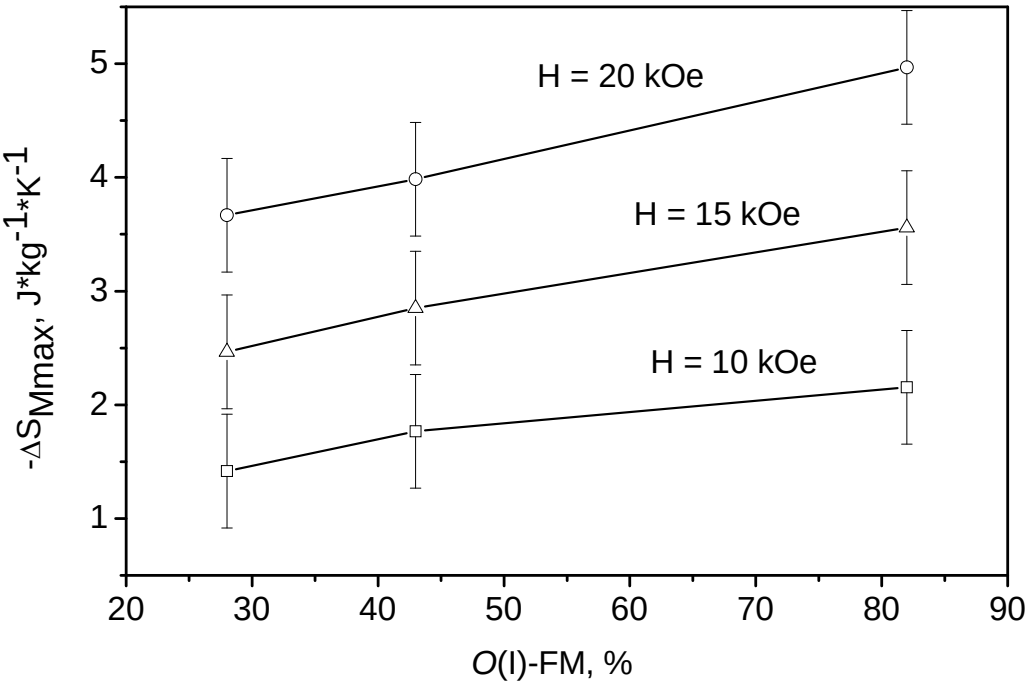

Figure 5.13. Dependence of the maximum MCE at selected magnetic field values below H_C on relative content of the pressure induced *O*(I)-FM phase in Gd_5Ge_4 compound. The $-\Delta S_{Mmax}$ values were taken at selected pressures, temperatures and fields.

5.2 $Gd_5Si_{0.4}Ge_{3.6}$ compound

To investigate the volume dependence of the magnetic properties of Ge-rich $Gd_5(Si_xGe_{1-x})_4$ compounds, we performed magnetic and magnetoelastic measurements on the $Gd_5Si_{0.4}Ge_{3.6}$ (x = 0.1) compound under hydrostatic pressure. Accordingly to the magneto-crystallographic phase diagram (Fig. 4.8), $Gd_5Si_{0.4}Ge_{3.6}$ represents paramagnetic *O*(II) structure at room temperature. On cooling, the compound goes through the magnetic PM – AFM transition at $T_N \sim 130$ K and magnetostructural AFM *O*(II) – FM *O*(I) transition at $T_C \sim 80$ K (Morellon 2000). Comparison with pressure measurements on the Gd_5Ge_4 compound (see previous section) allows to us to obtain the volume dependencies of T_C on the basis of both pressure and Si concentration, (i.e. the effect of "chemical pressure").

5.2.1 Magnetic properties under high pressure

The temperature dependencies of the low-field magnetization (H = 500 Oe) of $Gd_5Si_{0.4}Ge_{3.6}$ were measured in SQUID magnetometer in temperature range 60-160 K under hydrostatic pressures 0, 4.5 and 8.4 kbar (Fig. 5.14). The transition temperatures T_C, T_N were determined as inflection points on the magnetization curves. The critical temperature of the AFM *O*(II) – FM *O*(I) transition has pronounced hysteresis in comparison with second-order character of the PM – AFM transition. The ambient pressure values T_C = 85.9(5) K, T_N = 129.1 K are in excellent agreement with the magneto-crystallographic phase diagram (Fig. 4.8). On increasing pressure, both T_N and T_C shift linearly to higher values at rates dT_N/dP = 0.6(2) K/kbar, dT_C/dP = 2.25 K/kbar (on heating) and dT_C/dP = 2.7(1) K/kbar (on cooling) (Fig. 5.15).

The magnetization isotherms were measured at different pressures in magnetic field range 0 – 50 kOe. Results at pressures 0 and 8.4 kbar are presented in Fig. 5.16. At 5 K, the clear ferromagnetic signal with no hysteresis was obtained. The saturation magnetization M_S = 5.35 μ_B/Gd at. is significantly lower than theoretically predicted 7 μ_B/Gd at. (see Tab. 2.1) which is evidence of texture of the sample and canted FM ground state. The pressure effect on the M_S at T = 5 K is negligible.

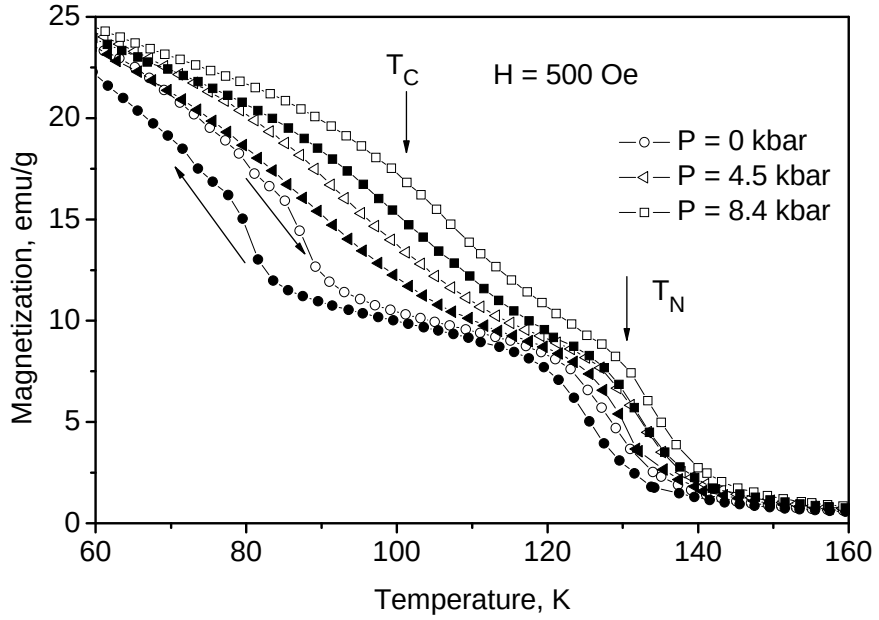

Figure 5.14 The temperature dependence of low-field magnetization of $Gd_5Si_{0.4}Ge_{3.6}$ under several hydrostatic pressures. The open symbols display measurements on heating, the solid ones – on cooling.

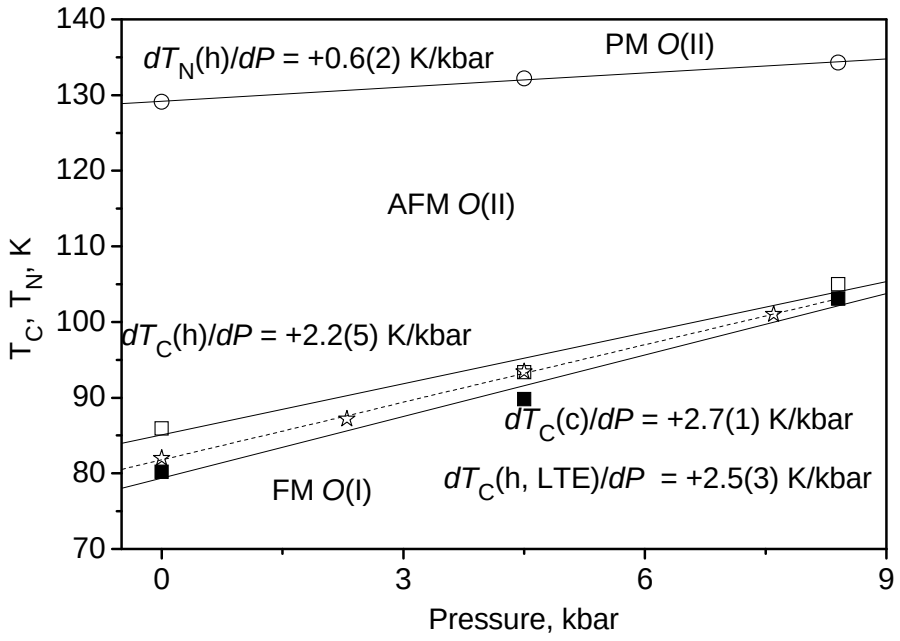

Figure 5.15 The temperature-pressure phase diagram of $Gd_5Si_{0.4}Ge_{3.6}$ as obtained from low-field magnetization measurements (solid lines). The dashed line indicates the AFM *O*(II)-FM *O*(I) phase boundary obtained from LTE measurements. The open symbols stand for heating, the solid ones stand for cooling.

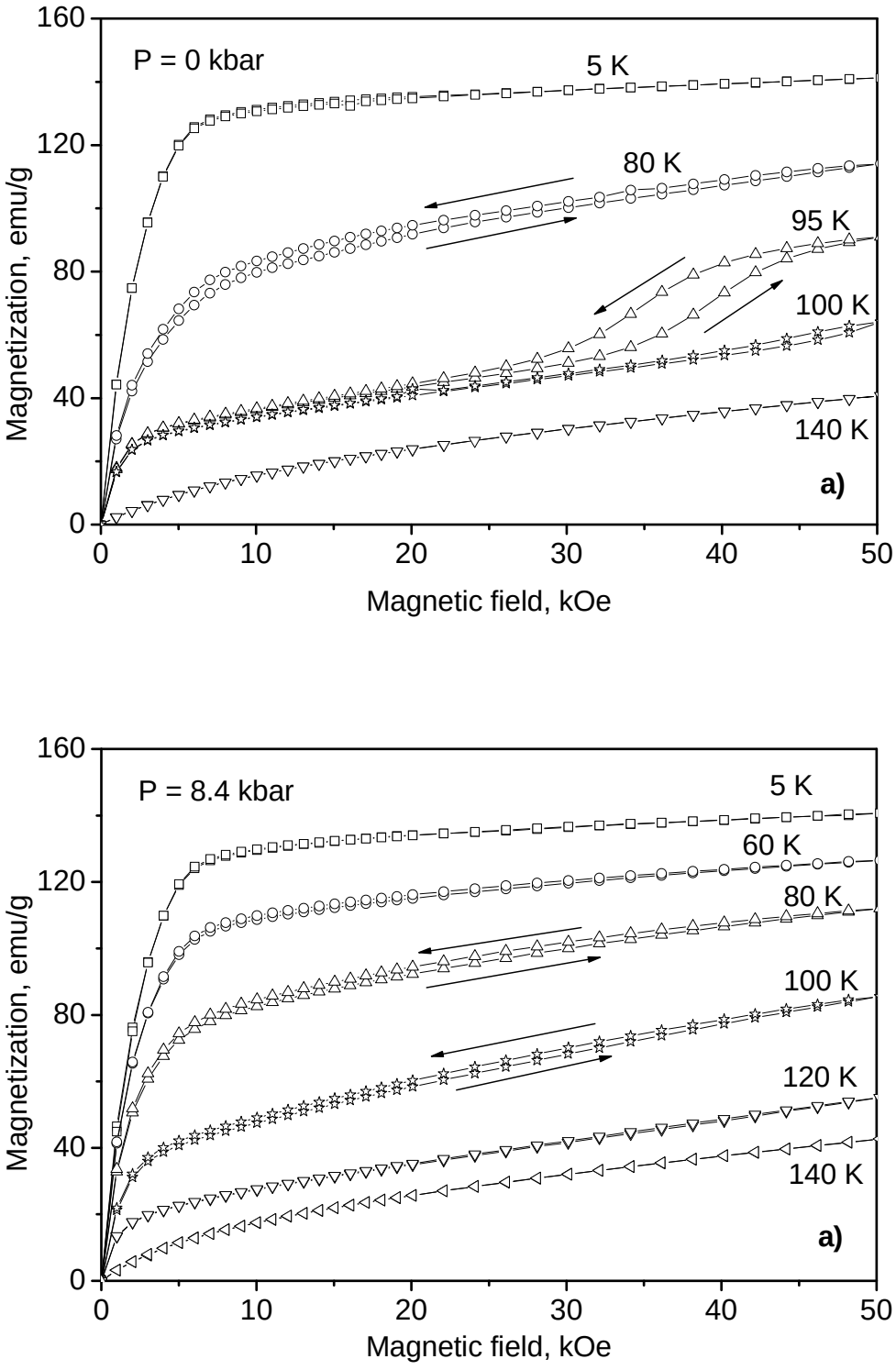

Figure 5.16 Magnetization isotherms of the $Gd_5Si_{0.4}Ge_{3.6}$ compound: a) ambient pressure, b) pressure 8.4 kbar. The arrows show the direction of the magnetic field change when the hysteresis is present.

At higher temperatures, the pressure effect on magnetization becomes much stronger. The 95 K isotherm at ambient pressure shows a clear field-induced AFM-FM transition with pronounced hysteresis at field 40 kOe. The hysteresis almost disappears at 8.4 kbar in agreement with formation of FM state under pressure (see previous section).

5.2.2 Magnetoelastic properties under high pressure

The LTE measurements were carried out in temperature range 12-270 K at pressure values 0, 2.3, 4.5 and 7.6 kbar (Fig. 5.17). The second-order PM-AFM transition within *O*(II) crystallographic structure was found to be undetectable in LTE experiments. On the contrary, the first-order magnetostructural AFM *O*(II)-FM *O*(I) transition is accompanied with significant changes of length. Moreover, the LTE changes its magnitude and sign from $\Delta L/L \sim +0.16\%$ at 0 kbar to $\Delta L/L \sim -0.25\ \%$ at 7.6 kbar. The positive jump at ambient pressure can be explained taking into account high anisotropy of the lattice behavior at AFM-FM transition.

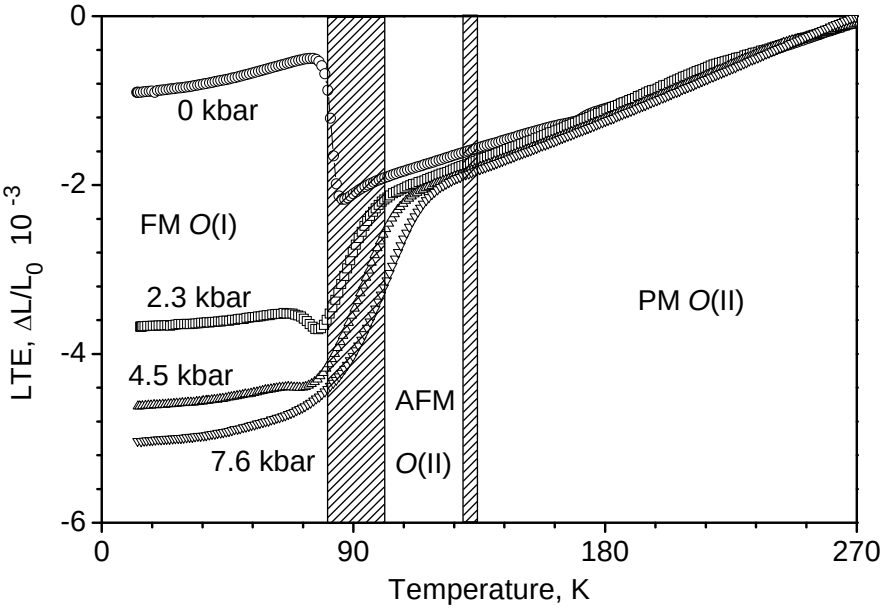

Figure 5.17 LTE of $Gd_5Si_{0.4}Ge_{3.6}$ at different pressures measured on heating. The pressure values are taken near transition temperature. The hatched areas indicate the transition regions.

The X-ray diffraction data (Morellon 2000) show a significant decrease of the *a*-parameter and slight increase of *b* and *c* parameters. Consequently, the increase of in length at ambient pressure indicates strong texture of the polycrystalline sample. The LTE measurements most probably were performed close to the *b*-*c* plane. The transition temperature of the AFM *O*(II) – FM *O*(I) transformation defined as an inflection point on the LTE vs. *T* curves increases with pressure at a rate dT_C/dP = +2.5(3) K/kbar, in good agreement with the low-field magnetization measurements (dashed line in Fig. 5.15).

The compressibility measurements were carried out at room temperature in pressure range 0–10 kbar The relative volume vs. pressure dependence seems to be nonlinear in range of applied pressures, the mean value of compressibility at room temperature is $k = -(1/V)dV/dP = 1.83$ Mbar^{-1}.

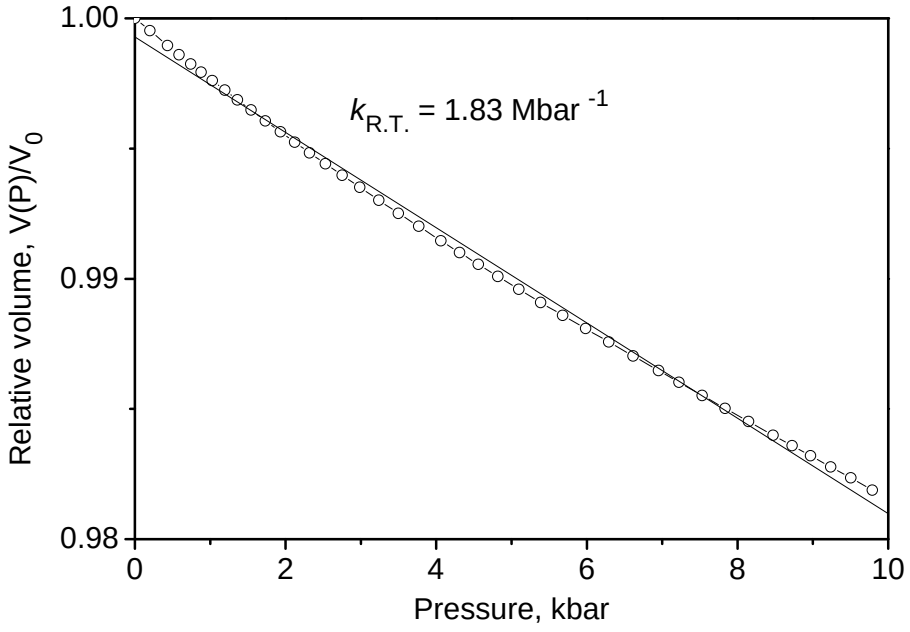

Figure 5.18 Relative volume of $Gd_5Si_{0.4}Ge_{3.6}$ as a function of pressure at room temperature.

Using the compressibility value for $Gd_5Si_{0.4}Ge_{3.6}$ and Gd_5Ge_4 (see previous section) and the magnetostructural information on $Gd_5(Si_xGe_{1-x})_4$ from Ref. (Pecharsky A.O. 2002), one can build the dependence of T_C on the unit cell volume (Fig. 5.19). The strong discrepancy between pressure and concentration dependence is clearly seen. The T_C changes with volume at a rate $dT_C(x)/dV$ = -15.5 K/Å at ambient pressure within the

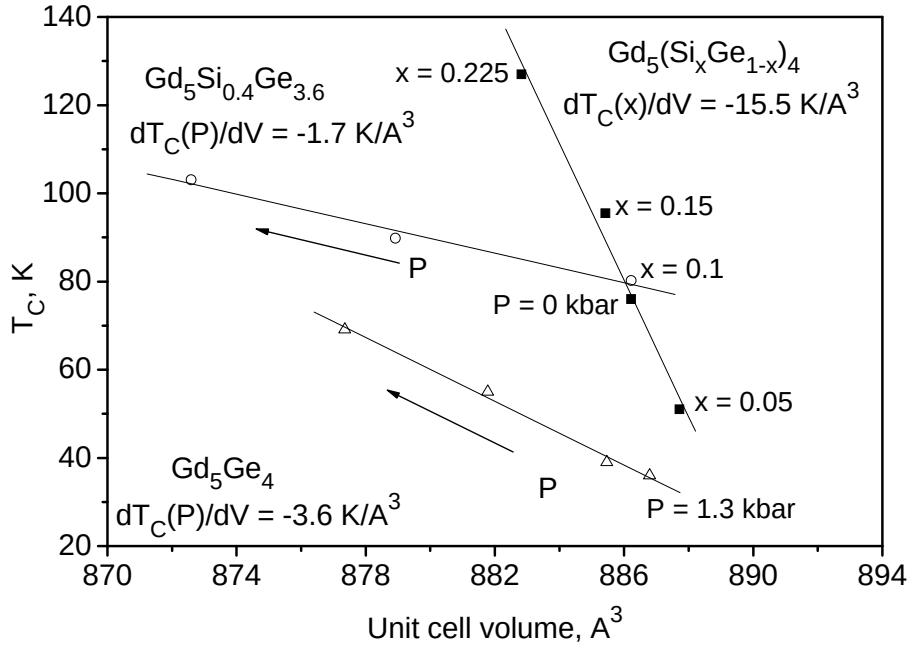

Figure 5.19. Dependence of the transition temperature T_C in $Gd_5(Si_xGe_{1-x})_4$ compounds on the unit cell volume, obtained from volume compressibility (open symbols) and concentration x (full symbols).

Ge-rich series. The pressure dependence of T_C brings much smaller values $dT_C(P)/dV$ = -1.7 K/Å and -3.6 K/Å for $Gd_5Si_{0.4}Ge_{3.6}$ and Gd_5Ge_4 compounds, respectively. The difference in $dT_C(P)/dV$ rates for $Gd_5Si_{0.4}Ge_{3.6}$ and Gd_5Ge_4 compounds seemingly reflects the fact, that in Gd_5Ge_4 the FM ordering sets only under pressure, whereas $Gd_5Si_{0.4}Ge_{3.6}$ has FM ground state at ambient pressure. The result obtained demonstrates that the dependence of the transition temperature upon changing the Si/Ge ratio across the Ge-rich $Gd_5(Si_xGe_{1-x})_4$ series cannot be explained by a pure volume effect.

5.3 $Tb_5Si_2Ge_2$ compound

The $Tb_5Si_2Ge_2$ alloy presents a paramagnetic PM-*M* structure at room temperature, the ground state is FM-O(I). Unlike the $Gd_5(Si_xGe_{1-x})_4$ alloys, where a coupled first-order magnetostructural PM-*M* -> FM-*O*(I) phase transition take place on cooling, the FM state sets in $Tb_5Si_2Ge_2$ at temperature T_C within the monoclinic phase. The structural M->*O*(I) transformation takes place at T_{st} which is lower than T_C (Morellon 2003). Therefore, the structural and magnetic transitions are uncoupled in this system. On cooling, the phase sequence PM-*M* -> FM-*M* -> FM-*O*(I) is observed.

In (Morellon 2004) we reported that the second-order transition in $Gd_5(Si_xGe_{1-x})_4$ is moderately affected by hydrostatic pressure (dT_C/dP = +0.3-0.7 K/kbar). The pressure effect is much stronger (+3 K/kbar) in the case of the first-order magnetostructural transition. Such behavior is the consequence of pressure enhancement of the interlayer interaction when the system is in *O*(I) FM state as also shown in (Magen 2003b). Within this approach, similar dependence of transition temperatures on applied pressure in $Tb_5Si_2Ge_2$ is expected. In this section, the results of investigation of magnetic, magnetoelastic and magnetocaloric properties of $Tb_5Si_2Ge_2$ compound under hydrostatic pressure are presented.

5.3.1 Magnetoelastic properties under high pressure

The linear thermal expansion of the $Tb_5Si_2Ge_2$ was measured under several pressures by mean of methodic described in Sec.3.3.1. The results on heating are displayed in Fig. 5.20. It was observed that the first-order $M \leftrightarrow O$(I) structural transition is connected with a significant jump in LTE and with temperature hysteresis up to 10 K. The transition temperature, T_{st}, is determined as a maximum of derivative of LTE vs. *T* curves (Fig. 5.21). Upon increasing of pressure, the T_{st} shifts linearly from 93 K at zero pressure at a rate dT_{st}/dP = +2.5(9) K/kbar.

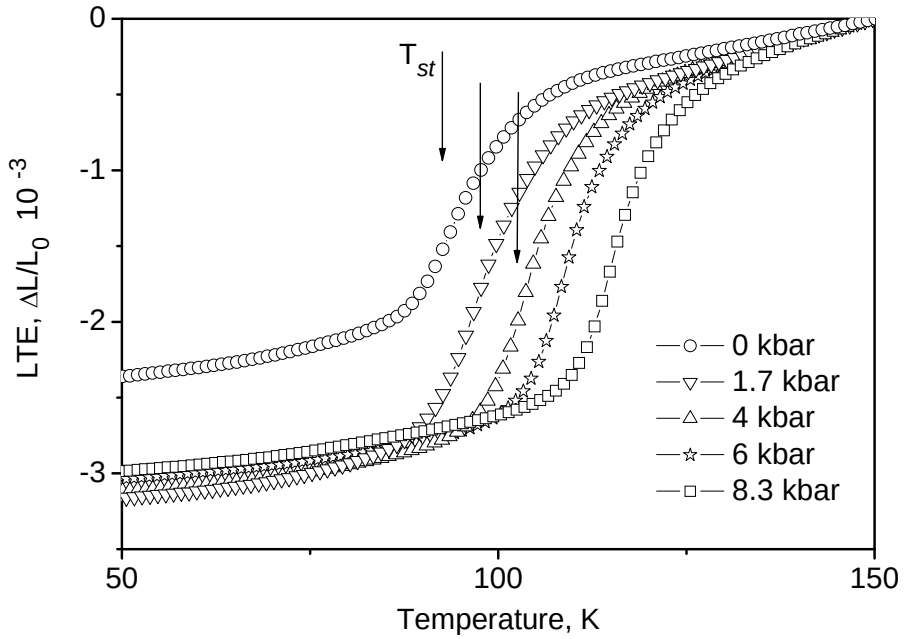

Figure 5.20 LTE of $Tb_5Si_2Ge_2$ under selected values of hydrostatic pressure measured on heating. The pressure values have been determined at T_{st}.

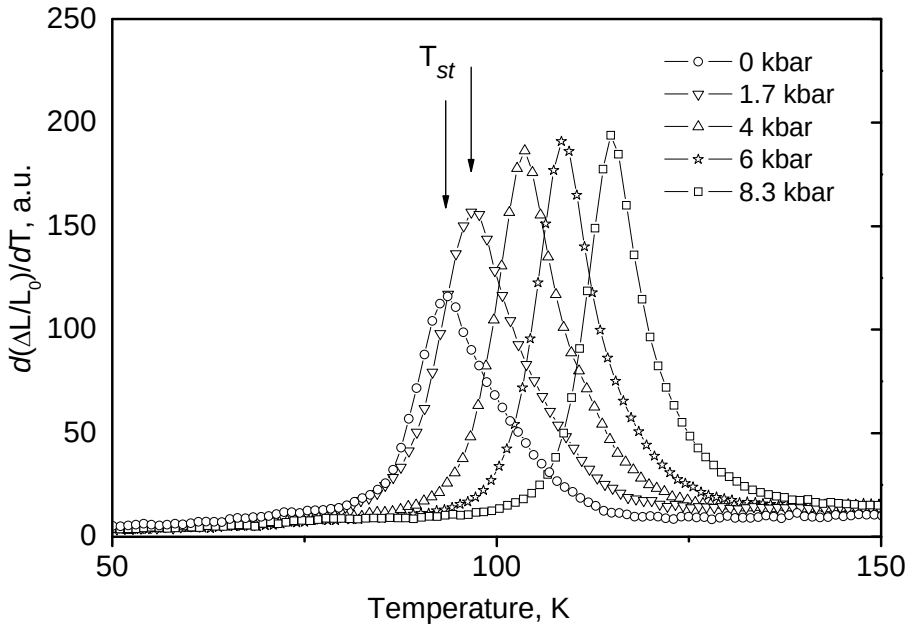

Figure 5.21 An evolution of a structure transition temperature T_{st} defined as a maximum of the thermal expansion coefficient. The pressure values have been determined near T_{st}.

The compressibility measurement was performed at room temperature in pressure range 0 – 10 kbar (Fig. 5.22). The volume of the sample changes unlinearly with pressure. Calculated value of compressibility at low pressures (up to 4 kbar) $k_{low} = -(1/V)dV/dP = 1.89$ Mbar^{-1}.

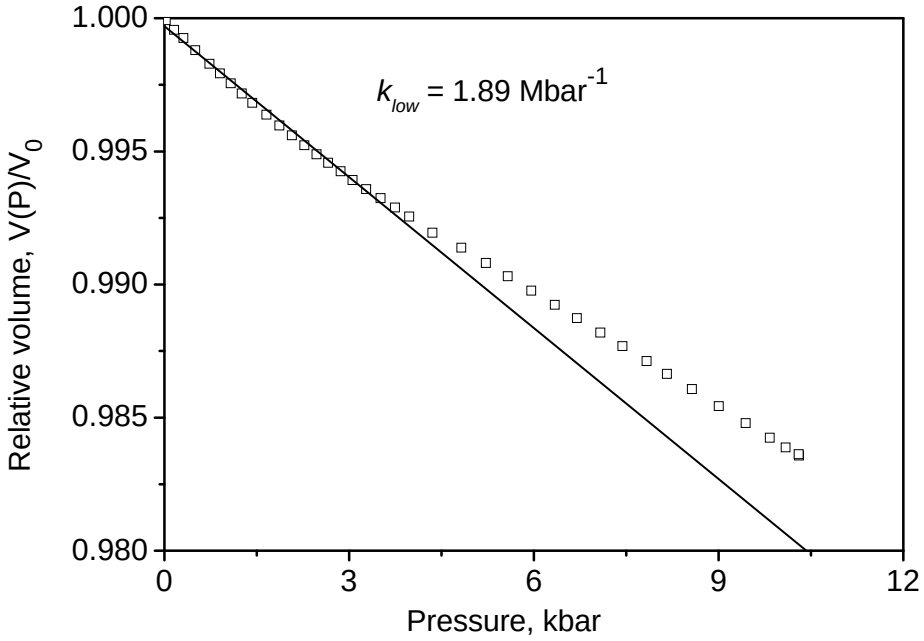

Figure 5.22 The relative volume change upon increasing pressure.

5.3.2 Magnetic properties under high pressure

The temperature dependence of the low-field magnetization (H = 500 Oe) was measured in SQUID magnetometer on heating in temperature range 80 – 150 K (Fig. 5.23). The T_C was determined as inflection point on the temperature dependence of the low-field magnetization, the ambient pressure value is $T_C = 111.5$ K. Small anomalies were observed at $T_{st} < T_C$ that can be corresponded to the structural M-O(I) transition. Both T_C and T_{st} increase linearly with pressure to higher temperatures at a rate $dT_C/dP = +0.63(9)$ K/kbar and $dT_{st}/dP = +2.07(8)$ K/kbar, respectively.

The magnetization isotherms were measured at different pressures in magnetic field range 0 – 50 kOe. Results at several pressures are presented in. Fig. 5.24.

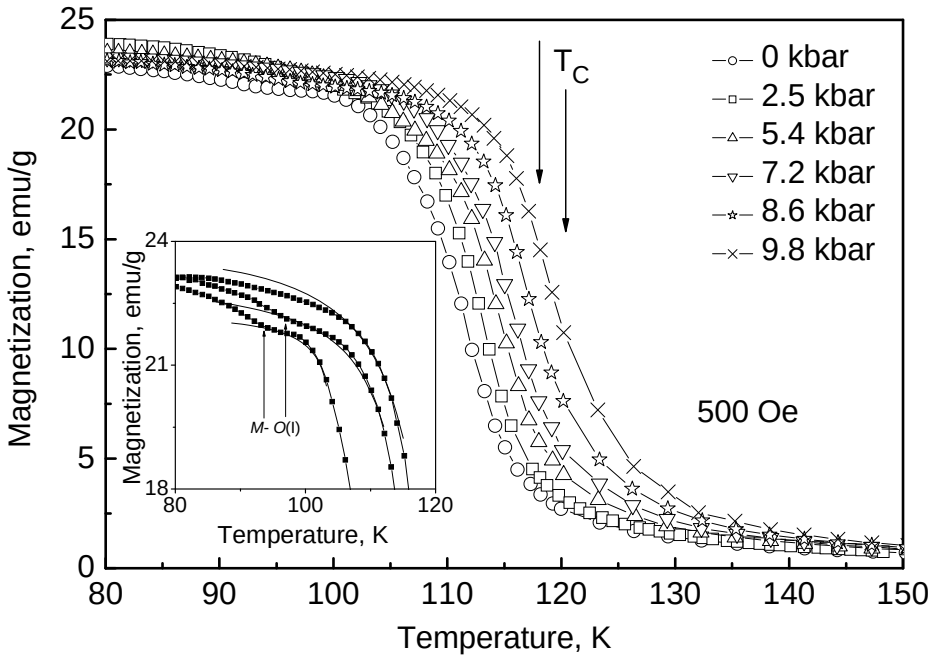

Figure 5.23 Magnetization of $Tb_5Si_2Ge_2$ under different values of hydrostatic pressure measured on heating. The inset shows the structural *M*-*O*(I) transition reflected in magnetization vs. *T* dependence as a small anomaly. The pressure values were determined near transition temperatures.

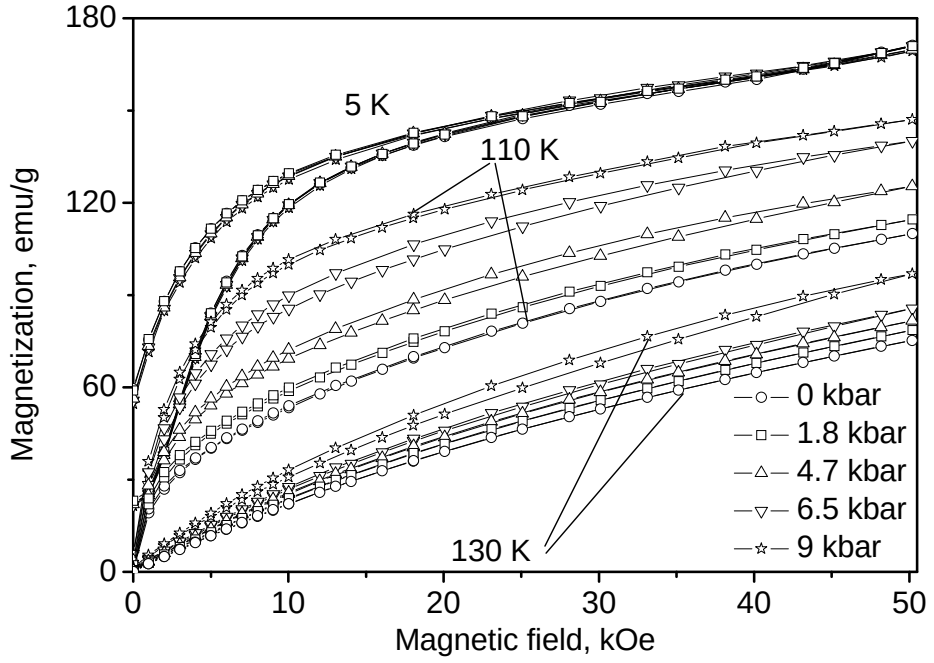

Figure 5.24. Magnetization isotherms on $Tb_5Si_2Ge_2$ at different temperatures and pressures.

The pressure effect on the M_S at T = 5 K is negligible and becomes significantly stronger around T_C. The maximum value of magnetic moment at 50 kOe and 5 K is 6.1 μ_B/Tb at., which is significantly lower than that predicted theoretically 9 μ_B/Tb at. That is evidence of the strong texture of the sample. However, a powder specimen cannot be used due to requirements of high-pressure equipment.

5.3.3 Temperature-pressure phase diagram

Combination of LTE and low-field magnetization measurement has allowed to restore the evolution of the magnetic system with respect to the applied pressure (Fig. 5.25). The values of T_C (open circles) and T_{st} (solid squares) on heating were taken from the magnetization and LTE measurements, respectively. The T_{st} values defined as

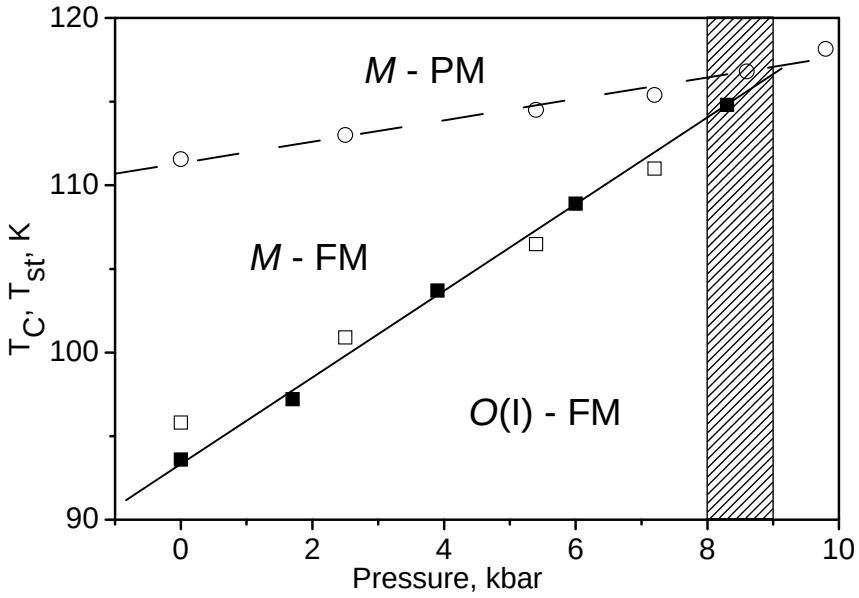

Figure 5.25. Temperature-pressure phase diagram of $Tb_5Si_2Ge_2$ as determined from magnetization (open circles and squares) and LTE (full squares). The dashed and solid lines depict the second-order magnetic PM-FM and first-order structural *M*-*O*(I) transitions, respectively. The hatched area marks the vicinity of tricritical point.

the additional anomaly on M vs. T curves (open squares) related to the structural transformation are in acceptable agreement with the LTE data. It is seen that both

second-order and first order phase boundaries merge at a tricritical point at pressure about 9 kbar. At this pressure, the coupled magnetostructural *M*-PM to *O*(I)-FM transition takes place. Therefore, the intermediate *M*-FM state can exist only up to 9 kbar. Since our equipment allows measurements up to 10 kbar, the further behavior of the magnetostructural transition remains unclear and experiments under higher pressures are strongly desirable.

5.3.4 Magnetocaloric properties

The specific heat data were measured in zero magnetic field in the temperature range 2–200K using the PPMS apparatus (Quantum Design) (Fig. 5.26). The measurement was performed using the relaxation method (see Sec. 3.3.3). A pronounced peak-like anomaly was observed in vicinity of 98.4 K, the maximum value of the specific heat reaches ~289 J*mol^{-1}*K^{-1}. The electronic part of the specific C_{el} heat can be described using the linear Sommerfeld term (see Sec. 2.3.1) with the coefficient γ_{el} = 5.53 mJ*mol^{-1}*K^{-1} (Fig. 5.27). The temperature dependence of the lattice contribution C_{ph} to the specific heat was calculated using the Debye approximation (see Sec. 2.3.1). The best fit of the calculated C_{ph} to the experimental results at both low and high (well below and above the T_C) temperatures was obtained with Debye temperature θ_D = 188 K (Fig. 5.28). The magnetic part C_M of the specific heat was obtained by subtraction of the C_{el} and C_{ph} from the experimental data (Fig. 5.29). The C_M has zero value (within the experimental and calculation accuracy) at low temperatures and reaches maximum value of 100.4 J*mol^{-1}K^{-1} at temperature ~98 K.

The PM-FM transition appears on a high-temperature slope of C_M temperature dependence as anomaly at temperature T_C = 110.7 K in agreement with magnetization measurement. Finally, the temperature dependence of the magnetic entropy S_M (Fig. 5.30) was obtained by numerical integration of Eq. (2.36). The S_M reaches the theoretically predicted value $R\ ln\ (2J+1)$ = 21.32 J*mol^{-1}K^{-1} (see Table 2.1).

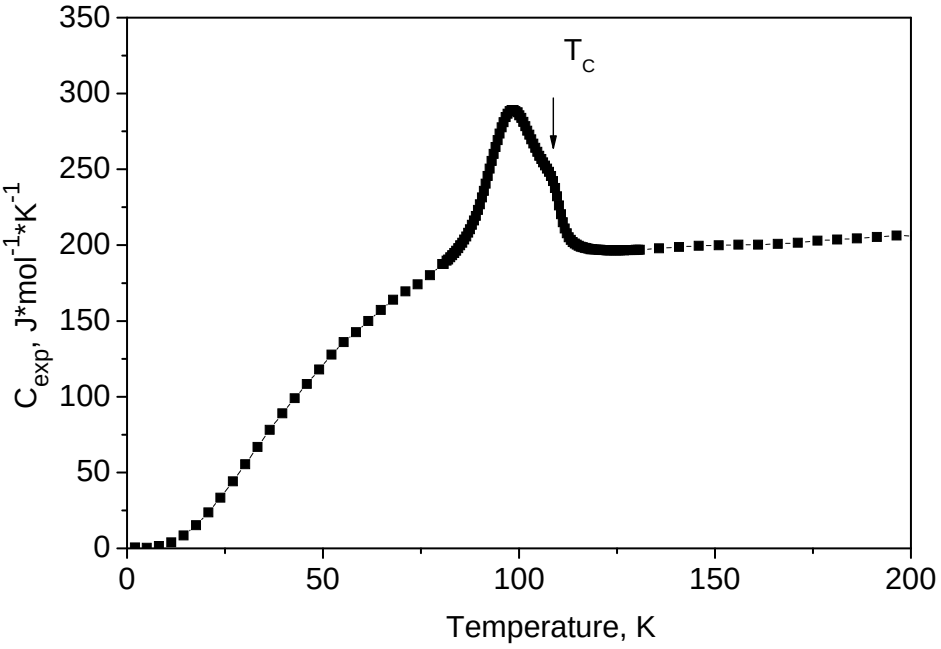

Figure 5.26 Temperature dependence of the specific heat of $Tb_5Si_2Ge_2$ compound measured on heating.

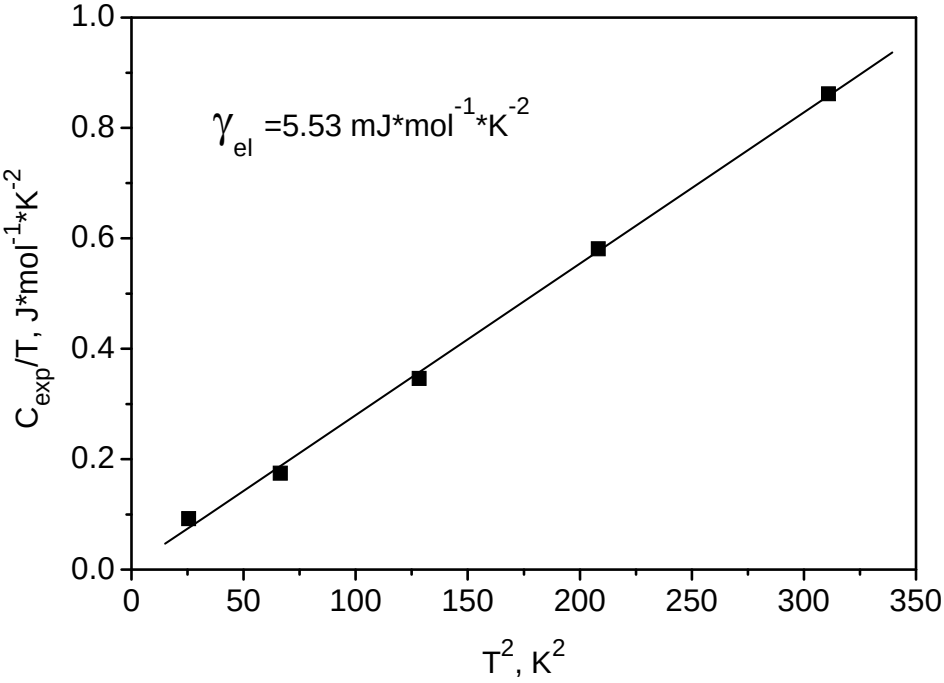

Figure 5.27 Low-temperature part of the C_{exp}/T vs. T^2 plot of the specific heat of $Tb_5Si_2Ge_2$.

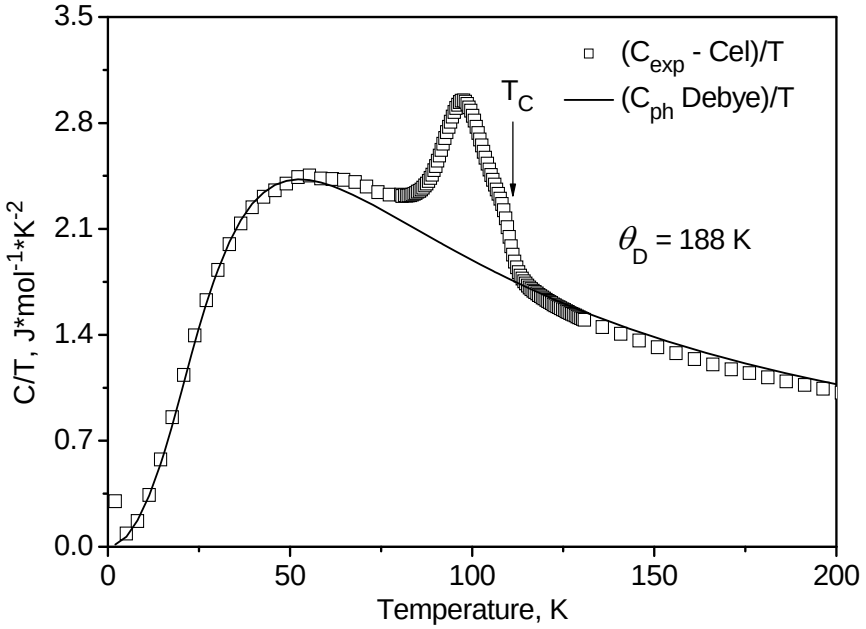

Figure 5.28 The specific heat of $Tb_5Si_2Ge_2$ as C/T vs. T after subtraction of the electron part. The solid line is the Debye fit.

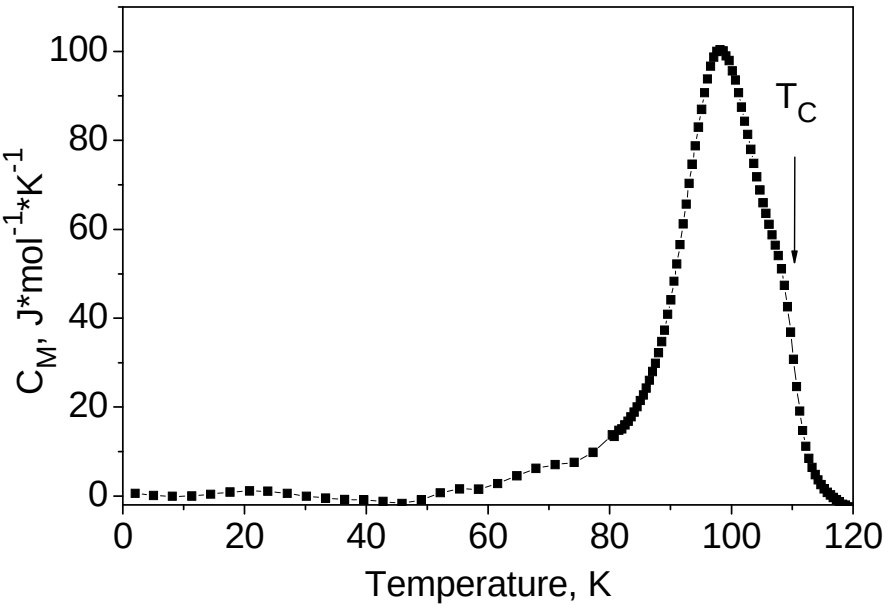

Figure 5.29 Magnetic specific heat of $Tb_5Si_2Ge_2$ obtained by subtraction of the electron and lattice parts from the experimental data.

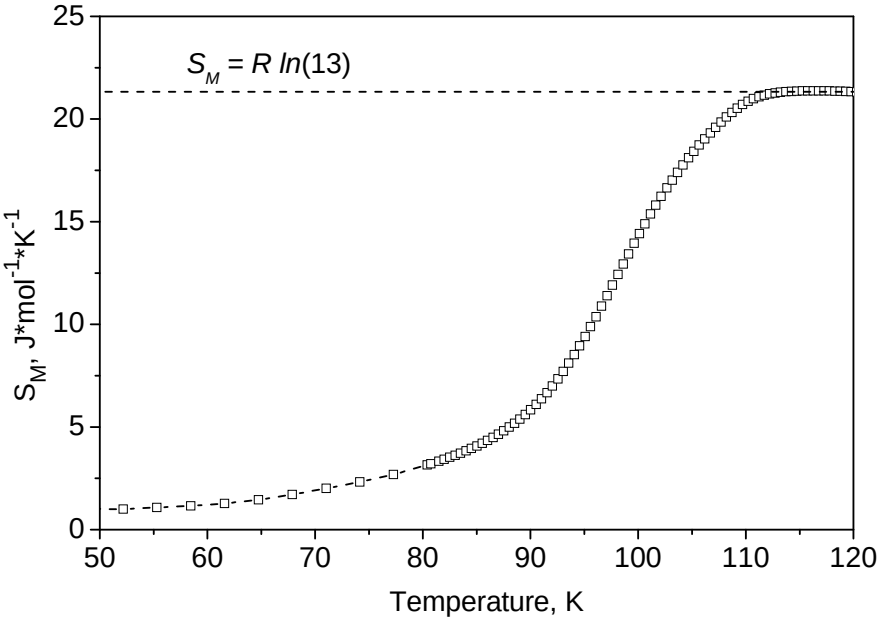

Figure 5.30 Temperature behavior of the magnetic entropy S_M in $Tb_5Si_2Ge_2$. The dashed line indicates theoretically predicted limit of S_M.

In order to investigate the pressure changes of the MCE in $Tb_5Si_2Ge_2$, we measured a large number of the magnetization isotherms at different hydrostatic pressures. The measurements were performed in temperature range 70-150 K with step 2.5 K, in magnetic fields up to 50 kOe (Fig. 5.31). It is clearly seen that magnetization behavior significantly changes its character under pressure. The hysteresis becomes wider that evidences for change from a purely magnetic second-order to the first-order magnetostructural phase transition.

The temperature dependencies of the magnetic entropy change $-\Delta S_M$ were calculated with use of Eq.(2.35) (Fig. 5.32). At ambient pressure, the $|-S_M|$ reaches maximum value 13.4 J*Kg^{-1}K^{-1}. By applying pressure, the wide bell-shaped curve gradually transforms to the peak and shifts to higher temperatures. At pressure 10.2 kbar, the value of the $|-S_M|$ increases to 22.1 J*kg^{-1}K^{-1}.

In (Pecharsky 2003), Pecharsky *et al*. suggested that in systems with first-order magnetostructural transformation (including $R_5(Si_xGe_{1-x})_4$), the giant MCE is the sum of the magnetic entropy-driven process and the difference between entropies of two crystallographic modifications:

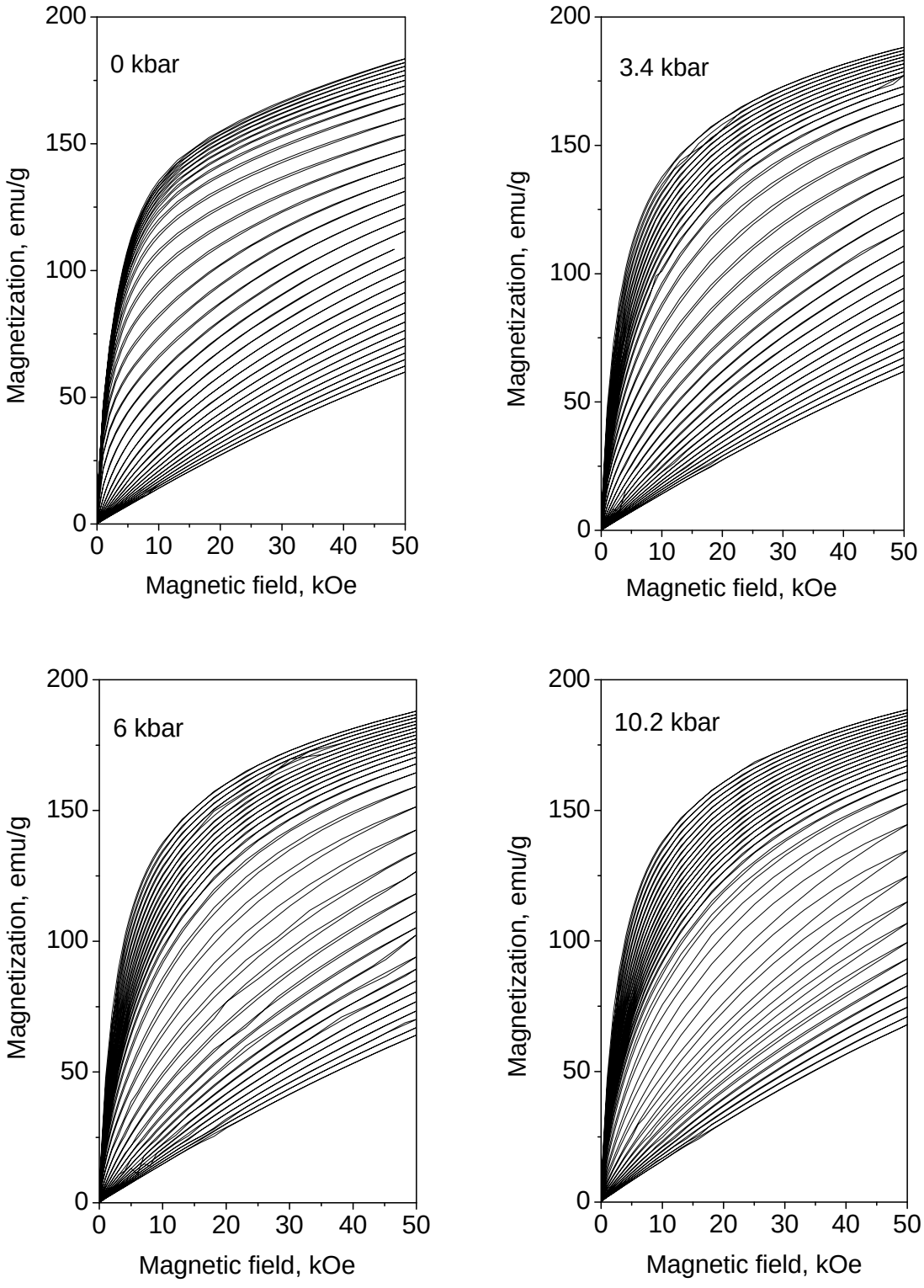

Figure 5.31 Magnetization isotherms on $Tb_5Si_2Ge_2$ at different hydrostatic pressures. The top and bottom curves correspond to 70 K and 150 K, respectively. Temperature step is 2.5 K, values of hydrostatic pressures were taken near T_C.

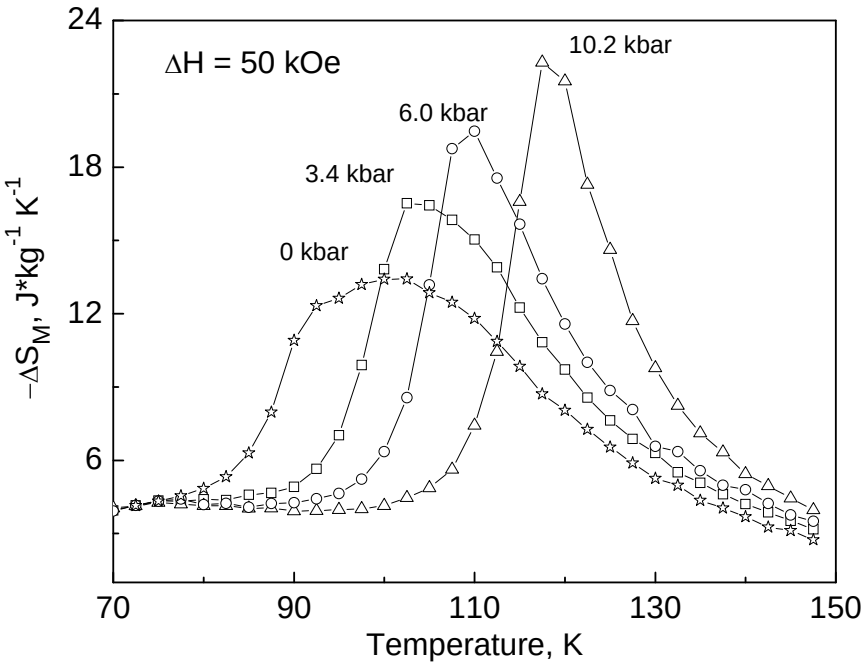

Figure 5.32 Temperature dependencies of magnetic entropy change effect in $Tb_5Si_2Ge_2$ in magnetic field 50 kOe at different pressures.

$$(\Delta S)_T = (\Delta S_M)_T + (\Delta S_{st})_T \qquad (5.1)$$

where ΔS_{st} is hidden parameter in magnetization measurements. Comparing MCE in similar $R_5(Si_xGe_{1-x})_4$ compounds with and without the first-order structural transition, the ΔS_{st} can be estimated. In this point of view, the $T_5Si_2Ge_2$ compound brings a great opportunity to analyze the Eq. 5.1 due to possibility of changing from the second-order magnetic to the first-order magnetostructural transition under hydrostatic pressure. Taking into account the magnetic-pressure phase diagram, one can estimate the value of structural entropy change ΔS_{st} as a difference between MCE at zero pressure and at pressure of transition coupling: $|\Delta S_{st}| \approx |\Delta S_M|(P= 10\ kbar) - |\Delta S_M|(P=0) \approx 9\ J*Kg^{-1}K^{-1}$.

5.4 Monoclinic $Nd_5Si_{1.45}Ge_{2.55}$ and $Pr_5Si_{1.5}Ge_{2.5}$ compounds

Both $Nd_5Si_{1.45}Ge_{2.55}$ and $Pr_5Si_{1.5}Ge_{2.5}$ compounds have a monoclinic $Gd_5Si_2Ge_2$-type crystallographic structure with space group $P112_1/a$ at room temperature. The studies at ambient pressure by means of neutron powder diffraction techniques and magnetization measurements (Magen 2004) showed that on cooling, they go through the second-order magnetic phase transition at ~56 K ($Nd_5Si_{1.45}Ge_{2.55}$) and ~32 K ($Pr_5Si_{1.5}Ge_{2.5}$) from a high-temperature paramagnetic state to a low-temperature complex canted ferromagnetic structure. The monoclinic crystal structure does not change upon cooling down to 4 K showing possibility of full decoupling of magnetic and structural transitions in $R_5(Si_xGe_{1-x})_4$. The absence of structural transition gives an unique opportunity of study of the volume effects on a pure magnetic transition.

5.4.1 Magnetic properties under high pressure

The low-field magnetization of $Nd_5Si_{1.45}Ge_{2.55}$ measured during the temperature scan at pressures 0, 6.7 and 8.8 kbar is presented in Fig. 5.33. The measurements were performed during warming in magnetic field 500 Oe after cooling down from room temperature without an applied field (ZFC) or under an applied field (FC). The difference between the ZFC and FC is known as a spin-glasses-like behavior. The T_C is defined as maximum on the dM_t/dT vs. T curves on FC measurements. At ambient pressure T_C = 58.1 K and increases with pressure at rate dT_C/dP=+0.38 K/kbar. The difference of T_C detected between heating and cooling (not presented here) measurements show no observable hysteresis that indicates the second order phase transition even under the pressure.

The magnetization of $Pr_5Si_{1.5}Ge_{2.5}$ was measured in the same way at pressures 0, 3.8, 6.8 and 9.5 kbar. Fig. 5.34 shows a qualitatively similar behavior as in previous case. The compound orders ferromagnetically at T_C = 36.2(8) K, the T_C increases with pressure more slowly, dT_C/dP=+0.21 K/kbar. As in case of $Nd_5Si_{1.45}Ge_{2.55}$ compound,

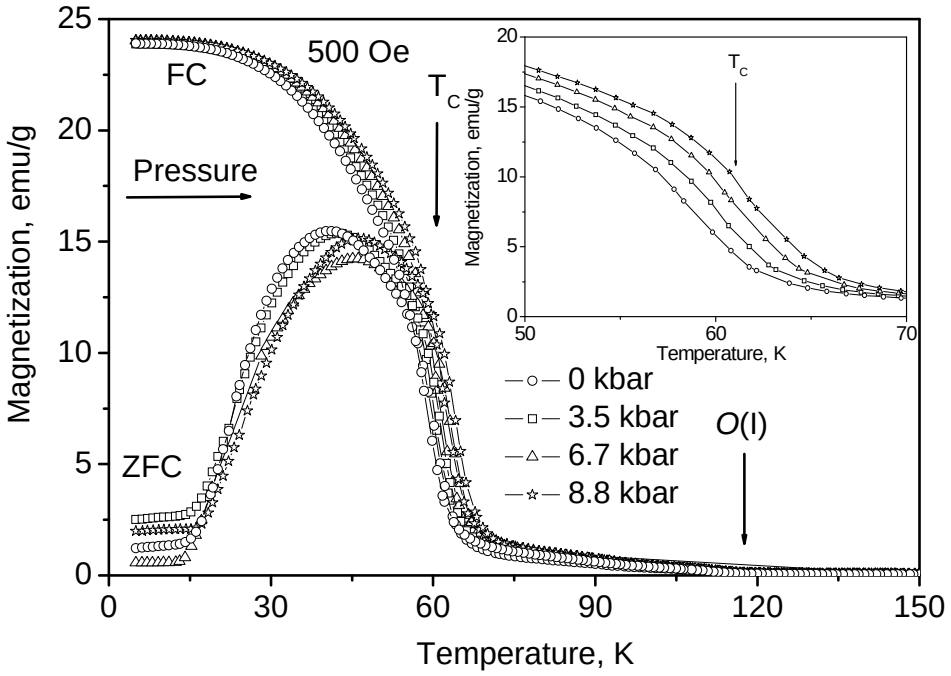

Figure 5.33 Temperature dependence of zero-field cooling and field cooling dc-magnetization of $Nd_5Si_{1.45}Ge_{2.55}$ in magnetic field of 500 Oe and at different pressures

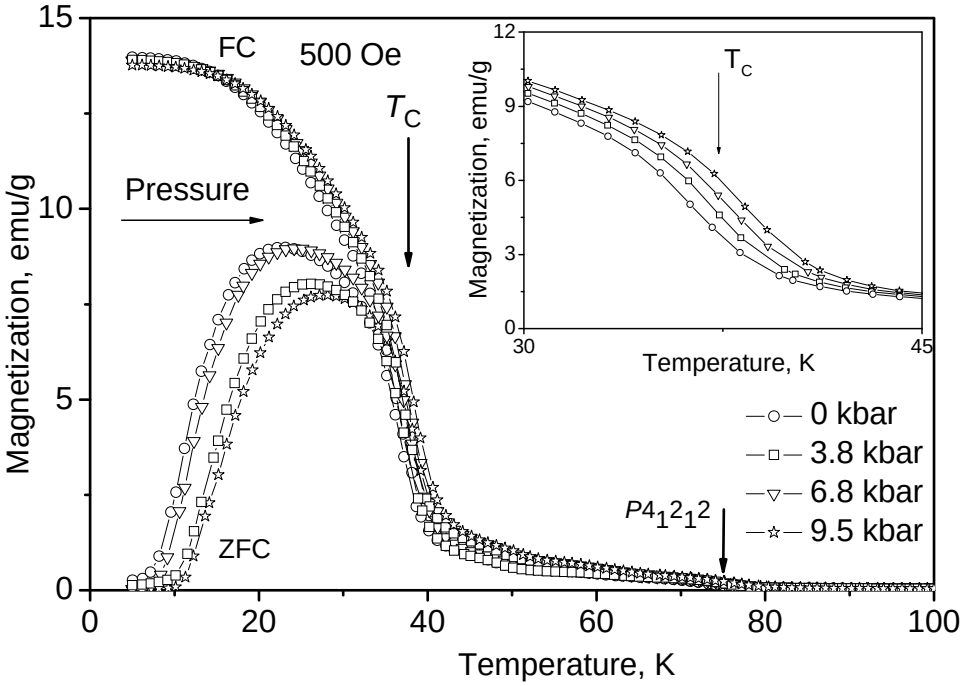

Figure 5.34 Temperature dependence of zero-field cooling and field cooling dc-magnetization of $Pr_5Si_{1.5}Ge_{2.5}$ in magnetic field of 500 Oe and at different pressures.

no temperature hysteresis was found. Small anomalies were observed on both compounds at T_{Nd} = 115 K and T_{Pr} = 76 K which corresponded to a small amount of an impurity phase with a higher T_C. The presence of the secondary phase was confirmed before in a monoclinic $Nd_5Si_2Ge_2$ alloy and suggested to be a ferromagnetic Gd_5Si_4-type *O*(I) secondary phase (Gschneidner 2000, Yang 2003). A similar effect was observed by Yang *et al*. for $Pr_5Si_2Ge_2$, the anomaly was attributed to a minor amount of tetragonal $P4_12_12$structure (Yang 2002a). The pressure dependence of the T_C of both compounds is presented in Fig. 5.35

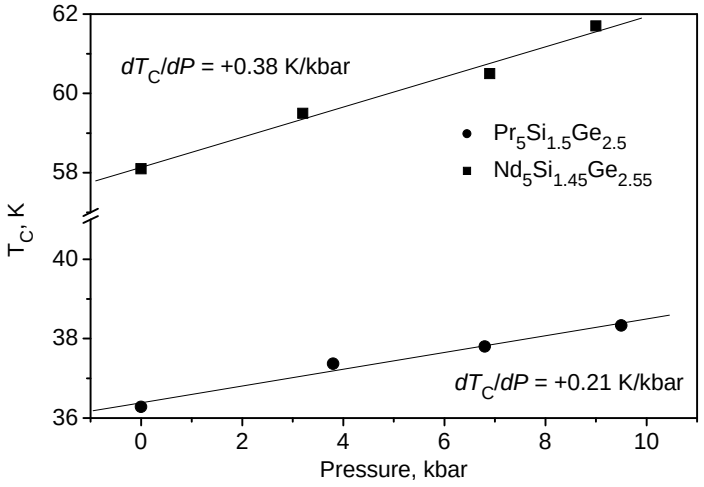

Figure 5.35 Pressure dependence of the T_C in $Pr_5Si_{1.5}Ge_{2.5}$ (circles) and $Nd_5Si_{1.45}Ge_{2.55}$ (squares). The lines are the guides for the eye.

Magnetization isotherms were measured in magnetic fields up to 50 kOe at different temperatures and the same pressures as in the case of low field magnetization measurements (0, 3.5, 6.7 and 8.8 kbar for $Nd_5Si_{1.45}Ge_{2.55}$ and 0, 3.8, 6.8 and 9.5 kbar for $Pr_5Si_{1.5}Ge_{2.5}$). The results are presented in Fig. 5.36 and Fig. 5.37, respectively. At 5 K they are similar in shape and reaching the saturation at magnetic fields about 10 kOe. The saturation magnetizations are significantly smaller (M_{SNd} =2.25 μ_B/Nd at. and M_{SPr} =2.14 μ_B/Pr at.) than the theoretical values of 3.27 and 3.2 μ_B/at for Nd and Pr ions, respectively (see Sec. 2.1). This is a consequence of texture of the sample in addition to a canted FM structure (Magen 2004) that can not be aligned in a range of applied fields.

The other significant effect in the studied compounds is the high value of the remanent magnetization. The calculated values of Mr/M_S are 0.84 for Nd-based and 0.8 for Pr-based compound that contrasts with the small or even absent remanence in other $R_5(Si_xGe_{1-x})_4$ compounds.

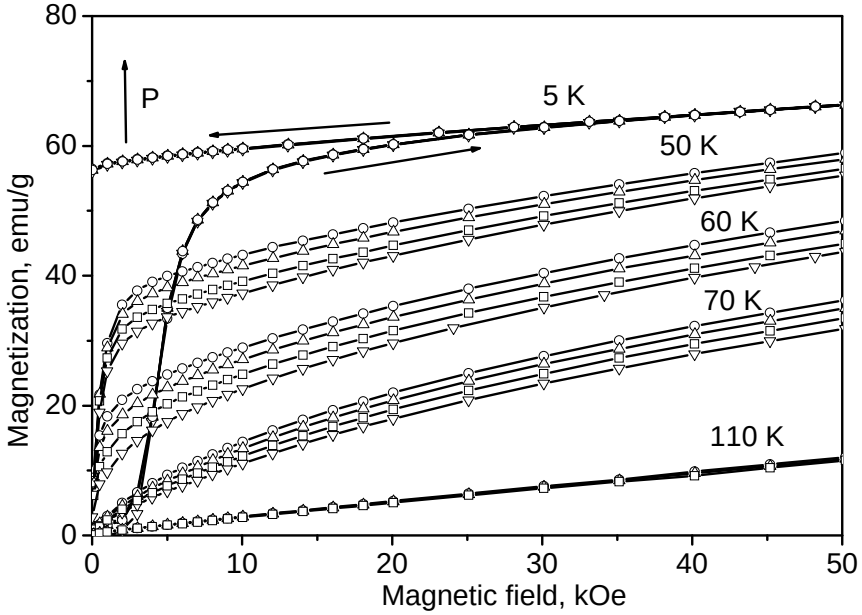

5.6

Figure 5.36 Magnetization isotherms measured on $Nd_5Si_{1.45}Ge_{2.55}$ at different temperatures and pressures 0, 3.5, 6.7 and 8.8 kbar

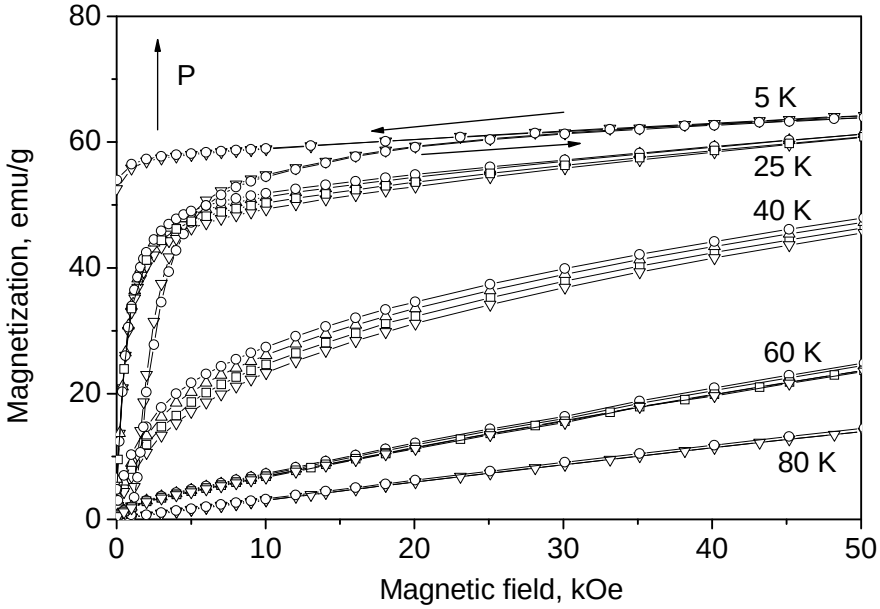

Figure 5.37 Magnetization isotherms measured on $Pr_5Si_{1.5}Ge_{2.5}$ at different temperatures and pressures 0, 3.8, 6.8 and 9.5 kbar

The pressure effect on both compounds is negligible at T=5 K. It indicates that most probably both the Nd and Pr magnetic moments and the canted FM structure are not affected by the high pressure. Pressure induced increase of magnetization at temperatures close to Curie temperature is a consequence of increase of Curie temperature with increasing pressure - see (2.43).

5.4.2 Magnetoelastic properties under high pressure

In order to evaluate the dependence of the magnetic and magnetocaloric properties on the unit cell volume, the compressibility measurements were carried out at room temperature in pressure range 0-12 kbar. At 12 kbar, the volume suppressions make 2.1% and 2.2% for Nd and Pr based compounds, respectively (Fig. 5.38). Calculated compressibilities of both compounds have similar values 1.7 and 1.8 $Mbar^{-1}$, respectively.

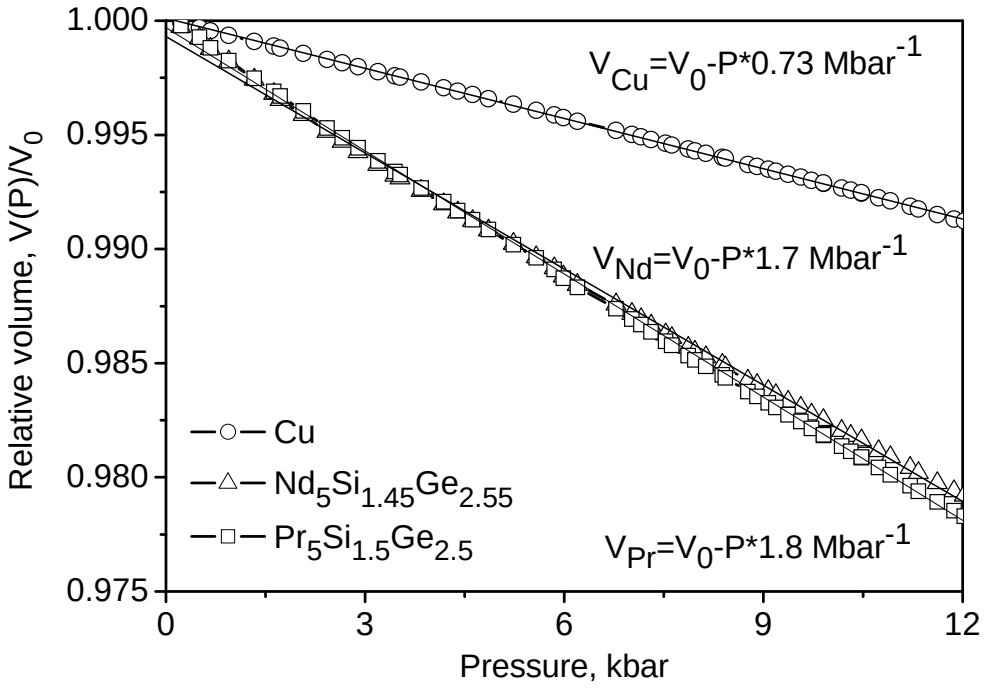

Figure 5.38 Volume changes of $Nd_5Si_{1.45}Ge_{2.55}$ and $Pr_5Si_{1.5}Ge_{2.5}$ at high hydrostatic pressure up to 12 kbar measured together with pure Cu.

At low temperatures, when the phase transition occurs, compressibility of studied material can differ from its room-temperature value (for example, see Fig. 5.3). In order to estimate the difference and to study temperature behavior of the lattice, the linear thermal expansion (LTE) measurements at different pressures were performed. Results of LTE measurements of $Pr_5Si_{1.5}Ge_{2.5}$ and $Nd_5Si_{1.45}Ge_{2.55}$ compounds in temperature range 10-150 K with respect to 150 K are presented in Fig. 5.39 and Fig. 5.40, respectively. The left axis represents the thermal expansion in form {L(T)-L(T=150K)}/L(T=150K) and the right one represents the thermal expansion coefficient α_{TE} in form $d[\{L(T)-L_0\}/L_0]/dT$. In the vicinity of the phase transition to the FM state

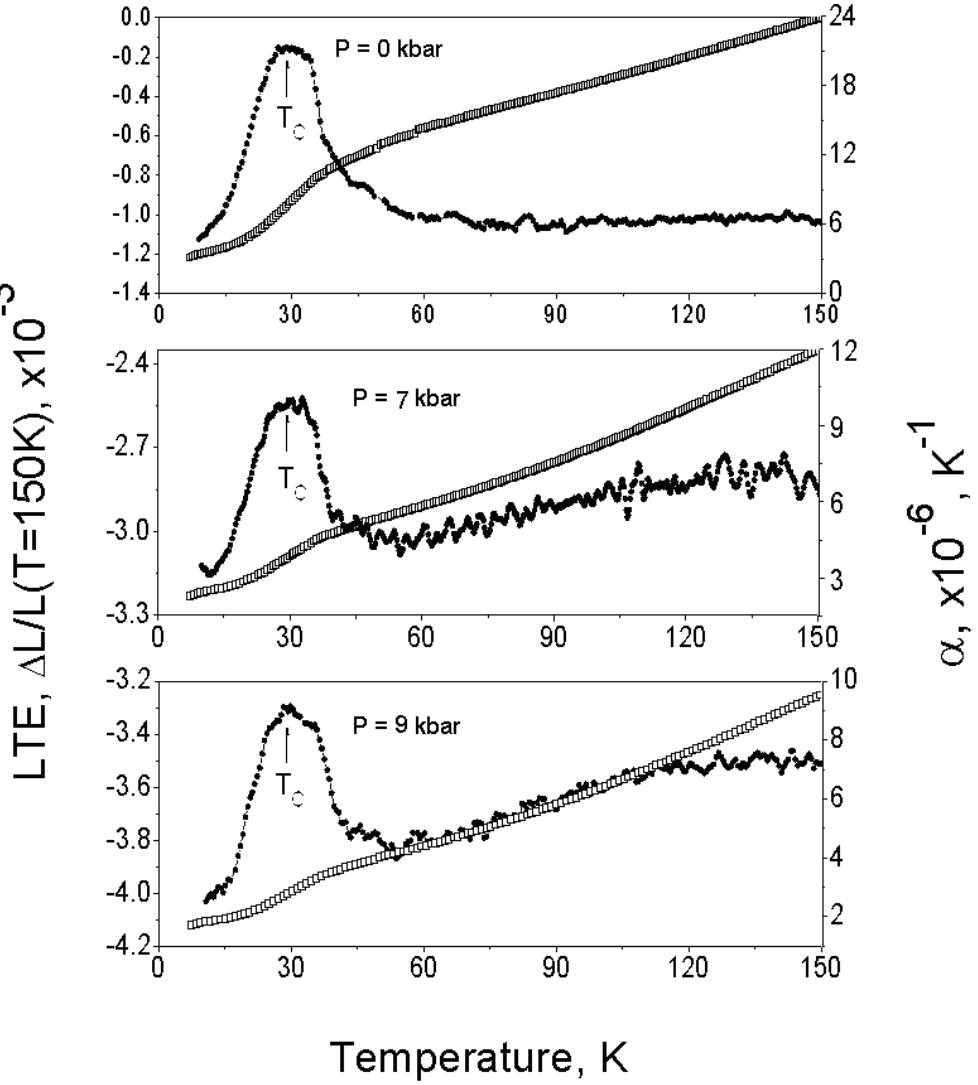

Figure 5.39 Linear thermal expansion (open squares) with respect to 150 K and the LTE coefficient (circles) of $Pr_5Si_{1.5}Ge_{2.5}$

the pronounced but relatively small anomaly was observed. The linear compressibilities at different temperatures were extracted from the thermal expansion data in order to compare their values at temperatures below and above the phase transition. As since no significant difference was observed, the room-temperature compressibility value can be extended down to the temperature of the phase transition.

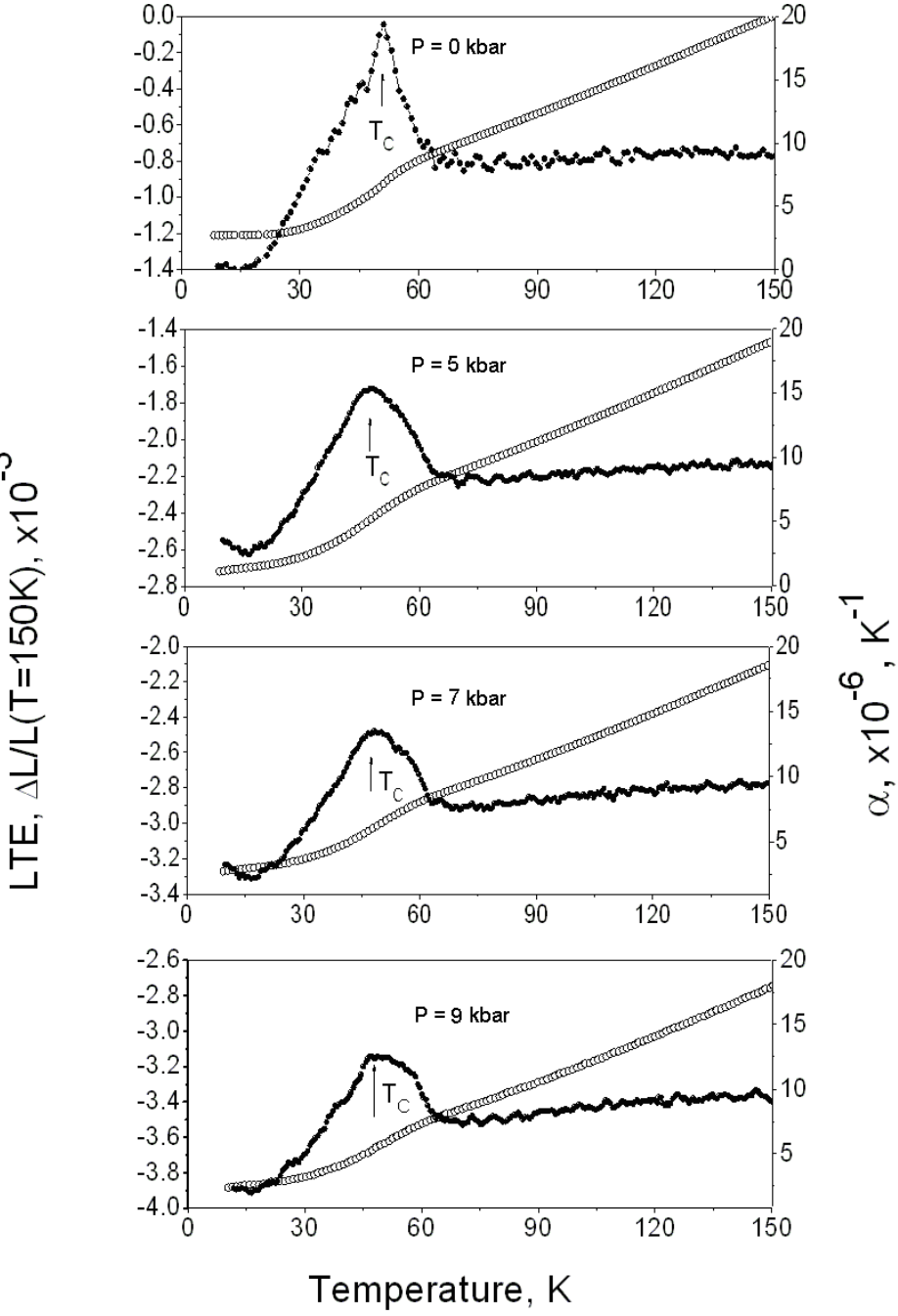

Figure 5.40 Linear thermal expansion (open circles) with respect to 150 K and the LTE coefficient (circles) of $Nd_5Si_{1.45}Ge_{2.55}$

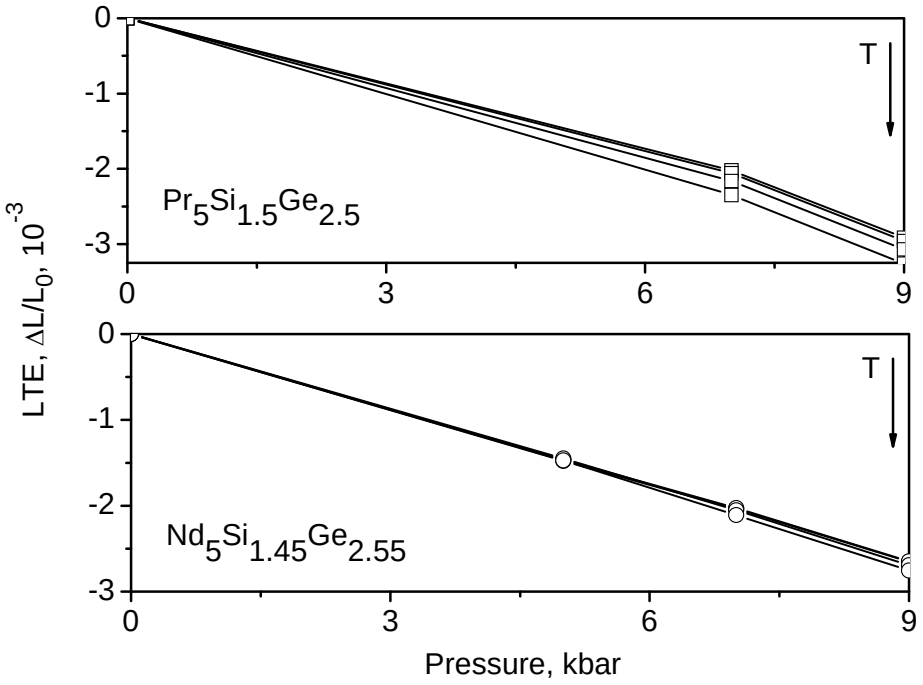

Figure 5.41 Linear thermal expansion of $Nd_5Si_{1.45}Ge_{2.55}$ and $Pr_5Si_{1.5}Ge_{2.5}$ at different temperatures obtained from the LTE measurements

5.4.3 Magnetocaloric properties

The isobaric molar specific heat of $Nd_5Si_{1.45}Ge_{2.55}$ and $Pr_5Si_{1.5}Ge_{2.5}$ was measured in PPMS by relaxation method at ambient pressure, results are presented in Fig. 5.42 and Fig. 5.44 for Pr and Nd-based compounds, respectively. The anomalies related to magnetic phase transition were observed in vicinity of T_C. From the low-temperature parts of C/T vs. T^2 plots we have found values of the Sommerfeld coefficient γ_{el} of the electronic specific heat $C_{el} = \gamma_{el}T$: 91.1 mJ*mol^{-1}K^{-2} for $Pr_5Si_{1.5}Ge_{2.5}$ and 49.7 mJ*mol^{-1}K^{-2} for $Nd_5Si_{1.45}Ge_{2.55}$ (Fig. 5.43 and Fig. 5.45, respectively). Further analysis of specific heat of the studied compounds was performed in order to determine the magnetic contribution. Taking into account that the specific heat of solids can be presented as a sum of electron, lattice and magnetic parts, the magnetic specific heat can be obtained by subtraction of electron and lattice contributions from the experimental data (Fig. 46,47).

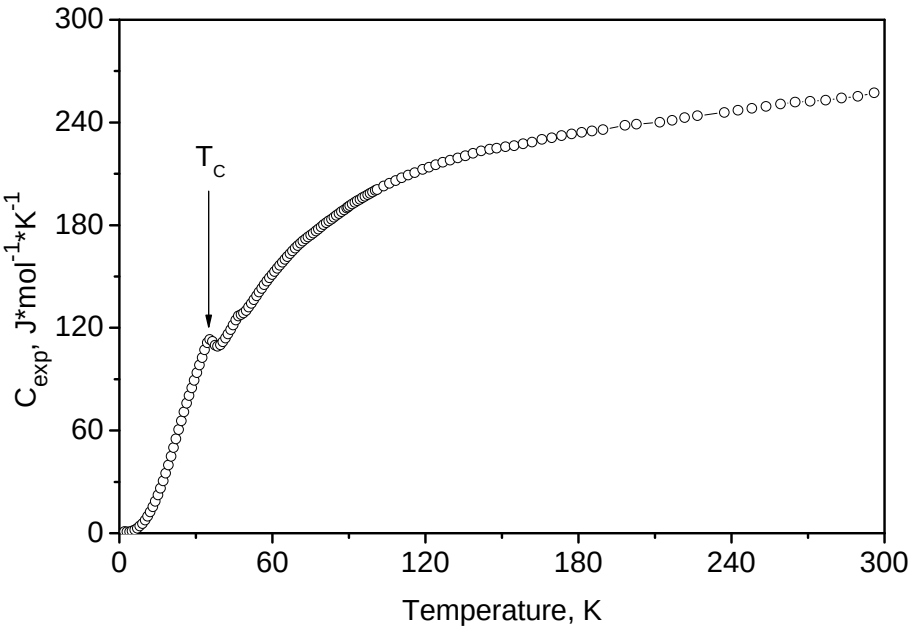

Figure 5.42 Temperature dependence of the specific heat of $Pr_5Si_{1.5}Ge_{2.5}$.

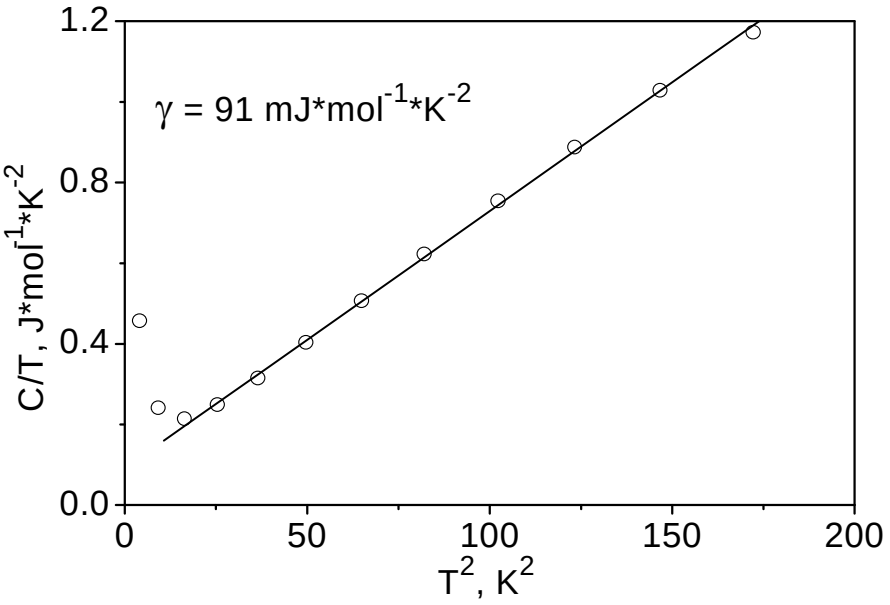

Figure 5.43 Low-temperature part of the specific heat of $Pr_5Si_{1.5}Ge_{2.5}$ as C/T vs. T^2 from which the γ_{el} value was obtained.

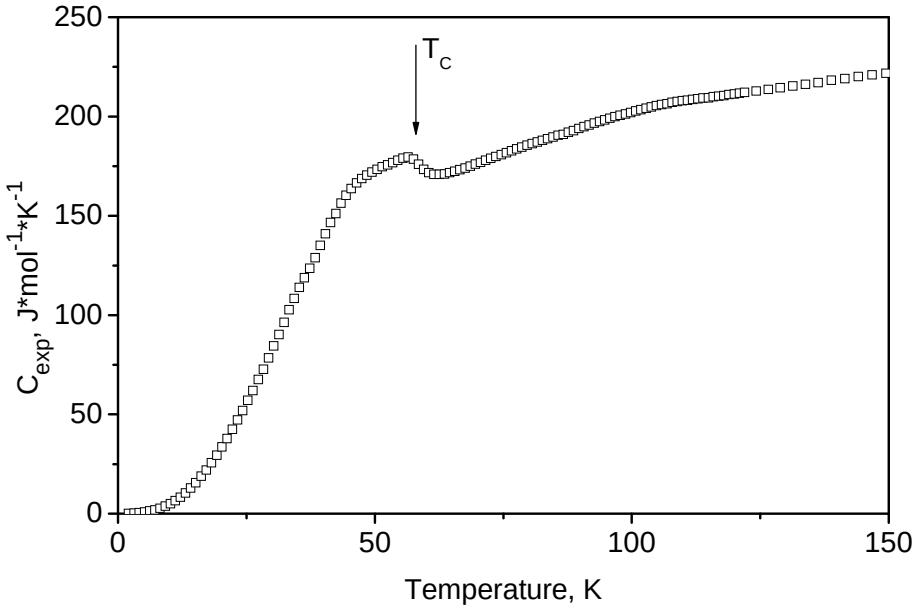

Figure 5.44 Temperature dependence of the specific heat of $Nd_5Si_{1.45}Ge_{2.55}$.

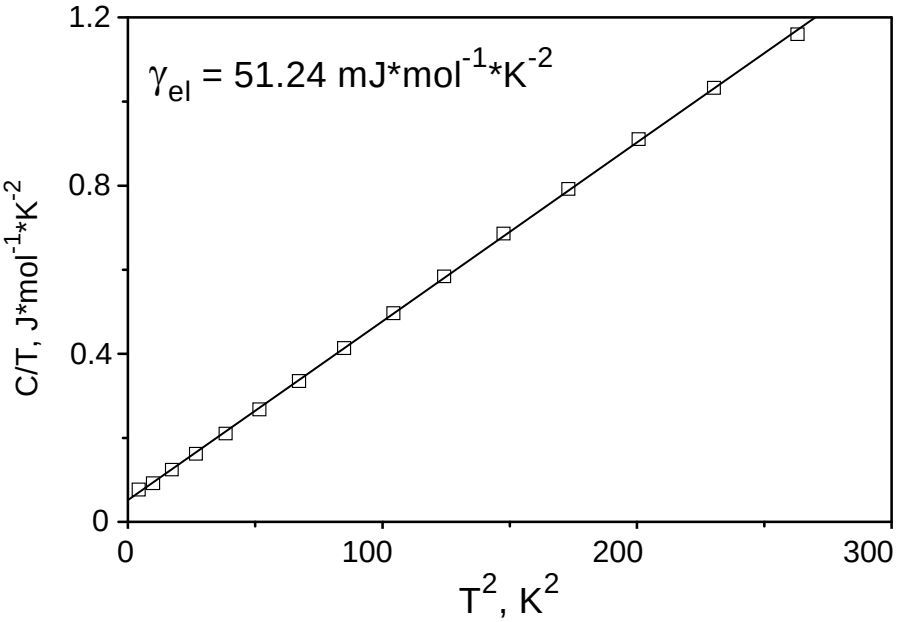

Figure 5.45 Low-temperature part of the specific heat of $Nd_5Si_{1.45}Ge_{2.55}$ as C/T vs. T^2 from which the γ_{el} value was obtained.

Strictly speaking, at low temperatures, the electron specific heat can have more complex behavior than the linear temperature dependence. However, at temperatures where the magnetic and lattice contributions to the specific heat become much more significant than the electron one, the electron contribution can be considered as $\gamma_{el}T$.

Analysis of the phonon part of the specific heat was performed with help of combined Debye-Einstein model for molar heat capacity (see Sec. 2.3.1). The total phonon spectrum is splitted up by 3 acoustic branches, described by the Debye integral and (3*$N_{f.u.}$-3) optical branches described by Einstein exponential function (Eq. (2.21), Sec. 2.3.1). Parameters of the best fit for both compounds are collected in Table 5.1.

Table 5.1. Parameters of the phonon part of the specific heat of $Nd_5Si_{1.45}Ge_{2.55}$ and $Pr_5Si_{1.5}Ge_{2.5}$ compounds.

	$Nd_5Si_{1.45}Ge_{2.55}$	$Pr_5Si_{1.5}Ge_{2.5}$
γ_{el}, mJ*mol^{-1}*K^{-2}	51.24	91.1
θ_D, K	77	68
α_D, K^{-1}	1.2*10^{-5}	1.7*10^{-4}
n_D	3	3
θ_{E1}, K	89	75
α_{E1}, K^{-1}	1.8*10^{-5}	1.8*10^{-4}
n_{E1}	2	2
θ_{E2}, K	100	80
α_{E2}, K^{-1}	1.2*10^{-5}	2*10^{-4}
n_{E2}	4	5
θ_{E3}, K	105	185
α_{E3}, K^{-1}	1.7*10^{-5}	7.5*10^{-5}
n_{E3}	5	17
θ_{E4}, K	150	-
α_{E4}, K^{-1}	1.7*10^{-5}	-
n_{E4}	6	-
θ_{E5}, K	170	-
α_{E5}, K^{-1}	1.8*10^{-5}	-
n_{E5}	7	-

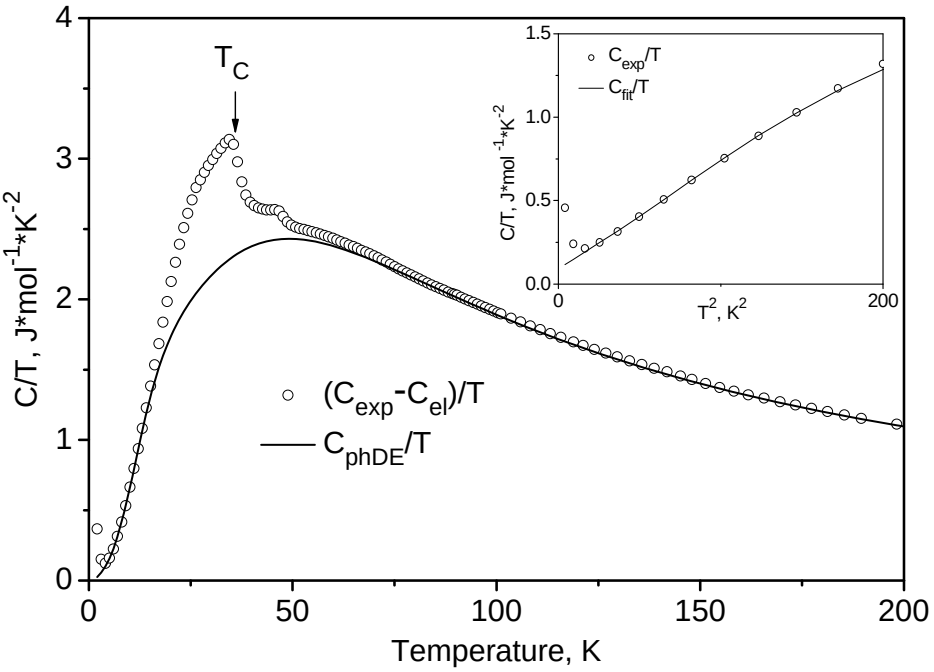

Figure 5.46 Specific heat of the $Pr_5Si_{1.5}Ge_{2.5}$ compound after subtraction of C_{el} in form C/T vs. T. The inset shows the coincidence of Debye-Einstein model with experimental data at low temperatures.

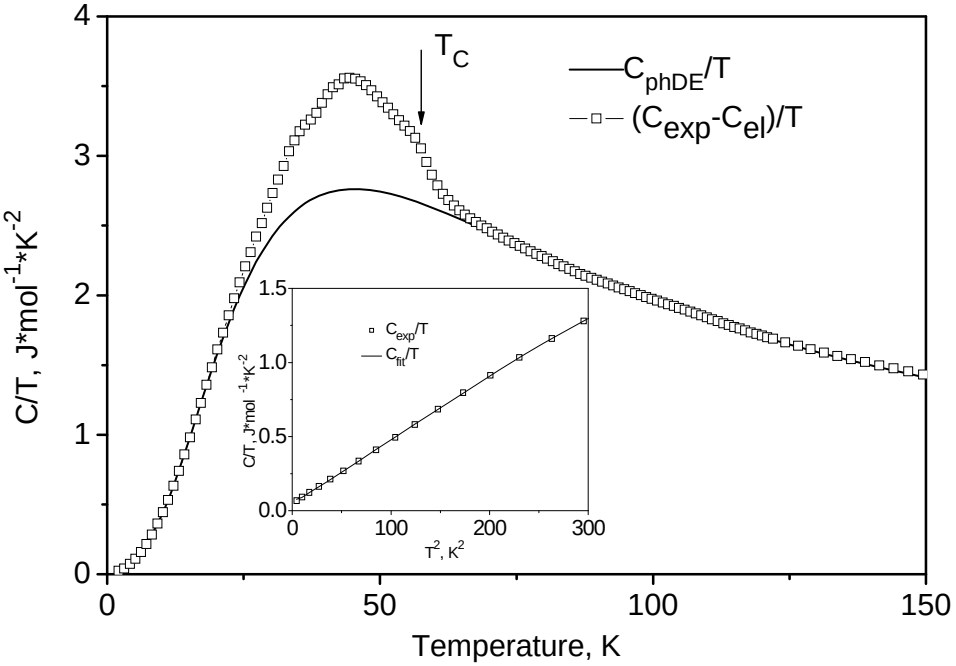

Figure 5.47 Specific heat of the $Nd_5Si_{1.45}Ge_{2.55}$ compound after subtraction of C_{el} in form C/T vs. T. The inset shows the coincidence of Debye-Einstein model with experimental data at low temperatures.

The magnetic contribution to the specific heat, obtained from the zero-field experimental data, are presented in Fig. 5.48 and Fig. 5.49 for Pr and Nd-based compounds, respectively. Their maximal values are C_{Mmax} = 24.2 J*mol^{-1}*K^{-1} at T = 34.4 K for $Pr_5Si_{1.5}Ge_{2.5}$ and C_{Mmax} = 54.5 J*mol^{-1}*K^{-1} at T = 46 K for $Nd_5Si_{1.45}Ge_{2.55}$. In Nd-based compound, the C_M reaches maximum value at temperature under T_C, that is, apparently, connected with complexity of the PM-canted FM phase transition.

The magnetic entropy was calculated using the formula:

$$S_{Mn+1} = ((C_M/T)_{n+1}+(C_M/T)_n)/2*(T_{n+1}-T_n)+S_{Mn} \quad (5.2)$$

where S_M, C_M and T are values of magnetic entropy, magnetic specific heat and temperature corresponding to n-th step of the specific heat measurement. Resulting temperature behaviors of S_M are visualized in Fig. 5.48 and Fig. 5.49.

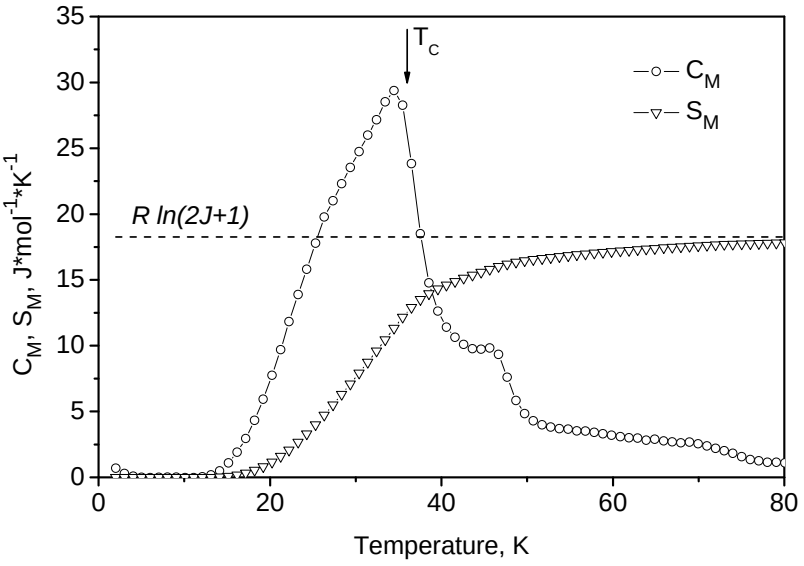

Figure 5.48 Temperature dependence of C_M and S_M of $Pr_5Si_{1.5}Ge_{2.5}$. The vertical arrow indicates the T_C value obtained from the magnetic measurements. The dashed line shows the theoretically calculated value of S_M.

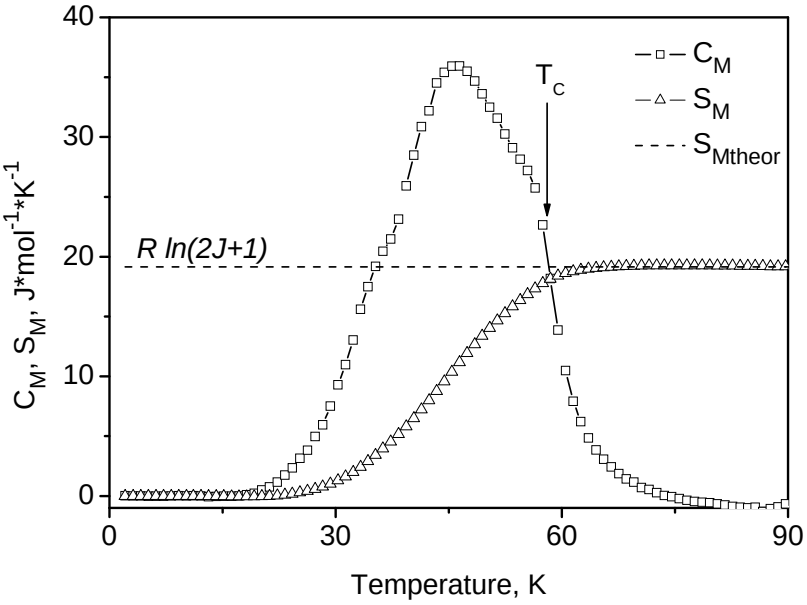

Figure 5.49 Temperature dependence of C_M and S_M of $Nd_5Si_{1.45}Ge_{2.55}$. The vertical arrow indicates the T_C value obtained from the magnetic measurements. The dashed line shows the theoretically calculated value of S_M.

In order to investigate the pressure changes in MCE, a great number of magnetization isotherms were measured near T_C at different pressures (not shown here). The measurements were performed at pressures 0, 2.5, 3.5, 5 kbar ($Pr_5Si_{1.5}Ge_{2.5}$) and 0, 3, 7.5 kbar ($Nd_5Si_{1.45}Ge_{2.55}$) with temperature step 2.5 K in magnetic filed up to 50 kOe. The MCE was calculated using the Maxwell thermodynamic relations (Sec. 2.3.3). The results are presented in Fig. 5.50, Fig. 5.51. At ambient pressure, the value of magnetic entropy change $|-\Delta S_M|_{max}$ reaches maximum value of 5.1 $J*kg^{-1}K^{-1}$ at 36.2 K on $Pr_5Si_{1.5}Ge_{2.5}$ and 4.9 $J*kg^{-1}K^{-1}$ at 56.2 K on $Nd_5Si_{1.45}Ge_{2.55}$. The last one is comparable to recently reported 5.6 $J*kg^{-1}K^{-1}$ on monoclinic $Nd_5Si_2Ge_2$ alloy (x = 0.5) (Gschneidner 2000). On increasing pressure, the $|-\Delta S_M|_{max}$ values on both compounds weakly increase. Taking into account composition-structure diagram published in Refs. (Yang 2002b, 2002c), information about T_C on monoclinic Pr- and Nd-based $R_5(Si_xGe_{1-x})_4$ from Refs. (Yang 2002a, Gschneidner 2000) and our compressibility, magnetization and MCE measurements, one can plot the dependence of the T_C and $|-\Delta S_M|_{max}$ on the unit cell volume with respect to the pressure and x (Fig. 5.52, Fig. 5.53). A comparative analysis of volume dependence of the T_C clearly shows the discrepancy between the pressure and concentration effects. On one hand, in the monoclinic range of concentration in $Nd_5(Si_xGe_{1-x})_4$ ($0.36<x<0.5$), the ratio $(dT_C/dV)_x = -1.6(6)$ K/Å^3 can be obtained. On the other hand, the dT_C/dV from our

compressibility and T_C vs. P measurements gives $(dT_C/dV)_P$ = -0.2(3) K/Å^3. For the $Pr_5(Si_xGe_{1-x})_4$, $(dT_C/dV)_x$ = -0.7(8) K/Å^3, $(dT_C/dV)_P$ = -0.12 K/Å^3.

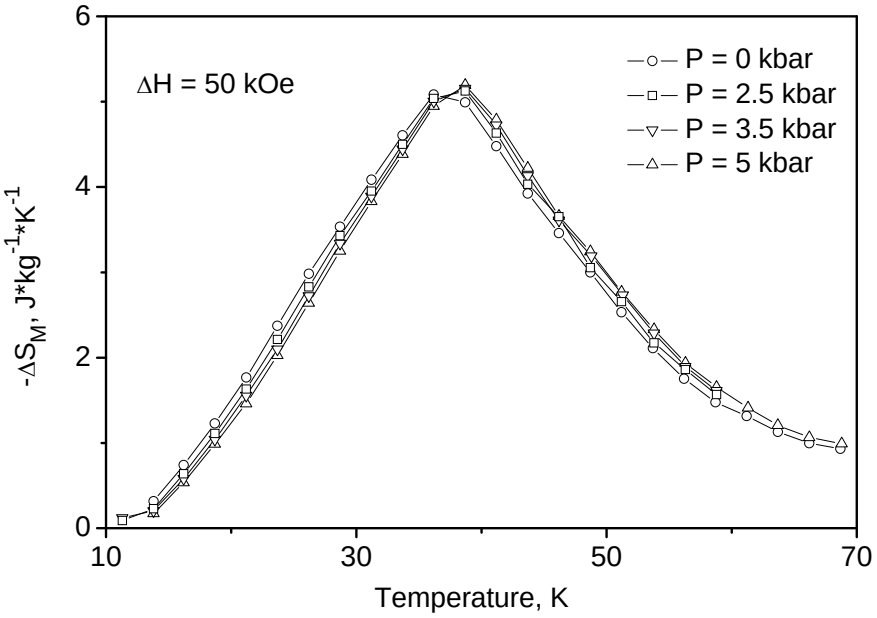

Figure 5.50 MCE in $Pr_5Si_{1.5}Ge_{2.5}$ in magnetic fields up to 50 kOe measured at different pressures.

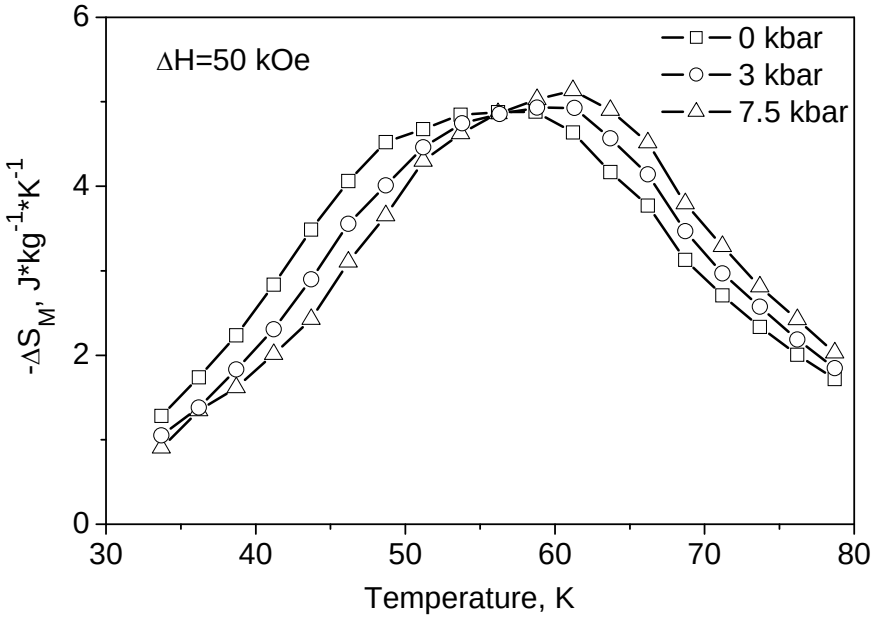

Figure 5.51 MCE in $Nd_5Si_{1.45}Ge_{2.55}$ in magnetic fields up to 50 kOe measured at different pressures.

Similar calculations for the $|-\Delta S_M|_{max}$ in $Nd_5(Si_xGe_{1-x})_4$ bring values $(d\,|-\Delta S_M|_{max}/dV)_x$ = -0.2 J*kg^{-1}K^{-1}Å^{-3} and $(d\,|-\Delta S_M|_{max}/dV)_P$ = -0.02 kg^{-1}K^{-1}Å^{-3} for the concentration and pressure dependencies, respectively.

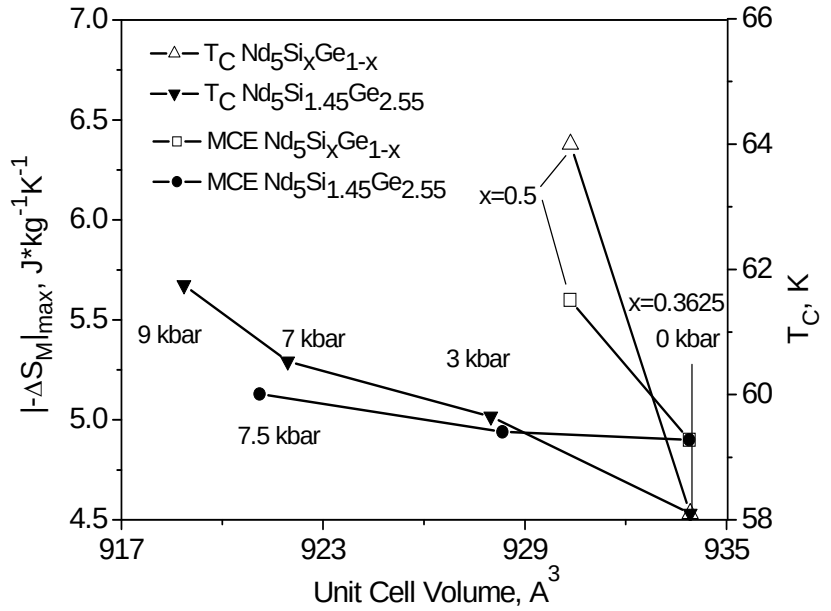

Figure 5.52 Volume dependencies of T_C and $|-\Delta S_M|_{max}$ in $Nd_5Si_{1.45}Ge_{2.55}$. The open symbols indicate data obtained from the x dependence of the unit cell volume. The solid ones correspond to pressure dependence.

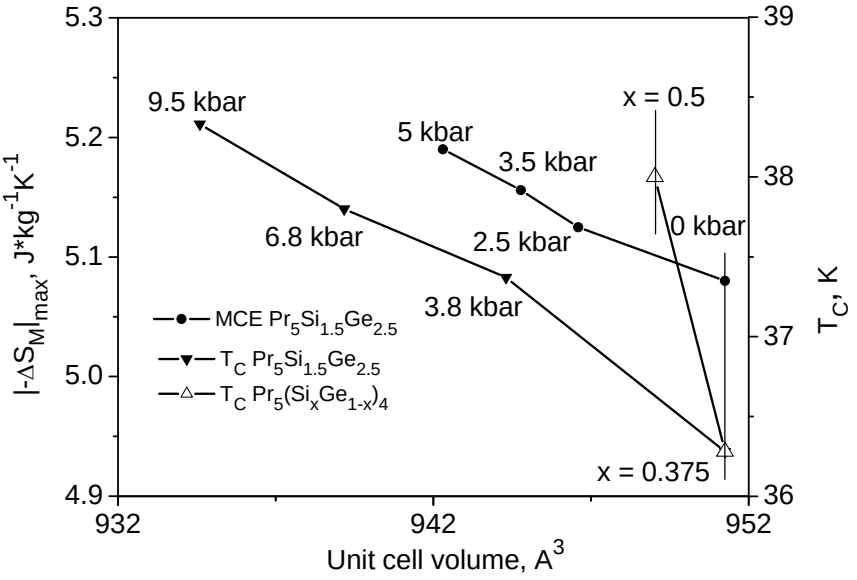

Figure 5.53 Volume dependencies of T_C and $|-\Delta S_M|_{max}$ in $Pr_5Si_{1.5}Ge_{2.5}$. The open symbols indicate data obtained from the x dependence of the unit cell volume. The solid ones correspond to pressure dependence.

6 Summary and conclusions

This Doctoral Thesis presents results of the studies of the hydrostatic pressure effects on the magnetic, magnetoelastic and magnetocaloric properties of selected members of the $R_5(Si_xGe_{1-x})_4$ family: Gd_5Ge_4, $Gd_5Si_{0.4}Ge_{3.6}$, $Tb_5Si_2Ge_2$, $Nd_5Si_{1.45}Ge_{2.55}$ and $Pr_5Si_{1.5}Ge_{2.5}$.

We verified the possibility of inducing 3D interlayer ferromagnetic correlations in Gd_5Ge_4 by high hydrostatic pressure (up to ~10 kbar). The formation of the spatially segregated regions with *O*(I)-FM ground state within the main *O*(II)-AFM phase in Gd_5Ge_4 was studied by extensive LTE and magnetization measurements under high hydrostatic pressure. The percentage of the pressure induced *O*(I)-FM phase with respect to the applied pressure on the basis of LTE and magnetization has been estimated. At pressures of over 10 kbar, the low-temperature *O*(I)-FM ground state is stabilized in the entire sample volume.

The studies of MCE of Gd_5Ge_4 by means of magnetization measurements and Maxwell's thermodynamic relations showed that the consequence of suppression of field induced first-order AFM-FM transition by high pressure and formation of the pressure-induced *O*(I)-FM state is a slow increase of the MCE, with increasing percentage of the *O*(I)-FM phase.in fields $H < H_C$.

Values of both T_N and T_C (induced by pressure) increase with pressure. Significantly different slopes - remarkable increase of Curie temperature with pressure (dT_C/dP = +5.3 K/kbar) and only moderate pressure changes of Neel temperature (dT_N/dP = +0.6 K/kbar) are in qualitative agreement with concentration dependencies of these two transitions within the series $Gd_5(Si_xGe_{1-x})_4$.

Si substituted Gd_5Ge_4 - $Gd_5Si_{0.4}Ge_{3.6}$ with ferromagnetic ground state (T_C = 85.9(5) K, T_N = 129.1 K) exhibit negligible pressure effect on saturation magnetization. On increasing pressure, both T_N and T_C shift linearly to higher values at rates dT_N/dP = +0.6 K/kbar, dT_C/dP = +2.25 K/kbar. Pronounced hysteresis of magnetic isotherms at ambient pressure as a consequence of field-induced AFM-FM transition almost disappears at 8.4 kbar in agreement with formation of FM state under pressure.

Comparison of the pressure effects on these two compounds with ambient pressure temperature-concentration diagram allows us to derive the volume dependencies of the transition temperatures on the basis of pressure and Si-doping effect

(effect of "chemical pressure"). Generally, application of hydrostatic pressure and Si-doping leads to reducing of volume and consequent increasing of T_C in agreement with localized nature of magnetism of $R_5(Si_xGe_{1-x})_4$. However, the dT_C/dV rates obtained upon applied pressure have significantly lower values than values extracted from the temperature-composition diagram. Thus, the observed changes cannot be explained by pure volume effects of the chemical pressure induced by Si-Ge substitution. Thus, the electronic structure changes play a paramount role in the magnetic properties of Ge-rich $Gd_5(Si_xGe_{1-x})_4$.

The studies of the temperature-pressure phase diagram of $Tb_5Si_2Ge_2$ by means of thermal expansion and magnetization measurements showed that application of hydrostatic pressure leads to recoupling of high-temperature second-order magnetic and the low-temperature first-order crystallographic transformations. A tricritical point was found in the vicinity of 9 kbar. Merging two phase boundaries significantly influences the shape and maximum value of the magnetocaloric effect. The value of the purely crystallographic contribution to the MCE has been estimated to be nearly 40% of the total MCE in magnetic field up to 50 kOe. The magnetic contribution to the total entropy of the system at the magnetic phase transition was extracted from the specific heat data by means of Debye model for the lattice heat capacity.

Qualitatively similar behavior of magnetic, elastic and magnetocaloric properties was observed for $Nd_5Si_{1.45}Ge_{2.55}$ and $Pr_5Si_{1.5}Ge_{2.5}$ compounds with monoclinic crystallographic structure. The observed pressure induced increase of T_C was expected from localized nature of the rare-earth magnetism. Relatively small values of dT_C/dP and $d|-\Delta S_M|/dP$ in both compounds are consequence of second-order magnetic phase transition with no changes of crystal structure. The magnetic part of the total entropy was obtained from ambient pressure measurements of the specific heat using the combined Debye-Einstein model for the lattice heat capacity. Values of dT_C/dV and $d\left|-\Delta S_M\right|/dV$ obtained from experiments under high hydrostatic pressure are sufficiently lower than those estimated from the x dependence of the lattice cell volume. These results indicate that and that decisive role in the changes of magnetic, magnetoelastic and magnetocaloric properties play electronic structure changes induced by Si-Ge substitution for whole series of $R_5(Si_xGe_{1-x})_4$ compounds.

7 References

Arnold Z., J.Kamarád, P.A.Algarabel, B.Garcia-Landa, M.R.Ibarra, IEEE Trans. Magn. **30**, 619 (1994)

Bachmann R., Rev. Sci. Instrum. **43**, 205 (1972)

Choe W., V.K.Pecharsky, A.O.Pecharsky, K.A.Gschneidner, Jr., V.G.Young, Jr., G.J.Miller, Phys. Rev. Lett. **84**, 4617 (2000)

Debye P., Ann. Phys. (Leipzig) **81,** 1154 (1926)

Devonshire A.F., Phil. Mag. **40,** 1040 (1949)

Devonshire A.F., Phil. Mag. **42,** 1065 (1951)

Devonshire A.F. Adv.Phys. **3,** 85 (1954)

Garfinkel M., D.E.Marother, Pressure effect on superconducting lead, Physical Review, v. 122, n. 2, 459-468 (1961)

Garlea V.O., V.K.Pecharsky, K.A.Gschneidner, Jr., Phys Rev. B **72**, 104431 (2005)

Giauque W.F., J. Am. Chem. Soc. **49,** 1864 (1927)

Gopal E.S.R., Specific Heats at Low Temperatures, New York: Plenum Press (1966)

Gschneidner K.A., Jr., V.K.Pecharsky, A.O.Pecharsky, V.V.Ivtchenko, E.M.Levin, J.Alloys and Compounds **303-304,** 214-222 (2000)

Holtzberg F., R.J.Gambino, T.R.McGuire, J.Phys. Chem. Solids **28**, 2283 (1967)

Kamarád J., K.V.Kamenev, Z.Arnold, in High Pressure Science and Technology, Proceeding of the Joint XV AIRPAT and XXXIII EHPRG International Conference, Warsaw, Poland 51 (1995).

Kamarád J., unpublished (1997)

Kamarád J., Encyclopedia of Materials: Science and Technology (Elsevier Science Ltd.) 4976 (2001)

Kasuya T., Prog. Theor. Phys. **16**, 45 (1956)

Kittel C., Introduction to Solid State Physics, New York: Wiley (1986)

Kouvel J.S., R.H.Wilson, J. Appl. Phys. **32**, 435 (1961)

Levin E.M., V.K.Pecharsky, K.A.Gschneidner, Jr., Phys. Rev. B **60**, 7993 (1999)

Levin E.M., V.K.Pecharsky, K.A.Gschneidner, Jr., P.Tomlinson, J. Magn. Magn. Mater. **210**, 181 (2000a)

Levin E.M., V.K.Pecharsky, K.A.Gschneidner, Jr., Phys. Rev. B **62**, R14625 (2000b)

Levin E.M., V.K.Pecharsky, K.A.Gschneidner, Jr., Phys. Rev. B **63**, 174110 (2001a)

Levin E.M. V.K.Pecharsky, K.A.Gschneidner, Jr., G.J.Miller, Phys. Rev. B **64**, 235103 (2001b)

Levin E.M., K.A.Gschneidner, Jr., V.K.Pecharsky, Phys. Rev. B **65**, 214427 (2002)

Liu G.J., Sun J.R., Shen J., Gao B., Zhang H.W., Hu F.X. Shen B.G., Appl. Phys. Lett. **90**, 032507 (2007)

Magen C., L.Morellon, P.A.Algarabel, C.Marquina, M.R.Ibarra, J.Phys.: Condens. Matter **15,** 2389-2397 (2003a)

Magen C., Z.Arnold, L.Morellon, Y.Skorokhod, P.A.Algarabel, M.R.Ibarra, J.Kamarad, Phys. Rev. Lett. **91**, 207202 (2003b)

Magen C., C.Ritter, L.Morellon, P.A.Algarabel, M.R.Ibarra, J.Phys.:Condens. Matter **16,** 7427–7437 (2004)

Martin C.A., J. Phys.: Condens. Matter **3**, 5967 (1991)

McMichael R.D., J.J.Ritter, R.D.Shull., J. Appl. Phys **73,** 6946 (1993a)

McMichael R.D., R.D.Shull, L.H.Bennett, C.D.Fuerst, J.F.Herbst, Nanostruct. Matter, **2,** 277 (1993b)

Morellon L., P.A.Algarabel, M.R.Ibarra, J.Blasco, B.Garcia-Landa, Z.Arnold, F.Albertini, Phys.Rev. B **58**, R14721 (1998a)

Morellon L., J.Stankiewicz, B.Garcia-Landa, P.A.Algarabel, M.R.Ibarra, Appl. Phys. Lett. **73**, 3462 (1998b)

Morellon L., J.Blasco, P.A.Algarabel, M.R.Ibarra, Phys. Rev. B **62**, 1022 (2000)

Morellon L., P.A.Algarabel, C.Magen, M.R.Ibarra, J. Magn. Magn. Mater. **237**, 181 (2001a)

Morellon L. C.Magen, P.A.Algarabel, M.R.Ibarra, C.Ritter, Appl. Phys. Lett., **79**, No.9 1318 (2001b)

Morellon L., C.Ritter, C.Magen, P.A.Algarabel, M.R.Ibarra, Phys. Rev. B **68**, 024417 (2003)

Morellon L., Z.Arnold, P.A.Algarabel, C.Magen, M.R.Ibarra, Y.Skorokhod, J.Phys.: Condens. Matter **16,** 1623-1630 (2004)

Nazih M., A. de Visser, L.Zhang, O.Tegus, E.Bruck, Solid State Comm.**126**, 255 (2003)

O'Handley R.C., Modern Magnetic Materials: principles and applications (John Wiley & Sons, Inc., New York) (2000)

Pecharsky V.K., K.A.Gschneidner, Jr.,Phys.Rev.Lett. **78,** 4494 (1997a)

Pecharsky V.K., K.A.Gschneidner, Jr., Appl. Phys. Lett. **70,** 3299 (1997b)

Pecharsky V.K., K.A.Gschneidner, Jr., J.Alloys Comp. **260,** 98 (1997c)

Pecharsky V.K., K.A.Gschneidner, Jr., J. Magn. Magn. Mater. **167,** L179 (1997d)

Pecharsky V.K., K.A.Gschneidner, Jr., Adv. Cryog. Eng. **43,** 1729 (1998)

Pecharsky V.K., K.A.Gschneidner, Jr., J. Appl. Phys. **86,** 565 (1999)

Pecharsky V.K., K.A.Gschneidner, Jr. Adv. Mater **13**, 683 (2001)

Pecharsky A.O., K.A.Gschneidner Jr. ,V.K.Pecharsky , C.E.Schindler, J.Alloys Compounds **338,** 126–135 (2002)

Pecharsky V.K., A.P.Holm, K.A.Gschneidner, Jr., R.Rink, Phys. Rev. Lett. **91**, 197204 (2003)

Rao G.H., J. Phys.: Condens. Matter **12**, L93 (2000)

Reich S., T.Godin, Meas. Sci. Technol. **7,** 1079-1082 (1996)

Ritter C., L.Morellon, P.A.Algarabel, C.Magen, M.R.Ibarra, Phys Rev. B, **65,** 094405 (2002)

Ruderman M.A., C.Kittel, Phys. Rev. **96**, 99 (1954)

Schilling J.S., in High Pressure in Science and Technology, Vol. **22**, eds C. Homan, R. K. MacCrone, E. Whalley (Elsevier Science Publisher, Amsterdam), Part I, 79 (1984)

Schilling J.S., Physica **139** & **140** B, 369 (1986)

Serdyuk Yu.V., R.P.Krentsis, P.V.Gel'd, Sov. Phys. Solid State **23**, 1592 (1982)

Smith G.S., A.G.Tharp, Q.Johnson, Nature **210**, 1148 (1966)

Smith T.F., C.W.Chu, M. B. Maple: Cryogenics **9**, 53 (1969)

Sousa J.B., M.E.Braga, F.C.Correia, F.Carpinteiro, L.Morellon, P.A.Algarabel, M.R.Ibarra, J.Appl. Phys. **91**, 4457 (2002)

Spichkin Y.I., V.K.Pecharsky, K.A.Gschneidner, Jr., J.Appl. Phys. **89**, 1738 (2001)

Stankiewicz J., L.Morellon, P.A.Algarabel, M.R.Ibarra, Phys. Rev. B **61**, 12651 (2000)

Svoboda P., P.Javorský, M.Diviš, V.Sechovský, F.Honda, G.Oomi, A.A.Menovsky, Phys. Rev. B **63**, 212408 (2001)

Tegus O., E.Brück, K.H.J.Buschow, F.R. de Boer, Nature (London) **415**, 150 (2002)

Teng B., M.Tu, Y.Chen, J.Tang, J.Phys.: Condens. Matter **14**, 6501 (2002)

Warburg E., Ann. Phys. Chem. **13**, 141 (1881)

Yang H.F., G.H.Rao, G.Y.Liu, Z.W.Ouyang, X.M.Feng, W.F.Liu, W.G.Chu, J.K.Liang, J. Phys.: Condens. Matter **14,** 9705- 9711 (2002a)

Yang H.F., G.H.Rao, G.Y.Liu, Z.W.Ouyang, W.F.Liu, X.M.Feng, W.G.Chu, J.K.Liang. J. Alloys Comp. **346,** 190-196 (2002b)

Yang H.F., G.H.Rao, W.G.Chu, G.Y.Liu., Z.W.Ouyang, J.K.Liang, J. Alloys and Compounds **339,** 189–194 (2002c)

Yang H.F., G.H.Rao, G.Y.Liu, Z.W.Ouyang, W.F.Liu, X.M.Feng, W.G.Chu J.K.Liang, Physica B **325,** 293 (2003)

Yao Y.D., Lee S.F., Lee M.D., Wu K.T., Cheng D.G., Thuy N.P., Hien N.T., Tai L.T., Vinh T.Q., Nong N.V., Physica B **237,** 324-327 (2003)

Yosida K., Phys. Rev. **106**, 893 (1957)

8 Acknowledgements

In the last lines of the thesis I would like to express my gratitude to all people who helped make this thesis possible.

First of all, I must express my profound gratitude to my supervisor Dr. Zdeněk Arnold for his inestimable support and guidance through my doctoral research. I learnt a lot in the field of magnetism and experimental equipment working under his supervision. His valuable discussions and critical commentary on my work have played a major role in preparation of the scientific publications and the thesis.

I am deeply thankful to Dr. Jiří Kamarád for invaluable teaching, advice, suggestions, helpful discussions about high pressure experimental equipment and overall support during my stay in Prague.

I would like to thank Doc. P.Svoboda for helpful advices related to the specific heat studies and Prof. A.V.Andreev for help and constructive criticism.

Essential work was performed at The Joint Laboratory for Magnetic Studies of the Charles University. I would like to express gratitude to Dr. Eva Šantavá, Ing. J.Šebek, Dr. D.Vasylyev and Dr. O.Syschenko for help with my experiments.

My special thanks belong to our Spanish colleagues L.Morellon, P.A.Algarabel and C.Magen for providing samples and productive cooperation during work on the thesis.

I wish to thank our technicians V. Jiřímský and T. Novotný for preparation of high pressure equipment used in experiments.

Finally, I would like to thank my family for their love and support.

9 List of publications:

Y.Skorokhod, Z.Arnold, J.Kamarad, L.Morellon, C.Magen, Magnetocaloric properties of $Nd_5Si_{1.45}Ge_{2.55}$ compound under high hydrostatic pressure, High Pressure Research, **26** (4): 495-498 (2006)

L.Morellon, Z.Arnold, C.Magen, C.Ritter, O.Prokhnenko, Y.Skorokhod, P.A.Algarabel, M.R.Ibarra and J.Kamarad, Pressure Enhancement of the Giant Magnetocaloric Effect in $Tb_5Si_2Ge_2$, Phys. Rev. Lett. **93**, 137201 (2004)

L.Morellon, Z.Arnold, P.A.Algarabel, C.Magen, M.R.Ibarra and Y.Skorokhod, Pressure effects in the giant magnetocaloric compounds $Gd_5(Si_xGe_{1-x})_4$, J. Phys.: Condens. Matter **16** 1623-1630 (2004)

C.Magen, Z.Arnold, L.Morellon, Y.Skorokhod, P.A.Algarabel, M.R.Ibarra and J.Kamarad, Pressure-Induced Three-Dimensional Ferromagnetic Correlations in the Giant Magnetocaloric Compound Gd_5Ge_4, Phys. Rev. Lett. **91**, 207202 (2003)